Beyond Traditional Superatom Ligands and Cores

Evan Ambrose Doud

Submitted in partial fulfillment of the
requirements for the degree of
Doctor of Philosophy
in the Graduate School of Arts and Sciences

COLUMBIA UNIVERSITY

2020

Abstract

Beyond Traditional Superatom Ligands and Cores

Evan Ambrose Doud

This dissertation summarizes my research in the Roy group on the development, synthesis, and study of new N-heterocyclic carbene (NHC) based ligands and nickel phsophinidene core compositions of molecular clusters, also known as superatoms.

Chapter 1 introduces superatoms as atomically precise and discreet building blocks for use in the design and synthesis of novel materials. A brief history as well as selected synthetic strategies of superatoms will be introduced. The relevant materials properties of superatoms as well as their dependence on core composition and ligand structure will be discussed. Next, the use of superatoms with specialized or functionalizable ligands to synthesize new materials will be demonstrated. This chapter details the importance of the superatom ligands and core composition is the foundation that the subsequent chapters builds upon in developing these two areas.

Chapter 2 introduces a functionalized NHC as a potential superatom ligand. While not necessary for all superatom ligands, ligands that enable electronic access to the superatom core are attractive. In this chapter, the conductance of potential NHC based ligands are probed through the scanning tunneling microscope-based break-junction (STM-BJ) method. A novel method of forming single molecule junctions *in situ* was used and these ligands are found to display a length dependent conductance with strong coupling to the Au electrode, confirming their potential use as ligands for superatoms.

Chapter 3 describes the nature of the NHC–M bond in self-assembled monolayers (SAMs) on a Au(111) surface using high-resolution spectroscopy and theoretical calculations. This study

was performed as a result of challenges and questions encountered during the work of Chapter 2. The results obtained from this study explore an important structure-function relationship of NHC ligands and have broader impact in materials chemistry beyond superatoms.

Chapter 4 explores the synthesis of superatoms with NHC ligands beyond simple imidazolium-based NHCs. This chapter describes the two primary synthetic techniques used and the synthesis of NHC-ligated superatoms. This work is also ongoing and characterization is limited to crude single crystal X-ray diffraction structures and select NMRs.

Finally, Chapter 5 details the use of uncommon organocyclophosphine reagents to synthesis novel nickel-phosphinidene molecular clusters, a potential new superatom. In this chapter the synthesis of a family of nickel-phosphinidene molecular clusters is described and studied. A potential application of these molecular clusters is explored through the thermolytic conversion to the industrially relevant Ni_2P.

Table of Contents

List of Figures and Tables

Acknowledgments

I would like to begin by acknowledging the enormous opportunity granted to me by my advisor, Prof. Xavier Roy. Without his mentorship I would not have been able to write this dissertation. I have encountered numerous challenges over the past several years, in and outside of research, and Xavier allowed me the freedom meet those challenges, for which I am grateful.

To my committee members; Prof. Latha Venkataraman, Dr. Michael Steigerwald, Prof. Colin Nuckolls, and Prof. Jonathan Owen, I thank you all for your insight and guidance. The unique flair and perspective each of you possess is both admirable and inspirational.

My scientific journey did not begin at Columbia and I must thank the numerous teachers, professors, and mentors that have had a hand in shaping my path thus far.

I am fortunate to have been blessed with incredibly supportive parents, Ralph and Virginia Doud. I am forever grateful for their love, sacrifice, and hard work, without which I also would not be able to write this dissertation. To my brother, Brigham Doud, I thank you for showing me the value of hard work and to always be passionate in all things you do. I am also blessed with an extended family who is a source of constant support and for them I am grateful.

Chris, thank you for your support through the past few years, especially during this time of ultimate activation and perpetual meltdown.

To all my friends, past and present, from Radford to Pittsburgh to New York, I do not know if I would still be here today without you. In particular the members of my cohort in Columbia Chemistry, especially those in the Roy, Cornish, and Nuckolls Labs.

Finally, I thank all who have entered my life, I am who I am because of you.

ἀρετή

Chapter 1: Superatoms in Materials Science

1.1 Preface

Significant portions of this chapter are adapted from a review that is in press as of the writing of this dissertation entitled "Superatoms in Materials Science" by Evan A. Doud, Anastasia Voevodin, Taylor J. Hochuli, Anouck M. Champsaur, Colin Nuckolls, and Xavier Roy to be published in *Nature Reviews Materials*.

1.2 Introduction

Crystalline solids are the foundation of countless technologies, from solar cells to lithium ion batteries to quantum computers. Harnessing the unique functions of such materials requires an ability to precisely control or tune their properties. As an example, most modern electronic devices are based upon our ability to tune the electrical behavior of silicon by introducing small amounts of impurities in the crystalline lattice without changing its overall structure. The Periodic Table of the elements contains 82 stable, non-radioactive, fundamental atomic building blocks that can be used to assemble crystalline materials. Each atom has a set of intrinsic characteristics that governs whether it can bond with other atoms and what structures they will form. This is the foundation of solid state chemistry. While the fundamental characteristics are intrinsic to each element, the atom itself cannot be altered. This presents an immense challenge for the design of materials with tunable properties because substituting one type of atom for another often leads to wholly new structures with entirely different properties.

The ability to tailor the properties of crystalline solids, by controlling their structures and compositions at the *atomic level* presents unique opportunities for the development of new functional materials by design and the discovery of novel phenomena. Crystalline solids are typically synthesized from elemental and polyatomic precursors through high temperature reactions that intrinsically produce thermodynamically stable compounds. This process inhibits the creation of metastable structures and leaves little room for rational tuning of the materials and their properties. Within this context, assembling hierarchical materials from preformed nanoscale building blocks with well-controlled and tunable properties offers significant benefits over traditional solid state reactions. One of the key challenges in this approach is to design building blocks that combine both atomic precision and synthetic flexibility. Nanocrystals, for instance, have remarkably tunable compositions and thus have useful electronic and optoelectronic properties, but they are polydisperse and have ill-defined surface chemistry, creating challenges in understanding and controlling the structure-properties relationships of the resulting solids[1-3].

Clusters are collections of atoms intermediate in size between a molecule and a bulk solid. Certain clusters adopt structural motifs that confer unique stability and enable the constituent atoms to behave as single units exhibiting collective behaviors. By combining atomic precision, synthetic flexibility and tunable properties, such clusters have emerged as exciting building blocks (or "superatoms") for materials design. These include noble metal "magic number" clusters, metal chalcogenide molecular clusters, fullerenes, Zintl ions, and boron/silicon/aluminum clusters. Many of these building blocks are stabilized with capping ligands. These ligands are important in that they direct self-assembly and control the coupling between clusters. Theoretical studies of select atomic clusters (e.g., Al_{13}^-) have shown that their electronic structures resemble that of

traditional atoms, with delocalized cluster-based *s*-, *p*-, and *d*-like orbitals[4]. These clusters were originally named "superatoms"[5] but the term has since then been applied more widely to clusters whose behaviors mimic those of traditional atoms. For this review we use this more inclusive definition of superatoms.

Figure 1.1 illustrates the general vision of the approach developed in this review: atomically precise materials, termed superatomic crystals, with tailored and tunable functions are created by assembling judiciously designed and synthesized superatoms.

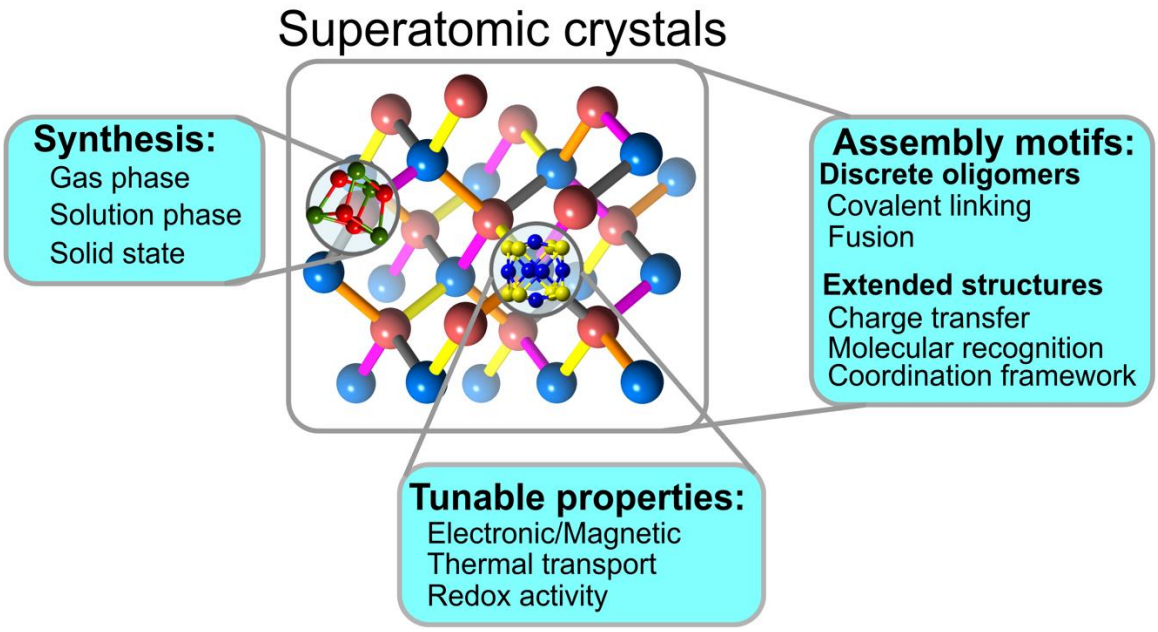

Figure 1.1: The design of superatomic crystals. The large blue and red spheres are the superatoms and the different bond colors represent different inter-superatom interactions or bonding. Superatomic crystals are prepared by combining structurally and electronically complementary superatoms in solution. A variety of tunable molecular clusters can be used as superatomic building blocks and different assembly motifs can assemble them into materials. Upon assembly, the internal structures of the constituent superatoms remain unchanged, resulting in materials that can be characterized by single-crystal x-ray diffraction (SCXRD).

Recent excellent reviews by Khanna[6] and Jena[7] explore the theoretical work on superatoms. This Review will provide a broadened introduction on synthetic strategies to create superatoms and emphasize the assembly strategies of mono-component and multicomponent superatomic crystals with emergent collective behaviours.

1.3 Overview of Clusters as Superatoms

The creation of superatomic crystals begins with the design and synthesis of building blocks capable of assembling together while maintaining their individual structures. The synthesis of metallic clusters and transition metal chalcogenide molecular clusters has been extensively reviewed[8-10]. In this section, we outline the general synthetic strategies to form clusters that can be used as superatoms and we discuss their isolated properties.

Synthesis of Superatoms

The synthesis of superatoms can be classified in three general approaches: gas phase synthesis, solution phase synthesis, and excision from solid state compounds. Figure 1.2a-c illustrates these three general approaches.

Gas Phase Synthesis

Superatoms were originally discovered in gas phase experiments. References to the formation of atomic aggregates date back to the 1930s[11] but the systematic study of clusters in mass spectrometer began in earnest in the 1970s and 1980s[12-14]. The concept of superatoms was not used to describe these gas phase clusters until the idea was proposed by Khanna and Jena[4] and was first experimentally demonstrated by Castleman and co-workers for Al clusters produced in the gas phase[5]. Beyond Al clusters, many other types of magic size clusters can be produced by

laser induced vaporization of metal substrates or other vaporization methods, and detected by mass spectrometry[14-15]. This general approach presents two major limitations: the clusters are typically unstable and highly reactive when removed from the vacuum environment, and the amount of cluster produced is generally too small to be used as building blocks for creating materials. We note that despite these challenges, there have been theoretical studies of their reaction chemistry[16] as well as important advances in the use of gas-phase synthetic methods to create catalytically active nanocluster-based materials[17].

Long and co-workers developed a modified gas phase method to prepare transition metal chalcogenide clusters that could be handled outside the vacuum chamber by evaporating bulk binary compounds within a partial vacuum containing vapors of a capping ligands[18]. One key limitation of this method is that it produces many different clusters, which need to be separated and characterized individually, resulting in very low yields for any particular superatom.

Solution Phase Synthesis

Solution phase synthesis is the most widely used and efficient approach to prepare noble metal and metal chalcogenide molecular clusters with varied structures[8-9, 19]. The synthesis of noble metal magic size clusters has been reviewed extensively[20-22]. For metal chalcogenide clusters, Dance and Fisher[9] classify the most common synthetic strategies in two categories: i) association of ions, and ii) reaction of a metal atom precursor with a chalcogen atom precursor.

In the first approach, a M^{n+} ion is reacted with an E^{2-} source under conditions that result in the formation of a cluster[9]. The synthesis of the magnetic cluster $[Fe_6S_8(PEt_3)_6][BPh_4]_2$[23] illustrates this approach: H_2S is bubbled through a solution that contains $Fe(BF_4)_2$ and an excess of PEt_3. Upon addition of $NaBPh_4$, black crystals of $[Fe_6S_8(PEt_3)_6][BPh_4]_2$ form. A modified strategy,

primarily developed by Fenske, reacts trialkylsilyl chalcogenide reagents with metal halide to eliminate trialkylsilyl halides and form metal-chalcogen bonds. The use of trialkylsilyl chalcogenide reagents is a preferred approach due to their ease of handling over gaseous reagents as well as the facile removal of the trialkylsilyl halides.

The second approach to synthesize metal chalcogenide superatoms combines a reactive source of metal with a reactive source of chalcogen (typically a phosphine chalcogenide)[9]. The quintessential example of this approach was pioneered by Steigerwald and co-workers[24] in the synthesis of $Ni_9Te_6(PEt_3)_8$, which is obtained by combining $Ni(COD)_2$, $TePEt_3$, and PEt_3 in a 1:1:1 molar ratio in toluene.

Excision from Solid State Compounds

Several bulk solids have identifiable clusters as their fundamental structural units[25], which can be excised from the lattice to give superatoms. These materials are typically second and third row early transition metal chalcogenides or halide such as $Re_6E_8X_2$[26-28], Mo_6E_8[29-30], and $Li_2Nb_6X_{16}$ (E = S, Se, Te, and X = Cl, Br, I)[31-32]. Excision involves heating the solid with excess capping ligand (e.g., cyanide, hydroxide, halide) that then coordinates the excised clusters to stabilize the core. These capping ligands can then be substituted with a variety of organic molecules.

Isolated Properties of Superatoms

The properties of atomic solids are determined by their constituent atoms and similarly, superatomic crystals have collective properties that result from the constituent superatoms and their interactions. The choice of superatoms is critical in the design of these materials. Unlike isolated atoms which have fixed properties, the properties of superatoms can be tuned in a number of ways (e.g., constituent atoms, ligands). In the following section, we will describe several

properties relevant to materials design (electrochemical, magnetic, optical) and how those properties can be precisely controlled in superatoms.

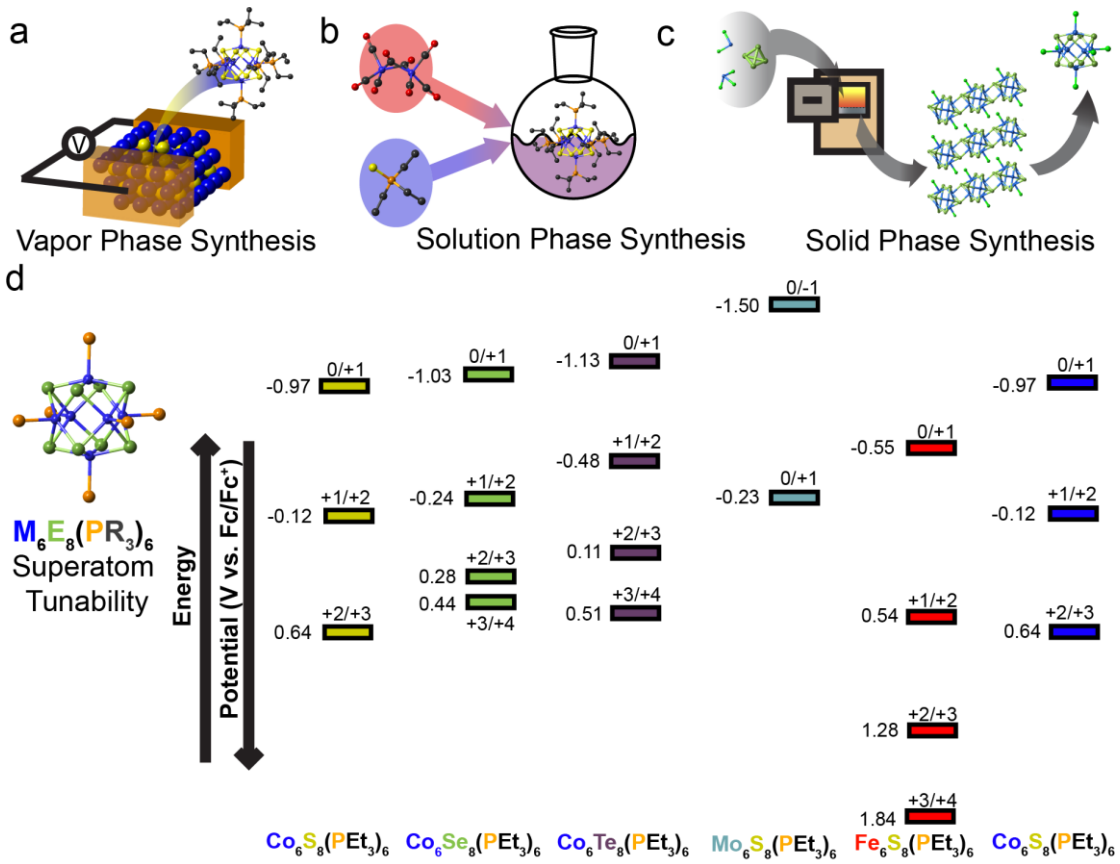

Figure 1.2: Synthesis and tunability of superatoms. **a-c.** Schematics illustrating the three general approaches to prepare superatoms. **d.** Electrochemical potential for a series of superatoms with the same $M_6E_8(PEt_3)_6$ structure but different core composition, as determined from cyclic voltammetry. Data adapted from [33-36].

Electrochemical Properties

Bonding within the cluster core produces highly delocalized electronic structures that enable rich electrochemical behaviour to exist[37]. The electrochemical properties of the superatoms are primarily dictated by the composition and structure of the core, as illustrated in Figure 1.2d.

Metal chalcogenide superatoms are typically electron rich with oxidation potentials that can rival alkali metals[38]. Other superatoms such as $Fe_8O_4(pz)_{12}Cl_4$ (pz = pyrazolate anion, $C_3H_3N_2^-$) and Al_{13} are excellent electron acceptors.

The electrochemical properties of superatoms can also be fine-tuned by modifying the ligand shell. For instance, by replacing strong σ-donor capping ligands such as phosphines with weaker σ-donor or π-acceptor ligands, one can effectively and precisely shift the oxidation potential of superatoms. Khanna recently published calculations showing the addition of 8 PEt_3 ligand to the Ni_9Te_6 core reduces the ionization potential by 2.5 eV to 3.3 eV, making $Ni_9Te_6(PEt_3)_8$ a superalkali and a strong donor[39]. By attaching CO ligands to the Ni_9Te_6 core, the cluster becomes an electron acceptor with an electron affinity of 3.23 eV[40]. The tunable effects of the ligand shell on the electrochemical properties of the hexanuclear cobalt sulfide superatoms was also theoretically and experimentally demonstrated for a series of $Co_6S_8(PEt_3)_{6-x}(CO)_x$ (x = 1 – 3) superatoms using photoelectron spectroscopy to probe their electron affinity and electronic structures[41]. The key result is that increasing the degree of carbonylation produced superatoms with higher electron affinities.

The examples above highlight the electrochemical flexibility of superatoms. An additional dimension of tunability emerges by adding multiple types of metal atoms to the cores. For example, the Long group modified the redox behaviour of the Re_6Se_8 core by replacing one of the metal atoms with Os[42].

Magnetic Properties

The traditional metallic superatoms first described by Khanna and Jena[4] have closed shell electronic structures and are thus of limited used for their magnetic properties. Many theoretical

studies suggest that magnetic metallic clusters could be produced by incorporating transition metal or rare earth metal atoms into the core of a diamagnetic cluster or by assembling the cluster entirely from magnetic elements[43-47]. This attractive concept lacks experimental demonstration because such magnetic superatoms are too unstable to be used as building blocks[48-50].

Beyond metallic clusters, a wide range of magnetic states are experimentally accessible in binary superatoms[51]. Metal oxide clusters often exhibit large spin states resulting from the coupling of the metal spins through superexchange[52]. Heavier chalcogens can also promote strong magnetic coupling, leading to ferromagnetic or antiferromagnetic ground states[53]. A few theoretical studies have begun to explore the complex relationship between superatom composition, structure and charge state, and the resulting magnetic behaviour. For example, one such study recently demonstrated the theoretical magnetic tunability of the superatom $Ni_9Te_6(PR_3)_8$[40].

In a strategy related to that for magnetic metallic superatoms, new magnetic metal chalcogenide superatoms can be created by varying the core electron count via metal atom substitution. For instance, replacing one Re atom in the diamagnetic core of Re_6Se_8 with Os produces a S = ½ core[42].

Optical Properties

The optical properties of superatoms have received widespread attention ever since the octahedral Re_6Q_8 and Mo_6X_8 families were first shown to exhibit intense and long-lived photoemission[54-55]. These superatoms are particularly attractive building blocks because their emission energy can be tuned by modifying the composition or charge of the core, or substituting their capping ligands[56-57]. In a recent development, non-centrosymmetric Sn_4S_6 superatoms were

used to create a spectrally broadband and highly directional warm-white-light emitter that is driven by an inexpensive, low-power continuous-wave infrared laser diode[58].

1.4 Superatom Assembly and Superatomic Crystal Properties

Until recently, superatoms have been used infrequently as building blocks to create solid state materials[59-60]. In the past few years, however, superatomic crystals have received much attention, resulting in materials with broader compositions, structures and properties[7, 59]. In this section, we discuss several synthetic strategies to assemble superatoms into discrete oligomers with well-controlled configurations, as well as extended structures. We highlight the resulting collective material properties that emerge due to the inter-superatom coupling.

Discrete Oligomers of Superatoms

Developing the chemistry to make discrete oligomers from superatoms is a necessary first step to the formation of extended assemblies. Providing stability and solution processability, the capping ligands on the surface of superatoms are also the entry point to forming inner-sphere bonds. A powerful approach to create oligomers of superatoms is to design building blocks with differentiated sites, which can be selectively modified, dissociated or substituted post-synthesis. To form oligomers, these site-differentiated superatoms are connected together by bridging linkers or by fusion of the cores upon removal of reactive ligands.

Site-differentiated Superatoms and Bridged Dimers

By installing kinetically inert and labile ligands at certain positions, site-differentiated superatoms can be used to create covalently-linked dimers. This approach was first explored using the site-differentiated superatoms $[Re_6E_8(L)_{n(X_{(6-n)}}]^{(n-4)+}$, which are prepared from $[Re_6E_8X_6]^{3-/4-}$

by selectively substituting some of the halide ligands with various labile, reactive, or inert ligands[61]. For example, labile acetonitrile ligands installed on the core form the site-differentiated clusters $[Re_6Se_8(PR_3)_4(MeCN)_2]^{2+}$ [62]. Zheng and co-workers installed photolabile CO ligands to yield the $[Re_6Se_8(PEt_3)_{(6-n)}(CO)_n]^{2+}$ (n = 1 or 2) superatoms and found considerable back-bonding into the CO ligand by the superatom core[63]. These clusters have been used as building blocks for the creation of a variety of oligomers (including the dendrimer discussed in sections below) via ligand substitution[64-66].

A more recent example of such a strategy, shown in Figure 1.3a, b, employs the carbonylated superatoms $Co_6Se_8(CO)_x(PEt_3)_{6-x}$[67]. The important finding that enabled isolation of these site-differentiated clusters was that an excess of elemental Se in combination with $Co_2(CO)_8$ and a phosphine yields a distribution of carbonylated products that can be easily separated by traditional silica gel chromatography or fractional crystallization. The CO group is a synthetically useful handle that can be easily manipulated. The Co_6Se_8 cores can be dimerized by replacing the CO with a rigid ditopic linker such as 1,4-phenylene diisocyanide (CNC_6H_4NC) (Figure 1.3a). This bridging strategy gives rise to a diversity of superatom dimer structures simply by varying the linking group and allows weakly coupled dimers to be studied. This approach has been championed as a breakthrough in nanoscience[68].

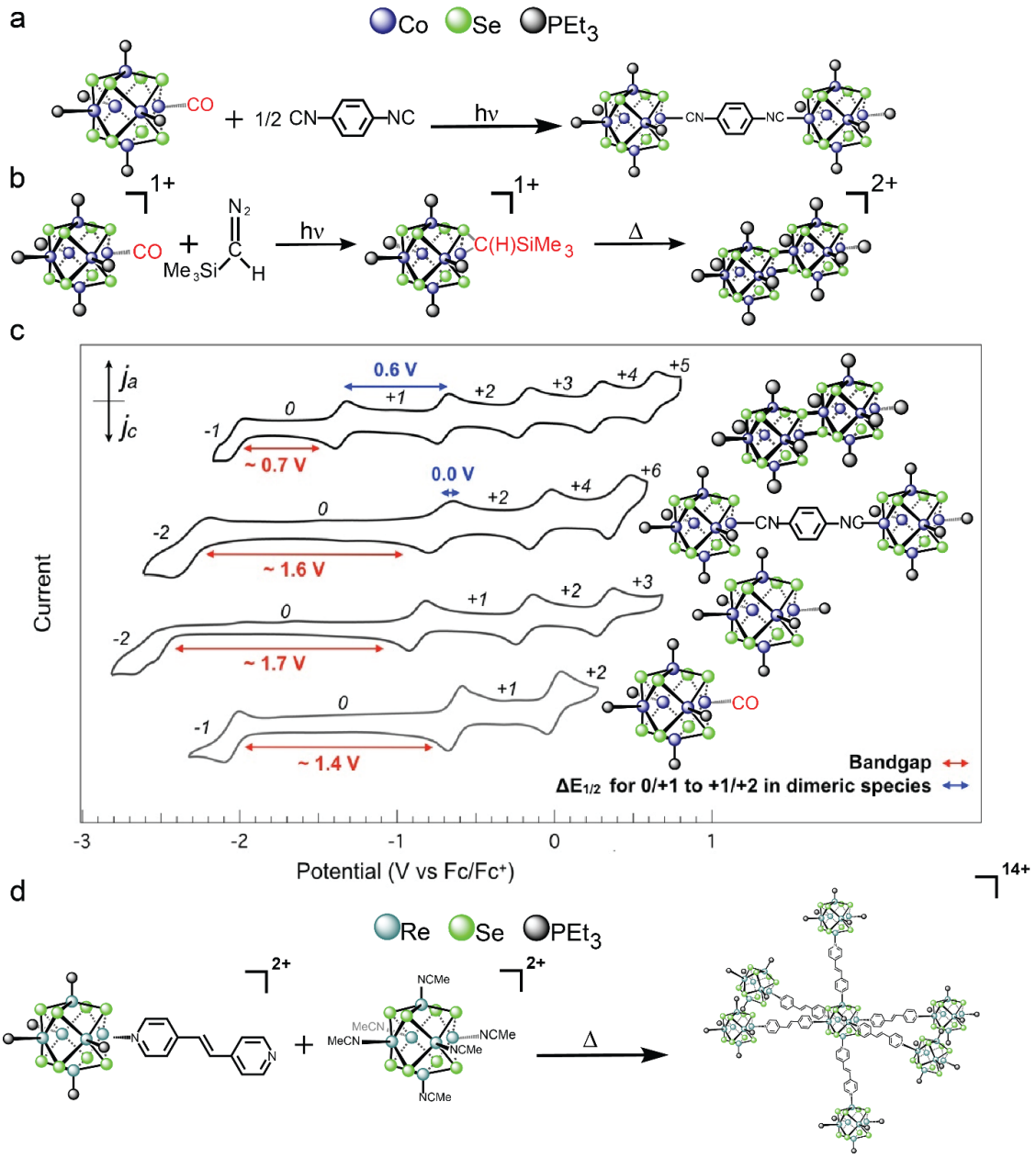

Figure 1.3: Oligomerization of superatoms. **a.** Formation of a superatom dimer using the site-differentiated superatom $Co_6Se_8(PEt_3)_5(CO)$ and the bridging ligand 1,4-phenylene diisocyanide[67]. **b.** Synthesis of a fused dimer by reacting the site-differentiated superatom $Co_6Se_8(PEt_3)_5(CO)$ with trimethylsilyldiazomethane69. **c.** Cyclic voltammograms of the superatoms $Co_6Se_8(PEt3)_5(CO)$ and $Co_6Se_8(PEt_3)_6$, the bridged dimer $Co_{12}Se_{16}(PEt_3)_{10}(CNC_6H_4NC)$ and fused dimer $Co_{12}Se_{16}(PEt_3)_{10}$. The red arrow shows the effective HOMO-LUMO, as estimated from CV and the blue arrow shows the ΔE1/2 for both dimer species[67, 69]. **d.** Synthesis of a superatom dendrimer from the site-differentiated superatom $[Re_6Se_8(PEt_3)_5(L)]^{2+}$ and $[Re_6Se_8(MeCN)_6]^{2+}$, where L = 1,2-di(4-pyridyl)ethylene[66].

Fused Dimers

While the ligand-bridging strategy allows superatom dimers to be studied in the weakly coupled limit, fusing them together leads to much stronger inter-superatom coupling. Until recently, there were only a few examples of discrete superatom fusion and these existing strategies are not generalizable[62, 70-73]. We have developed a novel chemical transformation to covalently expand the Co_6Se_8 core to a $Co_{12}Se_{16}$ core through direct fusion[69]. The key intermediate is obtained in one step, in high yield, from a carbonylated cluster and contains a carbene ligand that acts as a bifunctional protecting group for the Se and Co atoms involved in the subsequent fusion shown in Figure 1.3b. The combination of electronic and optical data and quantum chemical calculations reveal that the resulting dimer exhibits electronic coupling and electron delocalization.

The electrochemical properties of the Co_6Se_8 dimers depends on the type of inter-superatom linkage, as illustrated in Figure 1.3c. Both the $Co_6Se_8(PEt_3)_6$ and $Co_6Se_8(CO)(PEt_3)_5$ superatoms exhibit three reversible one-electron redox transformations. The CO ligand on the site-differentiated core, however, shifts the energy levels so that the charge states 0 to 3+ and 1– to 2+ are accessible for $Co_6Se_8(PEt_3)_6$ and $Co_6Se_{8(}CO)(PEt_3)_5$, respectively. Three redox couples are also observed for the diisocyanide-bridged dimer $Co_{12}Se_{16}(PEt_3)_{10}(CNC_6H_4NC)$ synthesized from $Co_6Se_{8(}CO)(PEt_3)_5$ precursors. The three redox couples come from the additive shuttling of two electrons, with each redox event corresponding to a two-electron process. The fused dimer $Co_{12}Se_{12}(PEt_3)_{10}$, however, displays a drastically different redox behaviour: the cyclic voltammogram shows five distinct and reversible one-electron events giving access to the 1– to 5+ charge states. Accessing more redox states a result of the direct coupling of superatomic cores.

Dendrimers

Beyond dimers of superatoms, the next frontier is the controlled formation of larger discrete oligomers of superatoms. Work in this area has once again focused on the Re_6Se_8 and Co_6Se_8 systems.

The dendrimer prepared by Zheng and co-workers (Figure 1.3d) is a remarkable synthetic achievement[74-75]. It is prepared by reacting six equivalents of the site-differentiated unit $[Re_6Se_8(PEt_3)_5(L)]^{2+}$ (L is a ditopic 1,2-di(4-pyridyl)ethylene ligand) with one equivalent of $[Re_6Se_8(MeCN)_6]^{2+}$. The labile acetonitrile ligands are substituted with the pyridine group, leading to the coupling of the superatomic units.

The assembly of superatoms into dendrimers leads to unexpected electrochemical behaviours. Cyclic voltammetry shows two oxidation events: a reversible oxidation of the central cluster at 1.26 V vs. SCE and a second irreversible oxidation attributed to the surrounding six clusters occurring at 1.91 V vs. SCE[74]. The noteworthy feature of the dendrimer is that the electrostatic environment provided by the six outer cationic units shifts the energy levels of the central unit.

Superatom Trimers

Trimers can be prepared via a stepwise ligand substitution strategy. For instance, trimers of Co_6Se_8 are prepared by reacting *trans*-$Co_6Se_8(CNC_6H_4NC)_2(PEt_3)_4$ (formed from *trans*-$Co_6Se_8(CO)_2(PEt_3)_4$) with two site-differentiated $Co_6Se_8(CO)(PEt_3)_5$ units to link them together via photodissociation of the CO ligand[67]. This approach was also previously successful using the site-differentiated $[Re_6E_8(L)_{n(}X_{(6-n)}]^{(n-4)+}$ superatoms described above[64]. This is a general strategy that is currently being explored to make 1D wires with a diversity of core structures.

Extended Structures of Superatoms

Many strategies can be used to assemble superatoms into extended structures. These includes ligand-ligand interactions, bridging ligands, inter-superatom charge transfer and molecular recognition. We divide this section into materials comprising only one component and those comprising multiple building units.

Monocomponent Superatomic Crystals and Soft Materials

Monocomponent superatomic crystals and soft materials display properties that depend not only on the identity of the superatom but also on how these superatoms are arranged in a lattice or matrix and how they couple to each other.

Ligand-ligand Interactions

Capping ligands on the superatoms can direct the assembly of the superatomic crystals, and can influence the resulting collective properties. In a recent report, Li and co-workers installed two 1,1-bis(diphenylphosphino)methane (PCP) ligand on Au_{21} that act as "hooks" to link neighboring superatoms together through π–π and π–anion interactions[76] (Figure 1.4a). This ligand modification allows for the formation of 1D nanofibrils that further assemble into a 3D superatomic crystal. This process results in a material with tunable electrical conductivity: by changing the counterions used in the assembly, the electrical conductivity can be modulated by over two orders of magnitude.

Ligands with functional groups can engage into specific inter-superatom interactions. In one illustrative study, *p*-mercaptobenzoic acid (p-MBA) ligands were used to assemble the silver superatom $Ag_{44}(p\text{-}MBA)_{30}$ into a crystalline structure held together by H-bonds[77]. These interactions were investigated using first-principles calculations and are predicted to lead to a

cooperative, chiral mechanical response in which the clusters rotate in concert in the same direction when an external pressure is applied, akin to meshing gears rotating.

In another example, Nonappa and co-workers[78] synthesized cobalt nanoparticles also using p-MBA ligands and with a narrow size distribution. These nanoparticles then further assemble into spherical capsid superstructures also through H-bonding interactions. These capsid superstructures were shown to be reversibly assembled and disassembled through heating or through solvent interactions. Remarkably, these capsid structures can be further assembled using magnetic-field-directed self-assembly into various superstructures due to the magnetic nature of the cobalt nanoparticles.

Superatomic Liquid Crystals or Clustomesogens

Although not crystalline solids, superatomic liquid crystals or clustomesogens are an interesting class of monocomponent superatomic "crystals". These materials are unique in that they combine favorable photoluminescent and magnetic properties displayed by superatoms with the versatility of liquid crystals. Extensive work by Molard and Cordier have demonstrated numerous synthetic approaches to obtain clustomesogens as well as a range of exciting optical and magnetic properties. In one example, $[Mo_6Br_8F_6]^{2-}$ superatomic cores were functionalized with gallic-acid-derived ligands forming a liquid crystalline phase which retained a strong red/near infrared (NIR) luminescence with only a slight shift (~10 nm) in the emission maximum[79]. In another example, $KCs_3[Re_6Se_8(CN)_6]$ superatoms undergo cation metathesis with dialkyldimethylammonium cations to form a liquid crystalline phase[80]. When Br_2 was used to oxidize the superatomic core, a paramagnetic clustomesogen was obtained. This paramagnetic

state was found to be switchable through electrochemical processes and was not affected by the mesogenic cations.

Superatom-containing Polymers

Similarly to the clustomesogens described above, polymers that have incorporated superatom cores through covalent interactions with the polymerizable monomer or other interactions have been investigated. These superatom-containing polymers retain the desired properties of the superatoms and the macromolecular backbone imparts processability typical of polymers. One such polymer was prepared by treating the $[Re_6Se_8(OH)_6]^{4-}$ core with *tert*-butylpyridine (TBP) and methacrylic acid (MAC) to give the polymerizable superatom $Re_6Se_8(TBP)_4(MAC)_2$. This polymerizable superatomic unit could then undergo radical polymerization with excess methyl methacrylate monomer to yield a Re_6Se_8 containing crosslinked polymer network[81]. Anionic superatoms can also be joined to polymerizable cationic monomers through coulombic interactions[82]. Following polymerization, the resulting polymer matrix can include high loading levels of superatoms, which act as crosslinking units between polymer chains while retaining their red-NIR photoluminescent properties.

Using Block Copolymers to Assemble Superatoms

The approach discussed above to prepare and functionalize the site-differentiated $Co_6Se_8CO(PEt_3)_5$ cluster[67] has enabled the development of a new family of superatom-containing diblock copolymers that can template the formation of microstructures such as vesicles[83]. A polymerizable monomer based on norbornene is first tethered to the Co_6Se_8 core through substitution of the photolabile carbonyl ligand. This monomer is then polymerized sequentially

through ring-opening metathesis polymerization (ROMP) with another block to create the superatom-containing diblock copolymer shown in Figure 1.4b.

The integration of superatoms into a well-defined block copolymer opens new possibilities to direct their assemblies into mesoscale structures. The diblock copolymer shown in Figure 1.4b is composed of two immiscible blocks: a hydrophilic, cationic superatom-containing block and a hydrophobic, cross-linkable cinnamoyl-containing block. In non-polar solvent mixtures, this diblock copolymer self-assembles to form microscale vesicles (Figure 1.4c, d). The cationic superatoms are contained within the hydrophobic vesicle walls, which can be further crosslinked by taking advantage of the photo-reactivity of the cinnamoyl-moieties. Moreover, we have demonstrated that these vesicles can be used to encapsulate molecular cargo such methylene blue.

The electrochemical properties of the polymer are controlled by its self-assembly behaviour. In N,N-dimethylformamide, the diblock copolymer does not self-assemble and three different charge states (neutral, 1+, 2+) of the tethered superatom are accessible through two reversible redox events. However, when the diblock copolymer self-assembles into vesicles, the superatom is confined within hydrophobic bilayer walls, thus inhibiting the electron transfer and silencing the redox activity of the superatom[83].

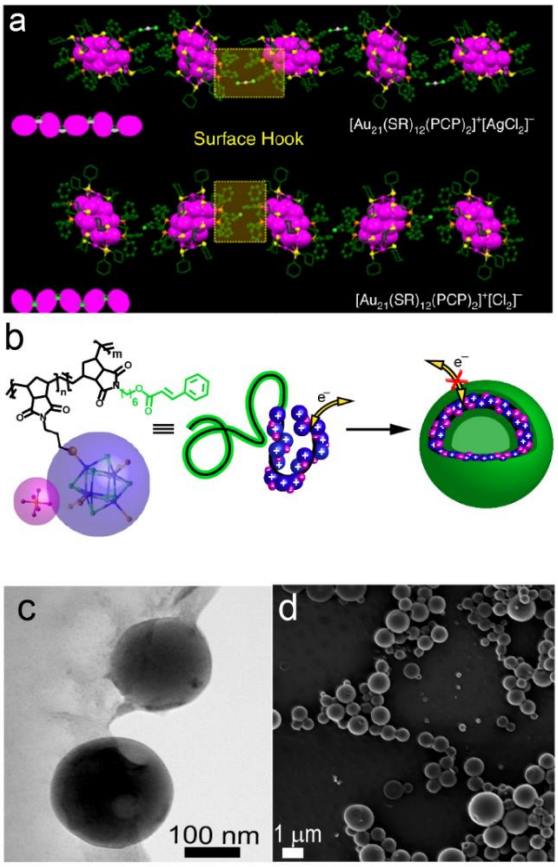

Figure 1.4: Monocomponent assemblies of superatoms. **a.** Packing of $[Au_{21}(SR)_{12}(PCP)_2][AgCl_2]$ (top) and $[Au_{21}(SR)_{12}(PCP)_2][Cl]$ (bottom) in 1D assemblies with ligands serving as hooks. Colour code: Au, Magenta; Ag, gray; Cl, light green; S, yellow; P, orange; C, green. Yellow boxes highlight surface hooks. Reproduced from [76] **b.** Structure of the superatom-containing diblock copolymer and schematic of its self-assembly into vesicles. The cinnamoyl block is shown in green and the cluster is shown in blue, with its counterion in pink. The dissolved diblock copolymer is able to reversibly access three redox states, but the self-assembled diblock copolymer is no longer redox-active. Colour code: Co, blue; Se, green; P, orange; F, magenta; C, black. Substituents on the phosphines are removed to clarify the view. **c.** Transmission electronic microscopy image and **d.** scanning electronic microscopy images of vesicles assembled from the superatom-containing diblock copolymer shown in Figure 1.4b. **b-d** reproduced from [83].

Superatomic Crystals from Charge Transfer Assembly

The creation of superatomic crystals assembled from several components were inspired by earlier work by Batail and co-workers on inorganic-organic hybrid materials. The cyanide-

functionalized cluster $[Re_6Se_8(CN)_6]^{4-}$ was used as a building block to assemble the crystalline solid $(EDT\text{-}TTF\text{-}CONH_2)_6[Re_6Se_8(CN)_6]$ ($EDT\text{-}TTF\text{-}CONH_2$ = amide-functionalized ethylenedithiotetrathiafulvalene), which adopts a Kagome lattice[84]. The terminal cyanide ligands on the superatom are key in directing the formation of the Kagome lattice through H-bonding interactions. A series of related atomically precise materials have been reported using various clusters with the M_6E_8 motifs, which are combined with organic electroactive molecules such as TTF and TCNQ[73, 85-87].

Building on this foundation, our team has created a new family of binary superatomic crystals assembled from metal chalcogenide superatoms and fullerenes[88] held together by charge transfer interactions. We have since expanded this concept into a vast library of multicomponent crystals formed by combining structurally and electronically complementary superatoms[59]. In this section, we will discuss the assembly of these materials as well as their physical properties.

Superatomic Crystals Comprising Metal Oxide Clusters

Beyond fullerenes, multicomponent superatomic crystals can be assembled from electronically complementary inorganic building blocks, including metal chalcogenide, metal oxide and metal halide superatoms. For instance, combining the electron-donating $Co_6Se_8(PEt_3)_6$ and electron-accepting $Fe_8O_4pz_{12}Cl_4$ in toluene forms black single crystals of $[Co_6Se_8(PEt_3)_6][Fe_8O_4pz_{12}Cl_4]$ [36] whose primitive cubic lattice can be approximated as the superatomic analog of the CsCl lattice (Figure 1.5b). Substitution of the phosphines, halides and/or chalcogens can produce subtle changes to the atomic structure of the binary solids or entirely new packing structures. The compounds $[Co_6Se_8(PEt_3)_6][Fe_8O_4pz_{12}Cl_4]$, $[Co_6Te_8(PEt_3)_6][Fe_8O_4pz_{12}Cl_4]$, $[Co_6Te_8(PEt_2Ph)_6][Fe_8O_4pz_{12}Cl_4]$ and

$[Co_6Te_8(PEt_3)_6][Fe_8O_4pz_{12}Br_4]$ all form the same CsCl packing structure, with slight differences in the orientation of the superatoms. $[Co_6Te_8(P^nPr_3)_6][Fe_8O_4pz_{12}Cl_4]$, by contrast, adopts an entirely different and highly unusual superstructure in which the two superatoms form alternating hexagonal close-packed layers with an *hccc* packing stacking sequence. These examples demonstrate how modification of the superatoms allows subtle tuning of the superstructure.

Superatomic Crystals Assembled from Molecular Recognition

In addition to electrostatic interactions resulting from inter-superatom charge transfer, multicomponent crystals can be assembled using molecular recognition motifs. We discuss an example in which a superatom decorated with phenanthrene groups is used as a nanoscale director to form a layered van der Waals solid, which can be exfoliated, akin to conventional atomic van der Waals materials[89]. Figure 1.5c is a side view of $Co_6Se_8(PEt_2phen)_6$ illustrating how the phenanthrene ligands extend, rotate and organize to form two antipodal buckybowls interacting with C_{60}, thus creating a dumbbell unit that templates the extended layered structure. The resulting bulk solid, $[Co_6Se_8(PEt_2phen)_6][C_{60}]_5$, contains two distinct layers: a hybrid cluster-fullerene layer (CL) in which each cluster is surrounded by two C_{60}, and a layer composed exclusively of close-packed neutral fullerenes (FL). Unlike charge transfer assemblies, the layers in $[Co_6Se_8(PEt_2phen)_6][C_{60}]_5$ are held together by relatively weak van der Waals forces.

By analogy to graphene and transition metal dichalcogenides, single crystals of $[Co_6Se_8(PEt_2phen)_6][C_{60}]_5$ can be exfoliated to produce nanosheet materials[90]. To enable exfoliation, the structure needs to be mechanically strengthened. This is accomplished by photopolymerizing the close-packed C_{60} layers FL within the structure. Once crosslinked, the crystals are dissolved to release nanosheets of the material, which can be collected on a substrate.

Figure 1.5d shows an atomic force microscopy (AFM) image of an isolated nanosheet after exfoliation and deposited onto a Si/SiO_2 substrate. The 5 nm step height for the nanosheet (Figure 1.5d, bottom) indicates that the 2D material in a sandwich of FL/CFL/FL. Remarkably, the exfoliated 2D photopolymerized material can be reverted back to its pristine molecular state by thermal depolymerization at 450 K.

Assembling superatoms into synthetic 2D materials offers exciting opportunities for tuning the material properties through chemical design and for discovering new behaviours. As a bulk crystal, $[Co_6Se_8(PEt_2phen)_6][C_{60}]_5$ exhibits in-plane activated electrical transport behaviour with an activation energy of 0.40 eV[89]. The optical gap of the material, estimated from electronic absorption spectroscopy, is 0.39 eV (Figure 1.5e). Upon photopolymerization and exfoliation, the nanosheets behave as a direct bandgap semiconductor with an optical gap of ~0.25 eV[90]. This unusual reduction of the optical gap in the 2D limit suggests that the C_{60} layers in the parent structure are electronically decoupled from each other. The effect is instead attributed to shorter intermolecular distances, resulting from the polymerization of the C_{60} layer. The decrease in C_{60}–C_{60} distance enhances the coupling between C_{60} units and thus reduces the gap.

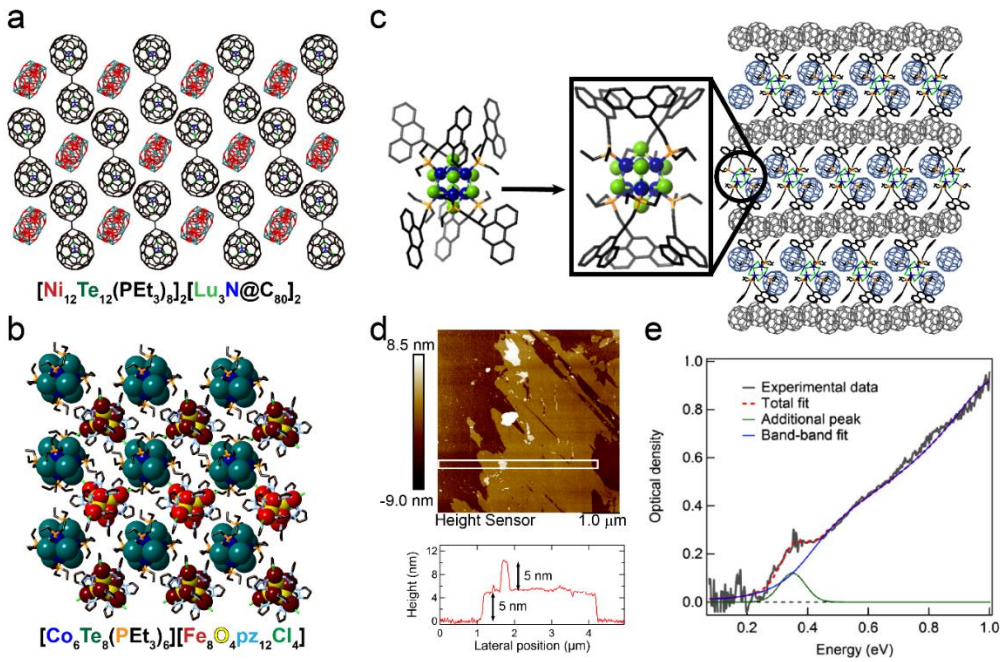

Figure 1.5: Multicomponent superatomic crystals. **a.** Wireframe representation of the crystal structure of $[Ni_{12}Te_{12}(PEt_3)_8]_2[Lu_3N@C_{80}]_2$ [91]. **b.** Space-filling representation of the crystal structure of $[Co_6Te_8(PEt_3)_6][Fe_8O_4pz_{12}Cl_4]$ [36]. Colour code for **a, b** as indicated by the chemical formulas. Capping ligands in **a** and H atoms in **b** are removed to clarify the views. **c.** Assembly of $Co_6Se_8(PEt_2Phen)_6$ and C_{60} into the layered van der Waals superatomic crystal $[Co_6Se_8(PEt_2phen)_6][C_{60}]_5$. Molecular structures of the nanoscale director before and after self-assembly are shown, along with an edge-on view of the crystal packing of $[Co_6Se_8(PEt_2phen)_6][C_{60}]_5$. Colour code: Co, blue; Se, light green; P, orange; C, black. The fullerenes in superatom containing layer are shown in light blue. Hydrogen atoms are removed to clarify the view. Adapted from [89]. **d.** AFM image and height profile of a nanosheet exfoliated from the crystal $[Co_6Se_8(PEt_2phen)_6][C_{60}]_5$ shown in **c** and transferred to a Si/SiO2 substrate. The step height of 5 nm corresponds to one complete layer of the structure. Adapted from [90]. **e.** Mid-IR absorption spectrum of $[Co_6Se_8(PEt_2phen)_6][C_{60}]_5$. The red dashed curve was obtained from a fit using band-to-band transition for semiconductor (blue) with an additional Gaussian peak (green) near the band-edge. The obtained bandgap is 0.39 eV[89].

1.5 Multicomponent Covalent Superatomic Materials

To create superatomic crystals with strong electronic coupling, it is required to covalently link the superatoms. The formation of such extended structures remains a major synthetic challenge. In this section, we discuss major advances in that direction.

Superatomic Prussian Blue Analogs

In addition to directing the assembly of superatoms through H-bonding interactions, cyanide ligands can also be used in a bridging configuration to form 3D coordination frameworks analogous to Prussian Blue (PB). For instance, cyanide-caped octahedral superatoms such as $[M_6E_8(CN)_6]^{n-}$ (M = Re, Mo, W; E = S, Se, Te) and $[M_6Cl_{12}(CN)_6]^{n-}$ (M = Nb, Ta) can replace the traditional atomic building block, $[Fe(CN)_6]^{4-}$, to form cluster-expanded PB analogs. Examples include $Fe_4[Re_6Te_8(CN)_6]_3$, $Ga_4[Re_6Se_8(CN)_6]_3$, $Cs_2Mn_3[Re_6Se_8(CN)_6]_2$, $Co_3[Re_6Se_8(CN)_6]_2$, and $(Me_4N)_2Mn[Nb_6Cl_{12}(CN)_6]$, which crystallize in the prototypical cubic lattice (Figure 1.6a)[32, 92-94].

More exotic superatom-based PB frameworks can also be produced. The superexpanded framework $Cs_2[$*trans*-$Fe(H_2O)_2]_3[Re_6Se_8(CN)_6]_2$ is a layered structure composed of the CN-bridged bimetallic sheets $\{[$*trans*-$Fe(H_2O)_2][Re_6S_8(CN)_6]\}^{2-}$ [93]. Another example is the ternary PB analog $[Fe(CN)_6(Mn($*salen*$))_6Nb_6Cl_{12}(CN)_6]$, which connects Fe and Mn ions with the Nb_6Cl_{12} unit into a crystalline cubic lattice[32]. Recent work by Zhang and Lachgar have continued to investigate ternary superexpanded PB analogues by synthesizing more compositionally diverse structures[95]. In these materials the superatomic units consist of $[Nb_6Cl_{12}(CN)_6]^{4-}$ or $[Ta_6Cl_{12}(CN)_6]^{3-}$ cores and the mononuclear metal cyanide complexes include $[Fe(CN)_6]^{4-}$, $[Cr(CN)_6]^{3-}$, $[Fe(CN)_5(NO)]^{2-}$, or $[Ni(CN)_4]^{2-}$. Using the same CN-bearing superatomic units, frameworks with various 1D, 2D, and 3D structures are accessible by varying the ratio and topology of building blocks[96].

With the exception of the $[Ta_6Cl_{12}(CN)_6]^{3-}$ core, one major limitation with the materials discussed above is that the superatomic units are all diamagnetic, precluding the observation of long-range magnetic coupling and phase transitions. To access superatomic solids with long-range magnetic ordering, Long and Batail have synthesized a family of paramagnetic superatoms $[Re_{6-}$

$_nOs_nSe_8(CN)_6]^{(5-n)-}$ and showed that these can couple ferromagnetically to transition metal ions bound to the cyanide at the N-terminus[97].

Superatomic Coordination Frameworks

Many metal-organic framework (MOF) synthetic strategies use clusters as secondary building units, however these are typically formed *in situ* during the growth of the structure, precluding *ex situ* tuning of the properties[98]. Zheng showed that low-dimensional coordination polymers can be formed by linking Re_6Se_8 superatomic cores using bipyridine bridging ligands[66]. In a related approach, we recently illustrated an application of carboxylic acid-based synthetic strategies typically used in MOFs to create 2D and 3D frameworks from preformed carboxylic acid-functionalized Co_6Se_8 superatoms[99]. This methodology combines the chemistry of molecular clusters and metal-organic frameworks. The hexatopic carboxylic acid cluster $Co_6Se_8[PEt_2(4\text{-}C_6H_4COOH)]_6$ reacts with Zn^{2+} ions in solvothermal reactions to form a crystalline superatomic molecular framework with carboxylate-zinc-carboxylate nodes. Different solvent conditions in the synthesis tune the dimensionality of the resulting networks from (Figure 1.6b, c) [99].

The layered structure shown in Figure 1.6c can be chemically exfoliated and the resulting nanosheets retain the redox activity of their constituent superatoms[99]. The cyclic voltammogram of the nanosheets deposited on an electrode shows three reversible oxidations, corresponding to the 0, 1+, 2+ and 3+ states of the Co_6Se_8 core. Thus, the redox-active nanosheets are solution-processable and exfoliation retains the open channels and solvent-accessible void space.

Polymerization of Superatoms into Woven Materials

A relatively unexplored yet powerful technique to assemble superatoms into atomically precise extended structures is electrocrystallization. This approach assembles molecular ions from

solution into ordered solid state crystals at an electrode by slowly oxidizing electroactive compound in the presence of an electrolyte. Previously employed by Batail to form the Kagome structures from with $[Re_6Se_8(CN)_6]^{4-}$ [84], this method was recently applied to site-differentiated *trans*-$Co_6Se_8(CNC_6H_4NC)_2(PEt_3)_4$, which oxidize in the presence of a shape complementary anionic template ($Mo_6O_{19}^{2-}$) to yield covalent 2D interwoven superatom polymer strands (Figure 1.6e)[100]. The resulting box weave stacks in two-dimensional layers with layers of the anionic cluster filling the void space of the weave. The crossing point of the weaving strands is comprised of π-π stacking of the diisocyanide linkers. This material demonstrates unprecedented complexity at the nanoscale, in which covalently linked Co_6Se_8 cores further interact via weaving.

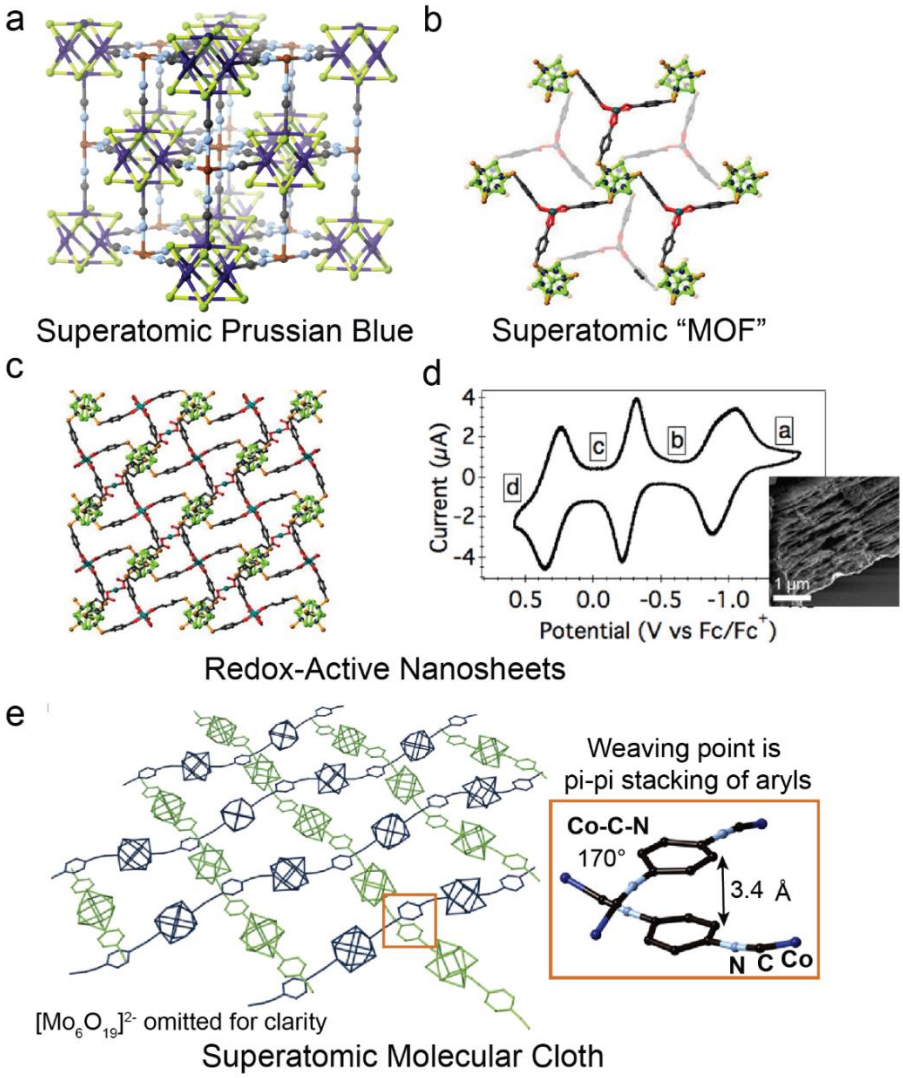

Figure 1.6: Covalent superatomic crystals. **a.** Crystal structure of the superatomic Prussian Blue analog $Fe_4[Re_6Se_8(CN)_6]_3 \cdot 36H_2O$. Colour code: Re, dark purple; Se, light green; Fe, maroon; N, light blue; C, black. Adapted from [101]. **b.** Crystal structure of the 3D superatomic coordination framework obtained from the reaction of $Co_6Se_8[PEt_2(4\text{-}C_6H_4COOH)]_6$ with $Zn(NO_3)_2$ [99]. Colour code: Co, blue; Se, green; Zn, teal; P, orange; C, black; O, red. **c.** Crystal structure of the layered superatomic coordination framework obtained from the reaction of $Co_6Se_8[PEt_2(4\text{-}C_6H_4COOH)]_6$ with $Zn(NO_3)_2$ [99]. Colour code is the same as for **b**. **d.** Solid-state cyclic voltammogram of nanosheets exfoliated from the crystal shown in **c**. The solution of exfoliated sheets was dropcast onto a glassy carbon electrode and the voltammogram was collected at 50 mV/s. **e.** Wireframe representation of the crystal structure of the electrocrystallized superatomic crystal $\{[Co_6Se_8(PEt_3)^{4+}](CNC_6H_4NC)\}_2[Mo_6O_{19}^{2-}]$. A single layer is shown. The two-dimensional sheets are templated by the anionic cluster, which stacks in the void space of the cloth material in alternating layers. The crossing point of the individual polymeric strands is π-π stacking of the diisocyanide linker. Adapted from [100].

1.6 Conclusion and Outlook

This chapter highlights the great potential of superatoms in the fabrication of functional materials. Superatomic crystals provide a bridge between traditional semiconductors, molecular solids, and nanocrystal arrays by combining tunability and atomic precision. The ultimate vision is to be able to create materials with tailored and tunable functions through the judicious design, synthesis and assembly of the superatoms. To this end, the literature is rich with a library of molecular clusters possessing a host of attractive properties for use as superatoms, including redox activity, large magnetic moments, and luminescence. Additionally, the field of molecular cluster science is thriving with new cluster species being synthesized that could be used as potential superatoms. Researchers interested in the creation of new materials from superatoms must always be watchful for potential candidates.

Much remains to be learned about the assembly of superatoms into superatomic crystals, and the relation between their structures and physical properties. The assembly strategies outlined above are a small fraction of potential synthetic approaches and there is a vast library of approaches that have yet to be explored for the creation of new materials. The observation that collective behaviours and phase transitions can emerge in such materials as a result of their atomic precision opens the door to a particularly rich area of exploration.

In our opinion, there are two major challenges that must be tackled if this field is to continue its progression. First, new general approaches to assemble superatoms into oligomers and extended structures are required. Particular emphasis should be placed on creating strongly coupled materials. In this context, the use of radical-containing bridging ligands to facilitate communication between superatoms or the selective removal of ligands to promote the formation

of core-core linkages could be fruitful avenues of exploration. As additional superatoms and assembly strategies are developed, many more potential avenues could emerge. Second, as new superatomic crystals are developed, more emphasis should be placed on exploring their collective material properties. There are several examples of superatomic crystals whose material properties have yet to be explored. One example is the previously discussed electrocrystallized molecular cloth $\{[Co_6Se_8(PEt_3)^+](CNC_6H_4NC)\}_2[Mo_6O_{19}^{2-}]$ [100], which could have exciting physical and chemical properties due to its unique structure.

In the following chapters, the development and exploration of a potential family of NHC-based ligands for superatoms will be explored. An investigation into several relevant materials properties of NHCs is presented and discussed as well as methods for installation of those ligands onto existing superatoms. Also, the synthesis and characterization of a potentially new family of superatoms containing a nickel-phosphinidine core will be investigated. The following work expands upon the rich chemistry of superatoms and their use in materials presented in this chapter.

1.7 References

1. Collier, C. P.; Vossmeyer, T.; Heath, J. R., Nanocrystal superlattices. *Annual Review of Physical Chemistry* **1998,** *49*, 371-404.

2. Shevchenko, E. V.; Talapin, D. V.; Kotov, N. A.; O'Brien, S.; Murray, C. B., Structural diversity in binary nanoparticle superlattices. *Nature* **2006,** *439*, 55-59.

3. Auyeung, E.; Cutler, J. I.; Macfarlane, R. J.; Jones, M. R.; Wu, J. S.; Liu, G.; Zhang, K.; Osberg, K. D.; Mirkin, C. A., Synthetically programmable nanoparticle superlattices using a hollow three-dimensional spacer approach. *Nature Nanotechnology* **2012,** *7*, 24-28.

4. Khanna, S. N.; Jena, P., Atomic clusters: Building blocks for a class of solids. *Phys Rev B Condens Matter* **1995,** *51*, 13705-13716.

5. Bergeron, D. E.; Castleman, A. W.; Morisato, T.; Khanna, S. N., Formation of Al13I-: Evidence for the superhalogen character of Al-13. *Science* **2004,** *304*, 84-87.

6. Reber, A. C.; Khanna, S. N., Superatoms: Electronic and Geometric Effects on Reactivity. *Accounts of Chemical Research* **2017,** *50*, 255-263.

7. Jena, P.; Sun, Q., Super Atomic Clusters: Design Rules and Potential for Building Blocks of Materials. *Chemical Reviews* **2018,** *118*, 5755-5870.

8. Steigerwald, M. L., Clusters as Small Solids. *Polyhedron* **1994,** *13*, 1245-1252.

9. Dance, I.; Fisher, K., Metal Chalcogenide Cluster Chemistry. *Progress in Inorganic Chemistry, Vol 41* **1994,** *41*, 637-803.

10. MacDonald, D. G.; Corrigan, J. F., Metal chalcogenide nanoclusters with 'tailored' surfaces via 'designer' silylated chalcogen reagents. *Philosophical Transactions of the Royal Society a-Mathematical Physical and Engineering Sciences* **2010,** *368*, 1455-1472.

11. Pfund, A. H., Bismuth black and. its applications. *Review of Scientific Instruments* **1930,** *1*, 397-399.

12. Knight, W. D.; Monot, R.; Dietz, E. R.; George, A. R., Stern-Gerlach Deflection of Metallic-Cluster Beams. *Physical Review Letters* **1978,** *40*, 1324-1326.

13. Dietz, T. G.; Duncan, M. A.; Powers, D. E.; Smalley, R. E., Laser Production of Supersonic Metal Cluster Beams. *Journal of Chemical Physics* **1981,** *74*, 6511-6512.

14. Knight, W. D.; Clemenger, K.; Deheer, W. A.; Saunders, W. A.; Chou, M. Y.; Cohen, M. L., Electronic Shell Structure and Abundances of Sodium Clusters. *Physical Review Letters* **1984,** *52*, 2141-2143.

15. Bondybey, V. E.; English, J. H., Laser-Induced Fluorescence of Metal-Clusters Produced by Laser Vaporization - Gas-Phase Spectrum of Pb-2. *Journal of Chemical Physics* **1981,** *74*, 6978-6979.

16. Abreu, M. B.; Powell, C.; Reber, A. C.; Khanna, S. N., Ligand-Induced Active Sites: Reactivity of Iodine-Protected Aluminum Superatoms with Methanol. *Journal of the American Chemical Society* **2012,** *134*, 20507-20512.

17. Palmer, R. E.; Cai, R. S.; Vernieres, J., Synthesis without Solvents: The Cluster (Nanoparticle) Beam Route to Catalysts and Sensors. *Accounts of Chemical Research* **2018,** *51*, 2296-2304.

18. Crawford, N. R. M.; Hee, A. G.; Long, J. R., Cluster synthesis via ligand-arrested solid growth: Triethylphosphine-capped fragments of binary metal chalcogenides. *Journal of the American Chemical Society* **2002,** *124*, 14842-14843.

19. Fenske, D.; Ohmer, J.; Hachgenei, J.; Merzweiler, K., New Transition-Metal Clusters with Ligands from Main Group-5 and Group-6. *Angewandte Chemie-International Edition* **1988,** *27*, 1277-1296.

20. Chakraborty, I.; Pradeep, T., Atomically Precise Clusters of Noble Metals: Emerging Link between Atoms and Nanoparticles. *Chemical Reviews* **2017,** *117*, 8208-8271.

21. Sokolov, M. N.; Abramov, P. A., Chalcogenide clusters of Groups 8-10 noble metals. *Coordination Chemistry Reviews* **2012,** *256*, 1972-1991.

22. Hidai, M.; Kuwata, S.; Mizobe, Y., Synthesis and reactivities at cubane-type sulfido clusters containing noble metals. *Accounts of Chemical Research* **2000,** *33*, 46-52.

23. Cecconi, F.; Ghilardi, C. A.; Midollini, S., A Novel Paramagnetic Octahedral Iron Cluster - Synthesis and X-Ray Structural Characterization of [Fe6(Mu-3-S)8(Pet3)6][Bph4]2. *Journal of the Chemical Society-Chemical Communications* **1981**, 640-641.

24. Brennan, J. G.; Siegrist, T.; Stuczynski, S. M.; Steigerwald, M. L., The Transition from Molecules to Solids - Molecular Syntheses of Ni9te6(Pet3)8, Ni20te18(Pet3)12, and Nite. *Journal of the American Chemical Society* **1989,** *111*, 9240-9241.

25. Lee, S. C.; Holm, R. H., Nonmolecular Metal Chalcogenide Halide Solids and Their Molecular Cluster Analogs. *Angewandte Chemie-International Edition in English* **1990,** *29*, 840-856.

26. Speziali, N. L.; Berger, H.; Leicht, G.; Sanjines, R.; Chapuis, G.; Levy, F., Single-Crystal Growth, Structure and Characterization of the Octahedral Cluster Compound Re6se8br2. *Materials Research Bulletin* **1988,** *23*, 1597-1604.

27. Fischer, C.; Fiechter, S.; Tributsch, H.; Reck, G.; Schultz, B., Crystal-Structure and Thermodynamic Analysis of the New Semiconducting Chevrel Phase Re6s8cl2. *Berichte Der Bunsen-Gesellschaft-Physical Chemistry Chemical Physics* **1992,** *96*, 1652-1658.

28. Leduc, L.; Perrin, A.; Sergent, M., The Structure of Hexarhenium Dichloride and Octaselenide, Re6se8cl2 - a Bidimensional Compound of Re6 Octahedral Clusters. *Acta Crystallographica Section C-Crystal Structure Communications* **1983,** *39*, 1503-1506.

29. Mironov, Y. V.; Virovets, A. V.; Naumov, N. G.; Ikorskii, V. N.; Fedorov, V. E., Excision of the {Mo6Se8} cluster core from a chevrel phase: Synthesis and properties of the first

molybdenum octahedral cluster selenocyanide anions [Mo6Se8(CN)(6)](7-) and [Mo6Se8(CN)(6)](6-). *Chemistry-a European Journal* **2000,** *6*, 1361-1365.

30. Magliocchi, C.; Xie, X. B.; Hughbanks, T., A cyanide-bridged chain of Mo6Se8 clusters: A product of cyanide-melt cluster synthesis. *Inorganic Chemistry* **2000,** *39*, 5000-5001.

31. Bajan, B.; Meyer, H. J., Two-dimensional networks in the structure of Li-2[Nb6Cl16]. *Zeitschrift Fur Anorganische Und Allgemeine Chemie* **1997,** *623*, 791-795.

32. Zhang, J. J.; Lachgar, A., Superexpanded prussian-blue analogue with [Fe(CN)(6)](4-), [Nb6Cl12(CN)(6)](4-), and [Mn(salen)](+) as building units. *Journal of the American Chemical Society* **2007,** *129*, 250-251.

33. Cecconi, F.; Ghilardi, C. A.; Midollini, S.; Orlandini, A.; Zanello, P., Synthesis, properties and structures of the two "electron rich" cobalt-sulphur clusters [Co6(μ3-S)8(PEt3)6]1+,0. *Polyhedron* **1986,** *5*, 2021-2031.

34. Saito, T.; Yamamoto, N.; Nagase, T.; Tsuboi, T.; Kobayashi, K.; Yamagata, T.; Imoto, H.; Unoura, K., Molecular-Models of the Superconducting Chevrel Phases - Syntheses and Structures of [Mo6x8(Pet3)6] and [Ppn][Mo6x8(Pet3)6] (X = S, Se, Ppn = (Ph3p)2n). *Inorganic Chemistry* **1990,** *29*, 764-770.

35. Cecconi, F.; Ghilardi, C. A.; Midollini, S.; Orlandini, A.; Zanello, P., Redox behaviour of the iron–sulphur cluster [Fe6(μ3-S)8(PEt3)6]2+. Synthesis and crystal structure of the new paramagnetic monopositive species [Fe6(μ3-S)8(PEt3)6]+ as its [PF6]– salt. *Journal of the Chemical Society, Dalton Transactions* **1987**, 831-835.

36. Turkiewicz, A.; Paley, D. W.; Besara, T.; Elbaz, G.; Pinkard, A.; Siegrist, T.; Roy, X., Assembling Hierarchical Cluster Solids with Atomic Precision. *Journal of the American Chemical Society* **2014,** *136*, 15873-15876.

37. Reber, A. C.; Khanna, S. N.; Castleman, A. W., Superatom compounds, clusters, and assemblies: Ultra alkali motifs and architectures. *Journal of the American Chemical Society* **2007,** *129*, 10189-10194.

38. Chauhan, V.; Reber, A. C.; Khanna, S. N., Metal Chalcogenide Clusters with Closed Electronic Shells and the Electronic Properties of Alkalis and Halogens. *Journal of the American Chemical Society* **2017,** *139*, 1871-1877.

39. Chauhan, V.; Sahoo, S.; Khanna, S. N., Ni9Te6(PEt3)(8)C-60 Is a Superatomic Superalkali Superparamagnetic Cluster Assembled Material (S-3-CAM). *Journal of the American Chemical Society* **2016,** *138*, 1916-1921.

40. Reber, A. C.; Chauhan, V.; Khanna, S. N., Symmetry and magnetism in Ni9Te6 clusters ligated by CO or phosphine ligands. *Journal of Chemical Physics* **2017,** *146*.

41. Liu, G. X.; Pinkard, A.; Ciborowski, S. M.; Chauhan, V.; Zhu, Z. G.; Aydt, A. P.; Khanna, S. N.; Roy, X.; Bowen, K. H., Tuning the electronic properties of hexanuclear cobalt sulfide superatoms via ligand substitution. *Chemical Science* **2019,** *10*, 1760-1766.

42. Tulsky, E. G.; Long, J. R., Heterometal substitution in the dimensional reduction of cluster frameworks: Synthesis of soluble [Re6-nOsnSe8Cl6]((4-n)-) (n=1-3) cluster-containing solids. *Inorganic Chemistry* **2001,** *40*, 6990-7002.

43. Khanna, S. N.; Linderoth, S., Magnetic-Behavior of Clusters of Ferromagnetic Transition-Metals. *Physical Review Letters* **1991,** *67*, 742-745.

44. Kortus, J.; Baruah, T.; Pederson, M. R.; Ashman, C.; Khanna, S. N., Magnetic moment and anisotropy in FenCom clusters. *Applied Physics Letters* **2002,** *80*, 4193-4195.

45. Reveles, J. U.; Clayborne, P. A.; Reber, A. C.; Khanna, S. N.; Pradhan, K.; Sen, P.; Pederson, M. R., Designer magnetic superatoms. *Nature Chemistry* **2009,** *1*, 310-315.

46. Chauhan, V.; Medel, V. M.; Reveles, J. U.; Khanna, S. N.; Sen, P., Shell magnetism in transition metal doped calcium superatom. *Chemical Physics Letters* **2012,** *528*, 39-43.

47. Zhang, X. X.; Wang, Y.; Wang, H. P.; Lim, A.; Gantefoer, G.; Bowen, K. H.; Reveles, J. U.; Khanna, S. N., On the Existence of Designer Magnetic Superatoms. *Journal of the American Chemical Society* **2013,** *135*, 4856-4861.

48. Xu, X. S.; Yin, S. Y.; Moro, R.; de Heer, W. A., Magnetic moments and adiabatic magnetization of free cobalt clusters. *Physical Review Letters* **2005,** *95*.

49. Billas, I. M. L.; Chatelain, A.; Deheer, W. A., Magnetism from the Atom to the Bulk in Iron, Cobalt, and Nickel Clusters. *Science* **1994,** *265*, 1682-1684.

50. Cox, A. J.; Louderback, J. G.; Bloomfield, L. A., Experimental-Observation of Magnetism in Rhodium Clusters. *Physical Review Letters* **1993,** *71*, 923-926.

51. Datta, S.; Saha-Dasgupta, T., Structural, electronic and magnetic properties of transition metal binary alloy clusters with isoelectronic components: case study with MnmTcn, TimZrn and MnmRen. *Journal of Physics-Condensed Matter* **2013,** *25*.

52. Gatteschi, D.; Sessoli, R., Quantum tunneling of magnetization and related phenomena in molecular materials. *Angewandte Chemie-International Edition* **2003,** *42*, 268-297.

53. Bencini, A.; Midollini, S., Some Synthetic and Theoretical Aspects of the Chemistry of Polynuclear Transition-Metal Complexes. *Coordination Chemistry Reviews* **1992,** *120*, 87-136.

54. Gabriel, J. C. P.; Boubekeur, K.; Uriel, S.; Batail, P., Chemistry of hexanuclear rhenium chalcohalide clusters. *Chemical Reviews* **2001,** *101*, 2037-2066.

55. Maverick, A. W.; Gray, H. B., Luminescence and Redox Photochemistry of the Molybdenum(Ii) Cluster Mo6cl14(2-1). *Journal of the American Chemical Society* **1981,** *103*, 1298-1300.

56. Shestopalov, M. A.; Mironov, Y. V.; Brylev, K. A.; Kozlova, S. G.; Fedorov, V. E.; Spies, H.; Pietzsch, H. J.; Stephan, H.; Geipel, G.; Bernhard, G., Cluster core controlled reactions of substitution of terminal bromide ligands by triphenylphosphine in octahedral rhenium chalcobromide complexes. *Journal of the American Chemical Society* **2007,** *129*, 3714-3721.

57. Kitamura, N.; Ueda, Y.; Ishizaka, S.; Yamada, K.; Aniya, M.; Sasaki, Y., Temperature dependent emission of hexarhenium(III) clusters [Re-6(mu(3)-S)(8)X-6](4-) (X = Cl-, Br-, and I-): Analysis by four excited triplet-state sublevels. *Inorganic Chemistry* **2005,** *44*, 6308-6313.

58. Rosemann, N. W.; Eussner, J. P.; Beyer, A.; Koch, S. W.; Volz, K.; Dehnen, S.; Chatterjee, S., A highly efficient directional molecular white-light emitter driven by a continuous-wave laser diode. *Science* **2016,** *352*, 1301-1304.

59. Pinkard, A.; Champsaur, A. M.; Roy, X., Molecular Clusters: Nanoscale Building Blocks for Solid-State Materials. *Accounts of Chemical Research* **2018,** *51*, 919-929.

60. Castleman, A. W.; Khanna, S. N., Clusters, Superatoms, and Building Blocks of New Materials. *Journal of Physical Chemistry C* **2009,** *113*, 2664-2675.

61. Long, J. R.; McCarty, L. S.; Holm, R. H., A solid-state route to molecular clusters: Access to the solution chemistry of [Re(6)Q(8)](2+) (Q=S, Se) core-containing clusters via dimensional reduction. *Journal of the American Chemical Society* **1996,** *118*, 4603-4616.

62. Zheng, Z. P.; Long, J. R.; Holm, R. H., A basis set of Re6Se8 cluster building blocks and demonstration of their linking capability: Directed synthesis of an Re12Se16 dicluster. *Journal of the American Chemical Society* **1997,** *119*, 2163-2171.

63. Orto, P. J.; Nichol, G. S.; Wang, R. Y.; Zheng, Z. P., Cluster carbonyls of the [Re-6(mu(3)-Se)(8)](2+) core. *Inorganic Chemistry* **2007,** *46*, 8436-8438.

64. Zheng, Z. P.; Gray, T. G.; Holm, R. H., Synthesis and structures of solvated monoclusters and bridged di- and triclusters based on the cubic building block [Re-6(mu(3)-Se)(8)](2+). *Inorganic Chemistry* **1999,** *38*, 4888-4895.

65. Roland, B. K.; Selby, H. D.; Carducci, M. D.; Zheng, Z. P., Built to order: Molecular tinkertoys from the [Re-6(mu(3)-Se)(8)](2+) clusters. *Journal of the American Chemical Society* **2002,** *124*, 3222-3223.

66. Selby, H. D.; Roland, B. K.; Zheng, Z. P., Ligand-bridged oligomeric and supramolecular arrays of the hexanuclear rhenium selenide clusters-exploratory synthesis, structural characterization, and property investigationt. *Accounts of Chemical Research* **2003,** *36*, 933-944.

67. Champsaur, A. M.; Velian, A.; Paley, D. W.; Choi, B.; Roy, X.; Steigerwald, M. L.; Nuckolls, C., Building Diatomic and Triatomic Superatom Molecules. *Nano Letters* **2016,** *16*, 5273-5277.

68. Super-Molecules from Superatoms. *Scientific American* **2016,** *315*, 41-41.

69. Champsaur, A. M.; Hochuli, T. J.; Paley, D. W.; Nuckolls, C.; Steigerwald, M. L., Superatom Fusion and the Nature of Quantum Confinement. *Nano Letters* **2018,** *18*, 4564-4569.

70. Zheng, Z. P.; Holm, R. H., Cluster condensation by thermolysis: Synthesis of a rhomb-linked Re12Se16 dicluster and factors relevant to the formation of the Re24Se32 tetracluster. *Inorganic Chemistry* **1997,** *36*, 5173-5178.

71. Amari, S.; Imoto, H.; Saito, T., Synthesis of a molybdenum cluster complex [Mo-12(mu(3)-S)(14)(mu(4)-S)(2)(PEt3)(10)] with Chevrel phase type intercluster bondings. *Chemistry Letters* **1997**, 967-968.

72. Saito, T., Group 6 Metal Chalcogenide Cluster Complexes and their Relationships to Solid-State Cluster Compounds. In *Advances in Inorganic Chemistry*, Sykes, A. G., Ed. Academic Press: 1996; Vol. 44, pp 45-91.

73. Cecconi, F.; Ghilardi, C. A.; Midollini, S.; Orlandini, A., Dimerization of the Stellated Octahedral Unit Co6s8p6 - Synthesis and X-Ray Crystal-Structure of [Co12(Mu-3-S)14(Mu-4-S)2(Pet3)10][Tcnq]2, Where Tcnq = Tetracyanoquinodimethane. *Inorganica Chimica Acta* **1993,** *214*, 13-15.

74. Roland, B. K.; Carter, C.; Zheng, Z., Routes to Metallodendrimers of the [Re6(μ3-Se)8]2+ Core-Containing Clusters. *Journal of the American Chemical Society* **2002,** *124*, 6234-6235.

75. Roland, B. K.; Flora, W. H.; Selby, H. D.; Armstrong, N. R.; Zheng, Z. P., Dendritic arrays of [Re-6(mu(3)-Se)(8)](2+) core-containing clusters: Exploratory synthesis and electrochemical studies. *Journal of the American Chemical Society* **2006,** *128*, 6620-6625.

76. Li, Q.; Russell, J. C.; Luo, T. Y.; Roy, X.; Rosi, N. L.; Zhu, Y.; Jin, R. C., Modulating the hierarchical fibrous assembly of Au nanoparticles with atomic precision. *Nature Communications* **2018,** *9*.

77. Yoon, B.; Luedtke, W. D.; Barnett, R. N.; Gao, J. P.; Desireddy, A.; Conn, B. E.; Bigioni, T.; Landman, U., Hydrogen-bonded structure and mechanical chiral response of a silver nanoparticle superlattice. *Nature Materials* **2014,** *13*, 807-811.

78. Nonappa; Haataja, J. S.; Timonen, J. V. I.; Malola, S.; Engelhardt, P.; Houbenov, N.; Lahtinen, M.; Häkkinen, H.; Ikkala, O., Reversible Supracolloidal Self-Assembly of Cobalt Nanoparticles to Hollow Capsids and Their Superstructures. *Angewandte Chemie International Edition* **2017,** *56*, 6473-6477.

79. Molard, Y.; Dorson, F.; Circu, V.; Roisnel, T.; Artzner, F.; Cordier, S., Clustomesogens: Liquid Crystal Materials Containing Transition-Metal Clusters. *Angewandte Chemie-International Edition* **2010,** *49*, 3351-3355.

80. Molard, Y.; Ledneva, A.; Amela-Cortes, M.; Circu, V.; Naumov, N. G.; Meriadec, C.; Artzner, F.; Cordier, S., Ionically Self-Assembled Clustomesogen with Switchable Magnetic/Luminescence Properties Containing [Re6Se8(CN)(6)](n-) (n=3, 4) Anionic Clusters. *Chemistry of Materials* **2011,** *23*, 5122-5130.

81. Molard, Y.; Dorson, F.; Brylev, K. A.; Shestopalov, M. A.; Le Gal, Y.; Cordier, S.; Mironov, Y. V.; Kitamura, N.; Perrin, C., Red-NIR Luminescent Hybrid Poly(methyl methacrylate) Containing Covalently Linked Octahedral Rhenium Metallic Clusters. *Chemistry-a European Journal* **2010,** *16*, 5613-5619.

82. Amela-Cortes, M.; Garreau, A.; Cordier, S.; Faulques, E.; Duvail, J. L.; Molard, Y., Deep red luminescent hybrid copolymer materials with high transition metal cluster content. *Journal of Materials Chemistry C* **2014,** *2*, 1545-1552.

83. Voevodin, A.; Campos, L. M.; Roy, X., Multifunctional Vesicles from a Self-assembled Cluster-Containing Diblock Copolymer. *Journal of the American Chemical Society* **2018,** *140*, 5607-5611.

84. Baudron, S. A.; Batail, P.; Coulon, C.; Clerac, R.; Canadell, E.; Laukhin, V.; Melzi, R.; Wzietek, P.; Jerome, D.; Auban-Senzier, P.; Ravy, S., (EDT-TTF-CONH2)(6)[Re6Se8(CN)(6)], a metallic Kagome-type organic-inorganic hybrid compound: Electronic instability, molecular motion, and charge localization. *Journal of the American Chemical Society* **2005,** *127*, 11785-11797.

85. Renault, A.; Pouget, J. P.; Parkin, S. S. P.; Torrance, J. B.; Ouahab, L.; Batail, P., Evidence for a Spin-Peierls-Like Transition in the 1-D Organic Cation Radical Salt - Beta-(Tmtsf)2re6se5cl9. *Molecular Crystals and Liquid Crystals* **1988,** *161*, 329-334.

86. Penicaud, A.; Batail, P.; Coulon, C.; Canadell, E.; Perrin, C., Novel Redox Properties of the Paramagnetic Hexanuclear Niobium Cluster Halide Nb6cl18(3-) and the Preparation, Structures, and Conducting and Magnetic-Properties of Its One-Dimensional Mixed-Valence Tetramethyltetra(Selena and Thia)Fulvalenium Salts - [Tmtsf and Tmttf]5[Nb6cl18].(Ch2cl2)0.5. *Chemistry of Materials* **1990,** *2*, 123-132.

87. Karadas, F.; Avendano, C.; Hilfiger, M. G.; Prosvirin, A. V.; Dunbar, K. R., Use of a rhenium cyanide nanomagnet as a building block for new clusters and extended networks. *Dalton Transactions* **2010,** *39*, 4968-4977.

88. Roy, X.; Lee, C. H.; Crowther, A. C.; Schenck, C. L.; Besara, T.; Lalancette, R. A.; Siegrist, T.; Stephens, P. W.; Brus, L. E.; Kim, P.; Steigerwald, M. L.; Nuckolls, C., Nanoscale Atoms in Solid-State Chemistry. *Science* **2013,** *341*, 157-160.

89. Choi, B.; Yu, J.; Paley, D. W.; Trinh, M. T.; Paley, M. V.; Karch, J. M.; Crowther, A. C.; Lee, C. H.; Lalancette, R. A.; Zhu, X. Y.; Kim, P.; Steigerwald, M. L.; Nuckolls, C.; Roy, X., van der Waals Solids from Self-Assembled Nanoscale Building Blocks. *Nano Letters* **2016,** *16*, 1445-1449.

90. Lee, K. H.; Choi, B.; Plante, I. J. L.; Paley, M. V.; Zhong, X. J.; Crowther, A. C.; Owen, J. S.; Zhu, X. Y.; Roy, X., Two-Dimensional Fullerene Assembly from an Exfoliated van der Waals Template. *Angewandte Chemie-International Edition* **2018,** *57*, 6125-6129.

91. Voevodin, A.; Abella, L.; Castro, E.; Paley, D. W.; Campos, L. M.; Rodriguez-Fortea, A.; Poblet, J. M.; Echegoyen, L.; Roy, X., Dimerization of Endohedral Fullerene in a Superatomic Crystal. *Chemistry-a European Journal* **2017,** *23*, 13305-13308.

92. Shores, M. P.; Beauvais, L. G.; Long, J. R., Cluster-expanded Prussian blue analogues. *Journal of the American Chemical Society* **1999,** *121*, 775-779.

93. Beauvais, L. G.; Shores, M. P.; Long, J. R., Cyano-bridged Re(6)Q(8) (Q = S, Se) cluster-metal framework solids: A new class of porous materials. *Chemistry of Materials* **1998,** *10*, 3783-+.

94. Yan, B. B.; Zhou, H. J.; Lachgar, A., Octahedral niobium chloride clusters as building blocks of templated Prussian blue framework analogues. *Inorganic Chemistry* **2003,** *42*, 8818-8822.

95. Zhang, J. J.; Lachgar, A., Octahedral Metal Clusters as Building Blocks of Trimetallic.Superexpanded Prussian Blue Analogues. *Inorganic Chemistry* **2015,** *54*, 1082-1090.

96. Zhou, H. J.; Lachgar, A., Octahedral metal clusters [Nb6Cl12(CN)(6)](4-) as molecular building blocks: From supramolecular assemblies to coordination polymers. *European Journal of Inorganic Chemistry* **2007**, 1053-1066.

97. Tulsky, E. G.; Crawford, N. R. M.; Baudron, S. A.; Batail, P.; Long, J. R., Cluster-to-metal magnetic coupling: Synthesis and characterization of 25-electron [Re6-nOsnSe8(CN)(6)]((5-n)-) (n=1, 2) clusters and {Re6-nOSnSe8[CNCu(Me(6)tren)](6)}(9+) (n=0, 1, 2) assemblies. *Journal of the American Chemical Society* **2003,** *125*, 15543-15553.

98. O'Keeffe, M.; Yaghi, O. M., Deconstructing the Crystal Structures of Metal-Organic Frameworks and Related Materials into Their Underlying Nets. *Chemical Reviews* **2012,** *112*, 675-702.

99. Champsaur, A. M.; Yu, J.; Roy, X.; Paley, D. W.; Steigerwald, M. L.; Nuckolls, C.; Bejger, C. M., Two-Dimensional Nanosheets from Redox-Active Superatoms. *Acs Central Science* **2017,** *3*, 1050-1055.

100. Champsaur, A. M.; Meziere, C.; Allain, M.; Paley, D. W.; Steigerwald, M. L.; Nuckolls, C.; Batail, P., Weaving Nanoscale Cloth through Electrostatic Templating. *Journal of the American Chemical Society* **2017,** *139*, 11718-11721.

101. Bennett, M. V.; Beauvais, L. G.; Shores, M. P.; Long, J. R., Expanded Prussian blue analogues incorporating [Re(6)Se(8)(CN)(6)](3-/4-) clusters: Adjusting porosity via charge balance. *Journal of the American Chemical Society* **2001,** *123*, 8022-8032.

Chapter 2: *In Situ* Formation of N-Heterocyclic Carbene-Bound Single Molecule Junctions

2.1 Preface

Significant portions of this chapter are adapted from a publication on this research entitled "*In Situ* Formation of N-Heterocyclic Carbene-Bound Single Molecule Junctions" by Evan A. Doud, Michael S. Inkpen, Giacomo Lovat, Enrique Montes, Daniel W. Paley, Michael L. Steigerwald, Héctor Vázquez, Latha Venkataraman, and Xavier Roy published in *Jounral of the American Chemical Society*, **2018**, 140, 8944-8949. I authored this work along with Prof. Michael S. Inkpen where we sought to explore the conductivity of N-heterocyclic carbenes (NHCs) in single molecule junctions. I synthesized and characterized the compounds used in this study. Prof. Michael S. Inkpen performed the scanning tunneling microscope-based break-junction (STM-BJ) measurements with assistance from Dr. Giacomo Lovat, both members of the Venkataraman research group. Dr. Enrique Montes of the Vázquez group performed theoretical calculations on the NHC-bound single molecule junctions. Dr. Dan Paley assisted with single crystal X-ray diffraction refinement.

2.2 Introduction

From Chapter 1, we see that the superatomic core and the accompanying ligands determine both the individual and collective properties of superatomic crystals and materials. The ligand shell however, is highly influential in facilitating access to the properties contained within the core and how superatomic materials are assembled. For these reasons, expansion of the currently available

ligand space in superatom synthesis presents a number of challenges for chemists interested in superatomic materials. A potentially useful ligand class for superatoms are the NHCs. NHCs exhibit a number of attractive properties that could be useful in the development of superatomic materials, specifically their strong binding and highly functionalizable nature. This chapter investigates the conductance of a series of NHC containing molecules, demonstrating a potential avenue for their use as ligands superatomic materials.

A key design feature of nanoscale electronic devices is the chemical group that establishes the physical and electronic contact at the molecule–electrode interface. The nature of this interaction, i.e. covalent,[1-4] dative[5] or supramolecular,[6] can be exploited to tune the stability and function of the connected component. One family of linkers with emerging potential are the carbenes, neutral molecules comprising a divalent carbon atom with a six-electron valence shell.[7] Originally considered too reactive to isolate, the development of stable, persistent carbenes such as NHCs[8] has played a critical role in many areas of modern chemistry.[9] While NHCs have been used extensively as tuneable ligands for organometallic complexes, their ability to strongly bind nanoparticles or planar surfaces has only recently been recognized.[10] Johnson, Crudden and their respective co-workers have demonstrated that NHCs can form self-assembled monolayers (SAMs) on Au that exhibit remarkable thermal and chemical stability;[11-13] NHCs in solution are even capable of rapidly displacing preformed thiol–Au SAMs.[12] Given their strong σ-donor binding to metals and unique electronic structure,[9] this family of molecules offers exciting new prospects for surface functionalization, with potential applications in selective heterogeneous catalysis,[14-17] nanotechnology[10, 18-19] and sensing.[10-11, 13, 20] Essential to such developments is an improved understanding of both the electronic coupling between the carbene and the metal surface, and the

electron transport across the carbene–electrode interface. Despite theoretical interest,[21-22] these features have never been experimentally investigated.

In this work, we describe a novel strategy to probe the electronic properties of NHCs on Au electrodes. Using the scanning tunneling microscope-based break junction (STM-BJ) technique,[2, 23] we form NHC–electrode contacts via *in situ* electrochemical conversion of a metal NHC complex in the junction (Figure 2.1a). By measuring the electrical transport properties of a series of NHC-bound single-molecule junctions, we find that the conductance (*G*) of the junction depends on the metal atom in the precursor. Our hypothesis, supported by transport calculations based on density functional theory (DFT), is that as the complex is reduced at the STM tip the NHC remains coordinated to the metal atom. This atom subsequently binds to the electrode surface and establishes a conductive contact. By extending the backbone of the NHC-bound single-molecule junction, we observe a clear exponential decay of conductance, indicating a coherent non-resonant transport mechanism. These results establish our approach as a robust yet flexible strategy to form NHC-linked molecular junctions.

2.3 *In Situ* Formation of NHC-Bound Single Molecule Junctions

The synthetic details for all compounds are given in Section 2.8. Conductance measurements were carried out using the STM-BJ technique which has been described in detail elsewhere.[23] Conductance measurements for all complexes were performed using 10 μM solutions in PC. The Au tip was coated with an insulating layer to suppress background ionic current. The insulated tips were created by driving a mechanically cut gold tip through Apiezon wax.[24] 1D

conductance histograms were constructed using logarithmic bins (100 per decade) without any data selection.

Our first objective was to measure the transport properties of a linear aromatic molecule utilizing an NHC as the contacting group. To achieve this goal, we exploited a new *in situ* electrochemical reduction approach to form the single-molecule junction using the STM-BJ technique (Figure 2.1a). For this method, the molecule is terminated by an aurophilic thiomethyl group (SMe) on one end, and a benzannulated NHC on the other end. The NHC is capped with one of a series of metal chloride complexes; the resulting air-stable metal NHC precursors are labelled **NHC1–MCl** (**M** = Au, Ag, Cu). A single-molecule junction is established when the SMe binds to the electrode surface via an Au–S bond, and the metal NHC complex is reduced at the STM tip. We developed this innovative strategy because we were unable to characterize the single-molecule transport characteristics of NHCs bound in SAMs prepared using traditional methods, shown in Figure 2.1b. STM-BJ measurements of monolayers assembled on Au surfaces from solutions of free NHCs, or from the vapor phase using NHC-CO_2 adduct precursors,[12, 25] did not yield reproducible conductance results.

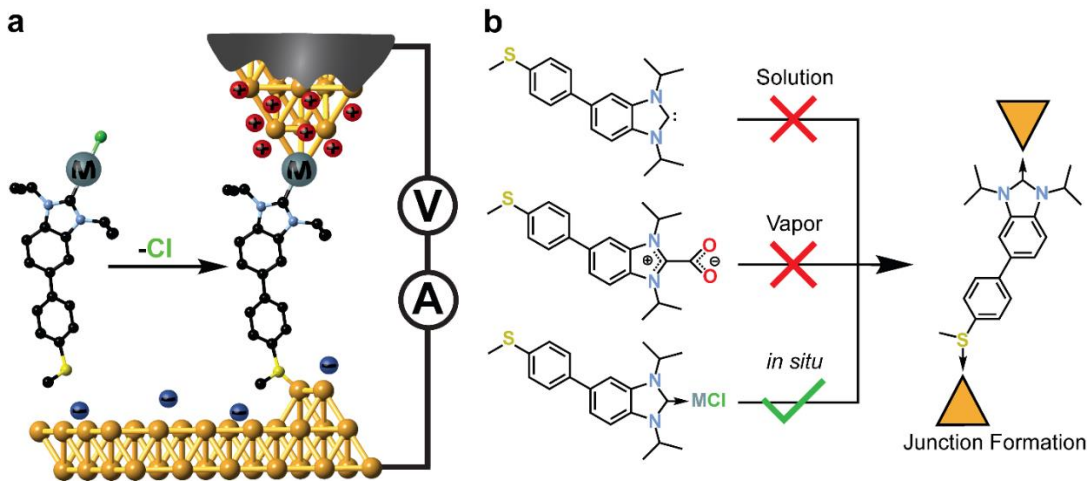

Figure 2.1: a. Schematic of an NHC-bound single-molecule junction created via *in situ* electrochemical conversion of a metal NHC complex. **b.** Synthetic strategies employed to prepare NHC-bound SAMs for subsequent STM-BJ measurements in air (solution, vapor). These proved unsuccessful, in contrast to the use of metal NHC complexes to form junctions directly from solution (*in situ*).

Figure 2.2a presents the molecular structure of the precursors **NHC1–CuCl**, **NHC1–AgCl** and **NHC1–AuCl**, as determined by single crystal x-ray diffraction (SCXRD). Details of the STM-BJ measurements in an ionic environment have been described previously.[26] Briefly, the measurements are performed using an insulated Au STM tip, with an exposed area of ~1 μm^2, and an Au substrate with an area larger than 1 cm^2. When a bias is applied, a dense double-layer of charge builds up around the small area of the coated tip while a sparse double-layer is formed on the large-area, uncoated substrate. Previous studies have demonstrated that under these conditions, redox-active compounds such as ferrocene[27] or molecular clusters[28] can be oxidized or reduced in the junction under positive or negative tip biases, respectively.

2.4 Conductance Dependence on M^I Identity

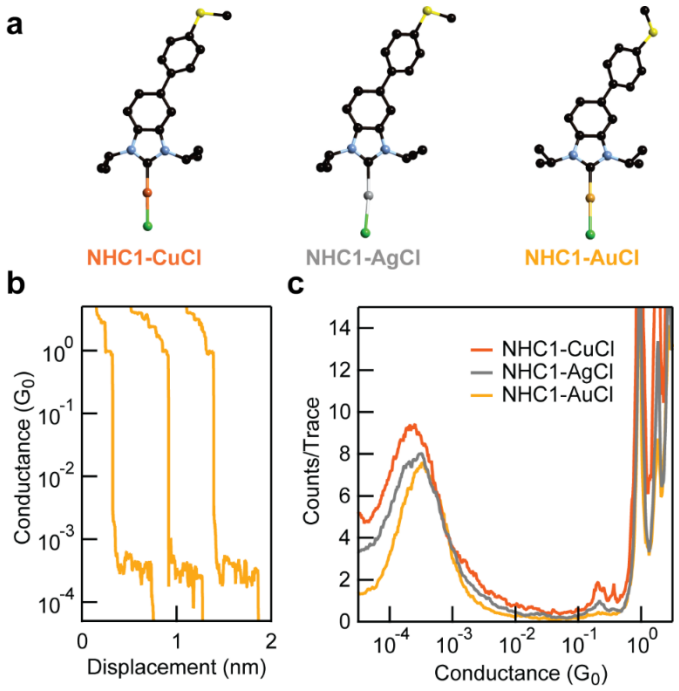

Figure 2.2: a. Molecular structure of **NHC1–MCl**, as determined by SCXRD. Colour code: black, C; blue, N; yellow, S; green, Cl; orange, Cu; gray, Ag; gold, Au. Hydrogens are omitted. **b.** Sample conductance versus displacement traces of **NHC1–AuCl**, offset laterally for clarity. The plateau at ~3 $\times 10^{-4}$ G_0 results from the single-molecule junction. **c.** Logarithmically-binned 1D conductance histograms (100 bins/decade) of **NHC1–MCl** junctions, each composed of at least 2,000 traces without data selection. All measurements are in PC at a tip bias of –720 mV.

When we use this approach with **NHC1–MCl** in propylene carbonate (PC), we can form electrically conducting NHC-bound single-molecule junctions by applying a negative (i.e. reducing) tip bias. Figure 2.2b shows sample conductance versus displacement traces for **NHC1–AuCl**, measured under a reducing tip bias of –720 mV. Clear conductance plateaus are visible at ~3 × 10^{-4} G_0 ($G_0 = 2e^2/h$ is the quantum of conductance), which we attribute to the conductance of the NHC-bound single-molecule junction. These measurements are repeated thousands of times and the traces are compiled into logarithmically binned one-dimensional (1D) histograms, without

data selection. Figure 2.2c presents the 1D histograms of all three **NHC1–MCl** complexes measured at –720 mV tip bias. Each histogram shows peaks close to integer multiples of G_0, indicating the formation of Au point contacts, as well as a peak between 10^{-4} and 10^{-3} G_0, corresponding to the most probable conductance of the NHC-bound single-molecule junction. Remarkably, we find that the position of the conductance peak depends on the metal in the precursor and decreases across the series as Au > Ag > Cu.

We emphasize that the NHC-bound junctions form reproducibly under negative (reductive) tip bias but not under positive (oxidative) tip bias (Figure 2.12). This strongly suggests that through the application of a negative tip bias, the metal complex in the junction is reduced and binds to the electrode, that is **NHC1**–$M^{I}Cl$ $\rightarrow$ **NHC1**–M^{0}–electrode. In addition to the bias polarity dependence, this hypothesis is supported by several observations and control experiments. (1) The metal-dependant conductance values indicate that the NHC group remains coordinated to the precursor metal atom even as it is reduced and binds to the electrode (Figure 2.2c). (2) The *in situ* formation of molecule-electrode bonds has previously been reported using benzyltrialkylstannane and benzyl–Au(PPh_3) contact group precursors[3]. (3) We synthesized two complexes as controls and measured their single-molecule conductance (Figures 2.13a and 2.13b). The first complex, **[NHC1–AuPPh$_3$][BF$_4$]**, is analogous to **NHC1–AuCl** but the Cl^- ligand is replaced with a weakly coordinating BF_4^- anion, and PPh_3, which is known to dissociate from Au complexes upon junction formation[3]. The conductance of **[NHC1–AuPPh$_3$][BF$_4$]** is close to that of **NHC1–AuCl**, strongly suggesting that the molecular junction does not form by binding through the Cl atom to the Au electrode (i.e. **NHC1**–Au–Cl–electrode). The second complex, bis(diethyl(4-(methylthio)phenyl)phosphine)AuCl (**((4-MeSPh)Et$_2$P)$_2$AuCl**), is used to confirm that junctions

formed via *in situ* reduction of gold chloride complexes are analogous to those formed by directly binding the free linker to the electrode. In this experiment, we replace the highly reactive NHC with a diethyl(aryl)phosphine group, which can be measured in the form of a metal chloride complex or as the free phosphine using the STM-BJ technique. In agreement with our premise, the conductance of the **((4-MeSPh)Et$_2$P)$_2$AuCl** complex agrees well with that of the free phosphine. Note however that the fate of the Cl^- ion cannot be determined through this experiment.

2.5 Length Dependence of Conductance

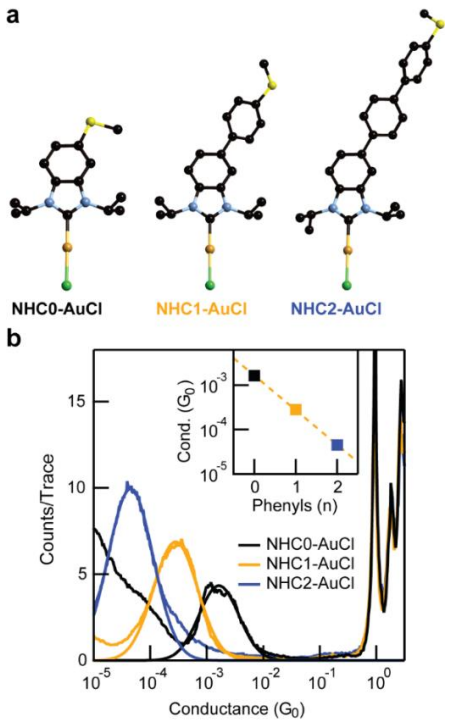

Figure 2.3: a. Molecular structure of **NHC*n*–AuCl** (*n* = 0, 1, 2), as determined by SCXRD. Note that the structure for **NHC1–AuCl** is repeated from Figure 2.2a for completeness. **b.** Logarithmically-binned 1D conductance histograms (100 bins/decade) of **NHC*n*–AuCl**, each composed of at least 2,000 traces obtained without data selection. All measurements are performed in PC at a tip bias of –360 mV. Inset: semi-logarithmic plot of the conductance histogram peak value as a function of the number of phenylene units in the backbone of **NHC*n*–AuCl**.

To gain a deeper understanding of electron transport across the NHC–electrode interface, we investigate how the conductance of NHC-bound single-molecule junctions changes with increasing molecular length. For this, we synthesized a new series of asymmetric oligophenylene derivatives. As in the previous design, each molecule is terminated by a SMe group on one end and a benzannulated NHC–AuCl group on the other. Figure 2.3a shows the molecular structure of **NHC0–AuCl**, **NHC1–AuCl** and **NHC2–AuCl**, as determined by SCXRD. As with the **NHC1–MCl** series, molecular junctions only form under reducing conditions in PC. Figure 2.3b presents the 1D conductance histograms of all three molecules (2D conductance-displacement histograms are presented in Figure 2.14). Each histogram shows a clear peak below G_0, and the conductance decreases with increasing molecular length. The inset of Figure 2.3b shows a semi-logarithmic plot of the conductance values, obtained from a Gaussian fit to the histogram as a function of the number of phenylene units (n) in the molecular backbone. An exponential fit to the data with $G \sim e^{-\beta n}$ gives a conductance decay β = 1.8/phenylene. This β value is in good agreement with that reported for oligophenylene molecular junctions with other linkers.[2, 29]

2.6 Computational Studies

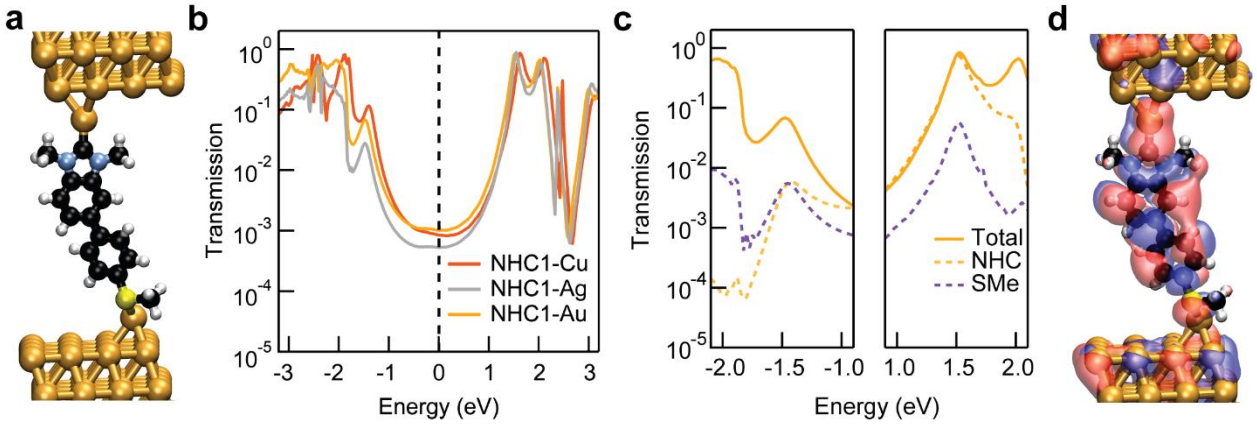

Figure 2.4: a. Modeled structure of **NHC1-Au** junction. **b.** Transmission function of **NHC1–M** junctions. **c.** Projection of the electronic coupling matrices at the NHC and SMe contacts for the **NHC1–Au** junction onto the HOMO (left) and LUMO (right). **d.** Real-space representation of the most conducting transmission eigenchannel of **NHC1–Au** junction at the LUMO energy.

The electronic and transport properties of molecular junctions were calculated using first-principles methods based on DFT-NEGF.[30-31] We modelled the junction by attaching the molecular backbone on the carbene side to an Au adatom for **NHC*n*–AuCl**, an Ag adatom for **NHC1–AgCl** and a Cu adatom for **NHC1–CuCl** (without including the Cl atom). To simplify geometry optimization, the isopropyl groups were replaced with methyl groups, resulting in negligible changes in conductance. The SMe side was attached to an Au adatom for all junctions. The supramolecular structure was placed between two electrodes that consisted of a 4×4 fcc Au(111) surface. We optimized the junction structure by relaxing the coordinates of the molecular backbone and the Au atoms to a force threshold smaller than 0.02 eV/Å, also optimizing the inter-electrode vertical separation. In the calculations, the exchange-correlation was described using the GGA approximation in the PBE implementation.[32] We used a double-zeta polarized local-orbital basis for molecular atoms and a single-zeta basis for Au atoms. We performed subsequent transport

calculations at optimized geometries by adding additional Au(111) layers. We used Monkhorst-Pack grids of 5×5×1 and 15×15×1 for calculating the electronic structure and transmission spectra, respectively. Transmission eigenchannels were computed at the center of the Brillouin zone.[33]To support these measurements, we perform DFT-based atomistic calculations of **NHC1–M** and **NHC*n*–Au** junctions (see Experimental). These junctions are modelled with both NHC and SMe groups bound to undercoordinated metal atoms on the electrode surface (Figure 2.4a and Figure 2.15).[25, 34] The atomic simulations underscore the strength of the NHC contact, regardless of the undercoordinated metal **M**: the computed binding energies of the NHC to the undercoordinated metal **M** are 1.6 to 2.0 eV (Table S2), comparable to reported binding energies of NHCs to Au(111) surfaces (1.5-1.75 eV),[12, 25] and significantly higher than those calculated for thiolate-based Au–S bonds.[35-36] For the **NHC*n*–Au** series, the calculated binding energy of the molecule in the junction is ~2.7 eV, and essentially independent of the number of phenylene units *n* (Table S2). The NHC contact is responsible for most of the binding (~2.0 eV), while the contribution of the Au–SMe bond is smaller (~0.7 eV), in agreement with previous calculations.[37]

DFT-based transport calculations are subsequently applied to establish the role the NHC contact plays in the transport properties of **NHC1–M** and **NHC*n*–Au** junctions. Figure 2.4b presents the calculated transmissions as a function of energy relative to Fermi level (E_F) for all three types of **NHC1–M** junction. For each junction type, the high-transmission peak closest to E_F derives from the lowest unoccupied molecular orbital (LUMO). A peak with lower transmission originating from a S-localized metal-molecule state is observed at ca. –1.5 V, which has previously been attributed to the Au–S gateway state.[38] The precursor metal atom **M** introduces only minor changes in the transmission function but it modulates the low-bias conductance. In agreement with

the measurements, we find a slightly lower conductance for Ag and Cu precursors than for Au. The position of the occupied resonance and resulting zero-bias conductance follow the trend in the position of the d-states in Au, Ag and Cu.[39]

Analysis of the transmission functions of the **NHC*n*–Au** junctions reveal that the LUMO and other empty molecular states derive mainly from the NHC unit while the SMe group contributes to the occupied state around –1.5 eV. The SMe contribution increases as the molecular backbone is lengthened (Figures 2.16 and 2.17). The computed conductance for the **NHC*n*–Au** junctions decreases exponentially as *n* increases. An exponential fit to the calculated values yields a decay constant β ~1.6/phenylene (Figure 2.18), slightly lower than the experimental β. This difference is in line with the general trends of DFT-based calculations.[27]

The projection of the electronic coupling matrices of the NHC/SMe contacts (top/bottom contacts in Figure 2.4a) for the **NHC1–Au** junction onto the HOMO and LUMO (Figure 2.4c) reveals the role the NHC plays in the transport characteristics (see Supporting Information for details). The low transmission observed when the NHC or SMe contacts are projected onto the HOMO (left panel in Figure 2.4c) illustrates the poor electronic coupling of this state to the electrodes. By contrast, when the coupling matrix of the NHC–Au contact is projected onto the (NHC-derived) LUMO, the total transmission is almost recovered (right panel in Figure 2.4c). This demonstrates the excellent conducting properties of the NHC linker, and quantifies the electronic coupling of the NHC-derived state to the electrode. In agreement with this finding, we see that current is carried by a single transmission channel, shown in Figure 2.4d at the LUMO energy which resembles the LUMO of the isolated molecule (see Figure 2.19).

2.7 Conclusion and Outlook

By designing a series of metal NHC complexes that can be electrochemically reduced *in situ* at the STM tip to form the NHC–electrode contact, we have demonstrated the first single-molecule study of electron transfer across an NHC–metal interface. Experimental and theoretical data indicate that the NHC conducts primarily through the LUMO. Given that many types of carbenes can form stable metal complexes, our *in situ* electrochemical approach opens the door to exploring the electronic properties of a wide range of carbene–electrode interfaces beyond NHCs. Remarkably, our method also introduces a unique strategy to manipulate the conductance of a single-molecule junction through *in situ* formation of heterometallic electrode contacts. Our results thus chart a clear path to define the final electrode structure down to the atomic level, through a combination of careful molecular design and synthetic electrochemistry. Further, these aspects of NHCs establish them as a class of molecules with significant relevance to materials scientists.

2.8 Synthetic Details

2-Iodopropane and sodium metal were purchased from Acros Organics. Ammonium chloride was purchased from Alfa Aesar. DMSO-d_6, benzene-d_6, and $CDCl_3$ were purchased from Cambridge Isotope. Dichloromethane (DCM), diethyl ether, dioxane, ethyl acetate, hexanes, isopropanol, sodium chloride, and tetrahydrofuran (THF) were purchased from Fisher Scientific. 5-Chloro-2-nitroaniline was purchased from Matrix Scientific. Silica gel was purchased from Silicycle. All other reagents and solvents were purchased from Sigma-Aldrich. Dry and deoxygenated solvents were prepared by elution through a dual-column solvent system (MBraun SPS). All reactions and sample preparations were carried out under inert atmosphere using

standard Schlenk techniques or in a nitrogen-filled glovebox unless otherwise noted. ^{1}H, ^{13}C, and ^{31}P NMR spectra were recorded on Bruker DRX400 and DMX500 spectrometers. ^{1}H and ^{13}C spectra were referenced using DMSO-d_6, C_6D_6, or $CDCl_3$, with the residual solvent peak as the internal standard, and ^{31}P spectra were referenced using H_3PO_4. Chemical shifts were reported in ppm, with ^{1}H multiplicities reported as: s (singlet), d (doublet), t (triplet), q (quartet), p (pentet), m (multiplet), and br (broad) or as indicated. Coupling constants, *J*, are reported in Hz and integration is provided.

An overall synthetic scheme is given in Figure 2.5.

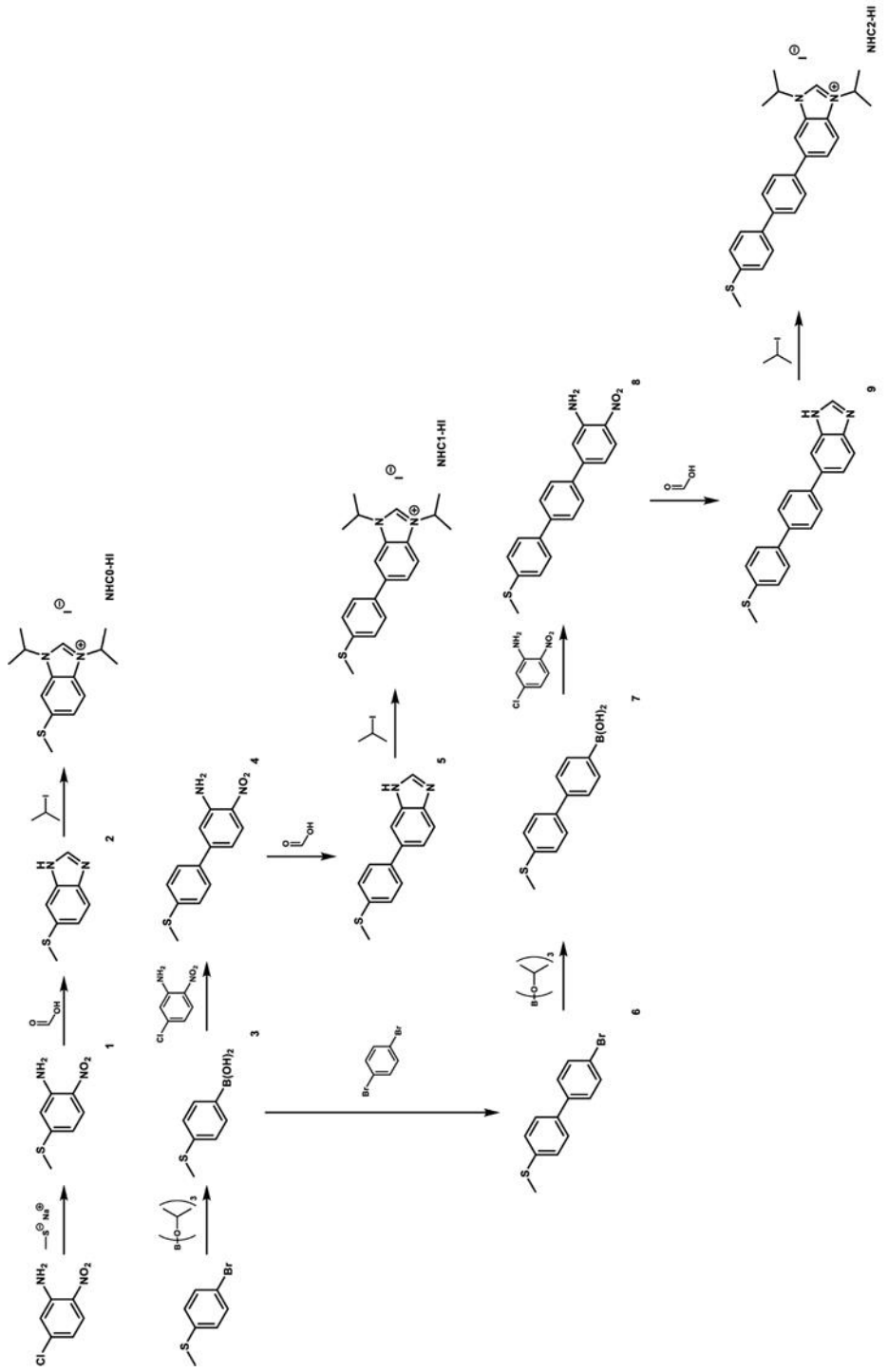

Figure 2.5: Synthetic scheme for the synthesis of NHC precursors. Full synthetic details are given below.

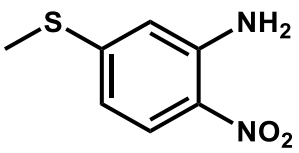

1

1. An oven-dried 250 mL round bottom flask equipped with a Teflon coated stir bar was charged with sodium methanethiolate (3.04 g, 43.4 mmol) (prepared according to a literature procedure[40]). Dry and deoxygenated N,N-dimethylformamide (DMF) (50 mL) was added and the suspension was vigorously stirred for 30 minutes. A solution of 5-chloro-2-nitroaniline (5.00 g, 28.9 mmol) in 50 mL of dry and deoxygenated DMF was added via oven-dried cannula to the sodium methanethiolate suspension. The reaction mixture turned a light red color and was then heated to 65°C for 20 hours or until TLC indicated complete consumption of the 5-chloro-2-nitroaniline. After 20 h, the deep red reaction mixture was cooled to room temperature and opened to air; 100 mL of water was added, and the reaction mixture was stirred for 1 h. The reaction mixture was then transferred to a separatory funnel and extracted several times with ethyl acetate (5 x 100 mL, a brine solution may be added to facilitate separation of the layers). The combined organic extracts were then washed with water (3 x 250 mL) and brine (2 x 100 mL). The organic extracts were then dried over $MgSO_4$, and the solvent was removed via rotary evaporation. The solid was purified using silica gel flash column chromatography, eluting with 50% ethyl acetate in hexanes to afford **1** as a red-orange solid. (Yield: 4.6 g, 87%)

^{1}H NMR (500 MHz, DMSO-d_6): δ (ppm) 7.86 (d, J = 9.1 Hz, 1H), 7.46 (s, 2H), 6.79 (d, J = 2.1 Hz, 1H), 6.48 (dd, J = 9.1, 2.1 Hz, 1H), 2.48 (s, 3H). ^{13}C{^{1}H} NMR (126 MHz, DMSO-d_6): δ (ppm) 148.80, 146.37, 127.53, 125.60, 113.26, 112.11, 13.83.

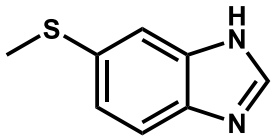

2

2. Synthesized following a modified literature procedure[12]. A 250 mL 2-neck round bottom flask equipped with a Teflon coated stir bar, reflux condenser with gas inlet adapter, and rubber septum, was charged with **1** (2.00 g, 10.8 mmol), Fe powder (6.06 g, 108.5 mmol), and ammonium chloride (5.81 g, 108.5 mmol). The flask was evacuated and refilled with N_2. In a separate 100 mL round bottom flask equipped with a stir bar and rubber septum, 35 mL of formic acid and 50 mL of isopropanol was sparged with N_2 for 15 min. After sparging, the formic acid and isopropanol solution was added to the flask containing 5-(methylthio)-2-nitroaniline, Fe powder, and ammonium chloride via cannula. The reaction mixture was heated to reflux at 80°C and stirred under N_2 for 3 h. The reaction mixture underwent several color changes finally ending in a light yellow-green with a large amount of gray precipitate. After 3 h, the reaction mixture was cooled to room temperature, opened to air and filtered through a pad of Celite over a medium porosity frit. The filter cake was washed with isopropanol (3 x 20 mL). The combined filtrate was evaporated to dryness via rotary evaporation, leaving a sticky solid. Saturated aqueous $NaHCO_3$ solution was slowly added to the solid residue until a neutral pH was obtained. The reaction mixture was then transferred to a separatory funnel and extracted with chloroform (3 x 50 mL). The combined extracts were dried over $MgSO_4$, filtered, and the solvent was removed via rotary evaporation to yield **2** as a sticky, brown, foamy solid. (Yield: 1.6 g, 90%)

^{1}H NMR (500 MHz, $CDCl_3$): δ (ppm) 8.10 (s, 1H), 7.59 (m, 2H), 7.28 (dd, *J* = 8.5, 1.7 Hz, 1H), 2.52 (s, 3H). $^{13}C\{^{1}H\}$ NMR (126 MHz, $CDCl_3$): δ (ppm) 141.35, 138.51, 136.88, 132.54, 123.72, 116.18, 114.35, 17.59.

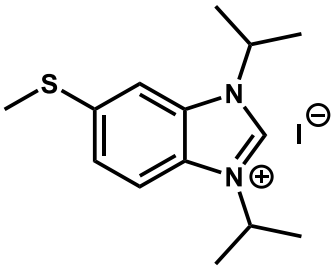

NHC0-HI

NHC0–HI. Synthesized following a modified literature procedure.[12] A 2-neck 100 mL round bottom flask equipped with a Teflon coated stir bar, reflux condenser with a gas inlet adapter, and rubber septum was charged with **2** (0.60 g, 3.6 mmol), K_2CO_3 (1.00 g, 7.2 mmol) and 25 mL of acetonitrile. The reaction mixture was sparged with N_2 while stirring vigorously for 30 min. 2-Iodopropane (2.5 mL, 25 mmol) was then added using a N_2 flushed syringe. The reaction mixture was refluxed at 90°C and stirred for 48 h. The reaction mixture was then cooled to room temperature and all volatiles were removed *in vacuo*. The flask was opened to air, the solid residue was sonicated in 50 mL of DCM for 10 min, and filtered through a pad of Celite over a medium porosity frit. The filter cake was washed with DCM (2 x 20 mL). The DCM filtrate was concentrated by rotary evaporation and ethyl acetate was added to induce precipitation. The suspension was then sonicated for 1 h, the solid was collected by filtration and washed with ethyl acetate and diethyl ether. The solid was then dried *in vacuo* to yield **NHC0–HI** as an off-white powder. (Yield: 893 mg, 65%)

^{1}H NMR (500 MHz, $CDCl_3$): δ (ppm) 10.82 (s, 1H), 7.70 (d, *J* = 8.8 Hz, 1H), 7.64–7.41 (m, 2H), 5.18 (overlapping septets, 2H), 2.61 (s, 3H), 1.85 (overlapping d, 12H). ^{13}C{^{1}H} NMR (126 MHz, $CDCl_3$): δ (ppm) 139.81, 139.22, 131.73, 128.45, 126.24, 114.08, 110.19, 52.66, 52.34, 22.35, 22.32, 16.50.

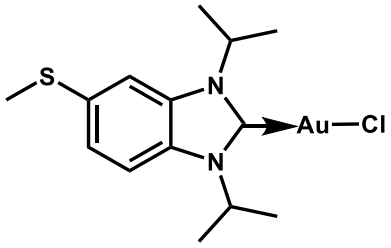

NHC0-AuCl

NHC0–AuCl. Prepared following the general procedure outlined below for the synthesis of **NHC1–AuCl**, using **NHC0–HI** (37 mg, 100 μmol), KO^{t}Bu (12.2 mg, 110 μmol), and $(SMe)_2AuCl$ (32.4 mg, 105 μmol). **NHC0–AuCl** was obtained as a faint yellow powder. (Yield: 46 mg, 95%)

X-ray diffraction quality crystals were grown by slow evaporation of a DCM solution of **NHC0–AuCl**.

^{1}H NMR (500 MHz, $CDCl_3$): δ (ppm) 7.55 (d, *J* = 8.7 Hz, 1H), 7.51 (d, *J* = 1.6 Hz, 1H), 7.30 (dd, *J* = 8.7, 1.7 Hz, 1H), 5.47 (overlapping septets, 7.0 Hz, 2H), 2.56 (s, 6H), 1.72 (overlapping doublets, 12H). ^{13}C{^{1}H} NMR (126 MHz, $CDCl_3$): δ (ppm) 176.37, 134.87, 133.14, 130.53, 123.84, 113.27, 111.53, 54.54, 54.23, 21.73, 21.69, 17.30.

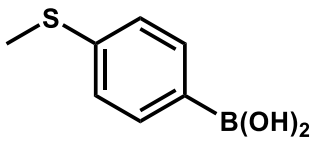

3

3. An oven-dried 3-neck 500 mL round bottom flask equipped with a Teflon coated stir bar, 60 mL addition funnel with a rubber septum, gas inlet adapter, and rubber septum was charged with 50 mL of THF. The flask was cooled to -78 °C in a dry ice/acetone bath, and *n*-BuLi (1.6 M in hexanes, 15 mL, 24.0 mmol) was added to the cooled THF and allowed to stir for 10 minutes. A solution of 4-bromothioanisole (3.00 g, 14.7 mmol) in 50 mL of THF was added to the addition funnel via a N_2 flushed syringe. The 4-bromothioanisole solution was then added dropwise to the *n*-BuLi solution and the reaction was stirred for 1 h, forming a white slurry. A solution of triisopropyl borate (3.75 g, 20.0 mmol) in 20 mL of THF was then added to the addition funnel using a N_2 flushed syringe. The triisopropyl borate solution was added dropwise; the reaction was warmed to room temperature after the addition finished and was stirred for an additional 3 h. The reaction was then opened to air, 100 mL of water was added dropwise through the addition funnel, and allowed to stir for an additional 30 min. 1M aqueous HCl was slowly added until a pH of 1 was obtained, and the mixture was stirred for 30 min. THF was then removed *in vacuo*. The resulting solid was then filtered and washed with water (3 x 50 mL), hexanes (3 X 50 mL), and dried overnight *in vacuo* to yield **3** as a white fluffy powder. (Yield: 2.05 g, 83%)

^{1}H NMR (500 MHz, DMSO-d_6): δ (ppm) 7.98 (s, 2H), 7.72 (d, J = 8.2 Hz, 2H), 7.21 (d, J = 8.2 Hz, 2H), 2.48 (s, 3H). ^{13}C{^{1}H} NMR (126 MHz, DMSO-d_6): δ (ppm) 140.99, 135.09, 130.28, 124.89, 14.60.

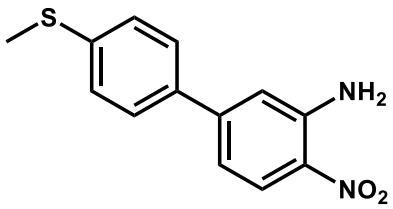

4

4. Synthesized following a modified literature procedure.[41] A 100 mL 2-neck round bottom flask equipped with a Teflon coated stir bar, reflux condenser with a gas inlet adapter, and rubber septum was charged with **3** (1.00 g, 5.9 mmol), 5-chloro-2-nitroaniline (0.80 g, 4.6 mmol) and tri(*o*-tolyl)phosphine (0.44 g, 1.4 mmol). The flask was evacuated and refilled with N_2. In a separate flask, a mixture of 30 mL of dioxane and 10 mL of 2.0 M aqueous K_2CO_3 was sparged with N_2 for 30 min. The mixture was transferred to the 2-neck flask using a cannula and $Pd(PPh_3)_4$ (0.35 g, 0.3 mmol) was added to the flask. The reaction was stirred under reflux for 18 h. The flask was then opened to air and dioxane was removed via rotary evaporation. Ethyl acetate (100 mL) was added to the flask, and the mixture was washed with water (3 x 100 mL) and with brine (2 x 100 mL). The organic phase was dried over $MgSO_4$ and purified by silica gel flash column chromatography, eluting with a 20-50% ethyl acetate in hexanes gradient. **4** was obtained as a yellow crystalline solid. (Yield: 0.99 g, 82%)

^{1}H NMR (500 MHz, DMSO-d_6): δ (ppm) 8.03 (d, J = 9.0 Hz, 1H), 7.61 (d, J = 8.5 Hz, 2H), 7.46 (br, 2H), 7.38 (d, J = 8.5 Hz, 2H), 7.28 (d, J = 2.0 Hz, 1H), 6.93 (dd, J = 9.0, 2.0 Hz, 1H), 2.52 (s, 3H). ^{13}C{^{1}H} NMR (126 MHz, DMSO-d_6): δ (ppm) 146.94, 146.72, 140.18, 134.85, 129.85, 127.65, 126.74, 126.59, 116.24, 114.61, 14.85.

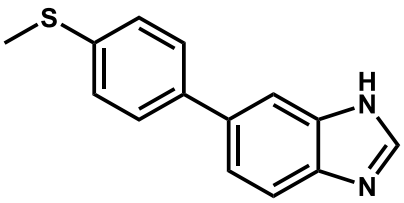

5

5. Synthesized following the same procedure as **2**, starting from **4** (500 mg, 1.9 mmol) with the following modifications. Benzene (100 μL) was added to the reaction to aid solubilizing the amine. After stirring under reflux for 3 h, the mixture was hot filtered. **5** was obtained as a light yellow powder. (Yield: 408 mg, 88%)

^{1}H NMR (500 MHz, DMSO-d_6): δ (ppm) 12.48 (br, 1H), 8.24 (s, 1H), 7.81 (s, 1H), 7.65 (d, J = 8.6 Hz, 3H), 7.48 (dd, J = 8.4, 1.8 Hz, 1H), 7.35 (d, J = 8.4 Hz, 2H), 2.51 (s, 3H). ^{13}C{^{1}H} NMR (126 MHz, DMSO-d_6): δ (ppm) 143.21, 138.22, 136.98, 134.23, 130.25, 127.81, 127.20, 126.98, 121.37, 117.15, 113.92, 15.30.

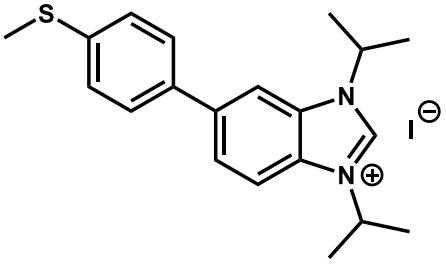

NHC1-HI

NHC1–HI. This compound was synthesized following the same procedure as **NHC0-HI**, starting from **5** (300 mg, 1.2 mmol) with the following modifications. The reaction mixture was heated to reflux and stirred until consumption of the starting benzimidazole material, as determined by NMR (typically 48-96 h). An additional 4 equivalents of 2-iodopropane was added after 48 h if the

reaction was not completed. The product was precipitated using a 50:50 mixture of ethyl acetate and diethyl ether. **NHC1–HI** was obtained as an off-white powder. (Yield: 215 mg, 38%)

^{1}H NMR (500 MHz, $CDCl_3$): δ (ppm) 10.91 (s, 1H), 7.89$CDCl_3$, δ ppm): δ –7.79 (m, 3H), 7.54 (d, *J* = 8.4 Hz, 2H), 7.37 (d, *J* = 8.4 Hz, 2H), 5.31–5.18 (overlapping septets, 2H), 2.53 (s, 3H), 1.89 (overlapping doublets, 12H). ^{13}C{^{1}H} NMR (126 MHz, $CDCl_3$): δ (ppm) 140.63, 139.86, 139.81, 135.62, 131.60, 129.91, 127.91, 126.89, 126.62, 114.31, 111.43, 52.70, 52.42, 22.39, 22.34, 15.59.

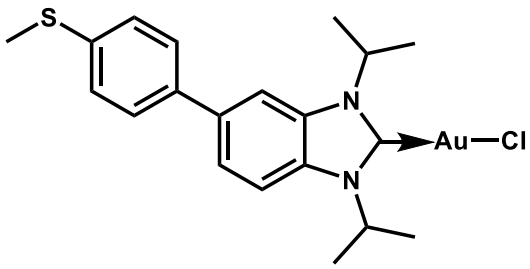

NHC1-AuCl

NHC1–AuCl. Synthesized following a modified literature procedure.[42] **NHC1–HI** (45 mg, 100 μmol) was suspended in 8 mL of THF. KO^{t}Bu (12 mg, 110 μmol) was added to the suspension and the reaction was stirred for 1 h. The mixture was then filtered through Celite and $(SMe)_2AuCl$ (31 mg, 105 μmol) was added to the filtrate. The reaction was stirred for 3 h, protected from light. Activated carbon (~100 mg) was added to the reaction, which was stirred for 1 h and then filtered through Celite. The solvent was then removed *in vacuo*. The solid residue was redissolved in DCM, filtered, and the solvent removed *in vacuo* to yield the pure complex **NHC1–AuCl** as a light yellow powder. (Yield: 48 mg, 86%)

X-ray diffraction quality single crystals were obtained by slow diffusion of hexanes into a DCM solution of the complex.

^{1}H NMR (500 MHz, $CDCl_3$): δ (ppm) 7.76 (d, *J* = 1.5 Hz, 1H), 7.71 (d, *J* = 8.6 Hz, 1H), 7.58 (dd, *J* = 8.6, 1.6 Hz, 1H), 7.54 (d, *J* = 8.4 Hz, 2H), 7.40 (d, *J* = 8.4 Hz, 2H), 5.56 (overlapping septets, 2H), 2.57 (s, 3H), 1.79 (overlapping doublets, 12H). ^{13}C{^{1}H} NMR (126 MHz, $CDCl_3$): δ (ppm) 176.74, 138.74, 137.34, 136.95, 133.15, 131.60, 127.81, 127.00, 123.35, 113.28, 111.07, 54.57, 54.31, 21.80, 21.72, 15.77.

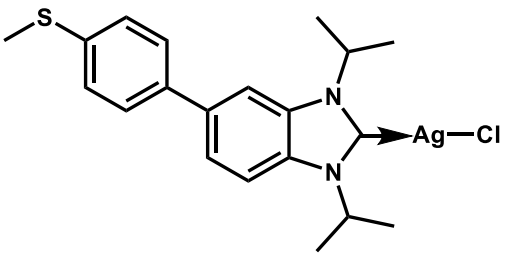

NHC1-AgCl

NHC1–AgCl. Prepared following the general procedure outlined above for the synthesis of **NHC1–AuCl**, using **NHC1–HI** (45 mg, 100 μmol) and (SMe_2)AgCl (20 mg, 105 μmol, see synthesis below). **NHC1–AgCl** was obtained as a light off-white powder. (Yield: 40 mg, 85%)

X-ray diffraction quality crystals were grown by slow evaporation of a DCM solution of **NHC1–AgCl**.

^{1}H NMR (400 MHz, $CDCl_3$): δ (ppm) 7.71 (d, *J* = 1.5 Hz, 1H), 7.66 (d, *J* = 8.7 Hz, 1H), 7.57 (dd, *J* = 6.6, 1.7 Hz, 1H), 7.52 (d, *J* = 8.4 Hz, 2H), 7.37 (d, *J* = 8.5 Hz, 2H), 5.15–5.03 (overlapping septets, 2H), 2.54 (s, 3H), 1.75 (overlapping doublets, 12H). ^{13}C{^{1}H} NMR (101 MHz, $CDCl_3$): δ (ppm) 176.49, 138.66, 137.23, 137.04, 133.90, 132.22, 127.84, 127.81, 127.01, 123.28, 112.93, 110.74, 54.44, 53.98, 22.62, 22.49, 15.79.

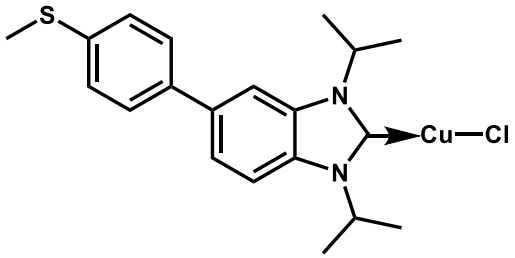

NHC1-CuCl

NHC1–CuCl. Prepared following the general procedure outlined above for the synthesis of **NHC1–AuCl**, using **NHC1–HI** (45 mg, 100 μmol) and (SMe_2)CuCl (16 mg, 105 μmol, see synthesis below). **NHC1–CuCl** was obtained as a white powder. (Yield: 36 mg, 85%)

X-ray diffraction quality crystals were grown by slow diffusion of hexanes into a THF solution of **NHC1–CuCl**.

^{1}H NMR (400 MHz, $CDCl_3$): δ (ppm) 7.66 (d, *J* = 1.4 Hz, 1H), 7.60 (d, *J* = 8.6 Hz, 1H), 7.56 (d, *J* = 1.5 Hz, 1H), 7.52 (d, *J* = 8.5 Hz, 2H), 7.37 (d, *J* = 8.4 Hz, 2H), 5.08 (overlapping septets, 2H), 2.54 (s, 3H), 1.79 (overlapping doublets, 12H). ^{13}C{^{1}H} NMR (101 MHz, $CDCl_3$): δ (ppm) 180.95, 138.52, 137.18, 137.11, 133.82, 132.24, 127.81, 127.03, 123.12, 112.33, 110.11, 52.95, 52.45, 23.17, 23.02, 15.81.

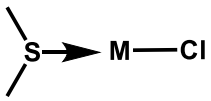

(SMe_2)MCl. Both (SMe_2)CuCl and (SMe_2)AgCl were synthesized using the same procedure. CuCl (99 mg, 1.0 mmol) or AgCl (143 mg, 1.0 mmol) was stirred in 10 mL of dimethylsulfide for 12 hours (with protection from light in the case of AgCl). The reaction mixture was filtered and hexanes was added to precipitate the product. The solid was collected by filtration, washed with

diethyl ether and dried *in vacuo*. $(SMe_2)CuCl$ (yield: 147 mg, 91%) was obtained as a colorless crystalline solid, and $(SMe_2)AgCl$ (yield: 180 mg, 88%) was obtained as a white powder.

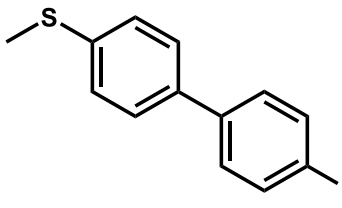

6

6. A 250 mL 2-neck round bottom flask equipped with a Teflon coated stir bar, reflux condenser with a gas inlet adapter, and rubber septum was charged with **3** (2.00 g, 11.9 mmol), 1,4-dibromobenzene (5.62 g, 24.0 mmol), and $PdCl_2(PPh_3)_2$ (0.25 g, 0.35 mmol). The flask was evacuated and refilled with N_2. In a separate flask, a mixture of 50 mL of dioxane and 25 mL of 2.0 M aqueous K_2CO_3 was sparged with N_2 for 30 min. The mixture was added to the 2-neck flask using a cannula, and the reaction was refluxed at 95°C and stirred for 3 h. The reaction was then opened to air and the dioxane was removed via rotary evaporation. Ethyl acetate (100 mL) was added to the flask and the mixture was filtered to remove the precipitated solid. The reaction mixture was transferred to a separatory funnel and the organic phase was separated from the aqueous phase. The aqueous phase was extracted with ethyl acetate (2 x 100 mL), and the combined organic extracts were then dried over $MgSO_4$ and concentrated *in vacuo*. The residue was purified by silica gel flash column chromatography, eluting with a 5-10% ethyl acetate in hexanes gradient. **6** was obtained as a white crystalline solid. (Yield: 1.92 g, 57%)

^{1}H NMR (400 MHz, $CDCl_3$): δ (ppm) 7.55 (d, *J* = 8.5 Hz, 2H), 7.48 (d, *J* = 8.4 Hz, 2H), 7.43 (d, *J* = 8.5 Hz, 2H), 7.32 (d, *J* = 8.4 Hz, 2H), 2.52 (s, 3H). ^{13}C{^{1}H} NMR (101 MHz, $CDCl_3$): δ (ppm) 139.46, 138.24, 136.74, 131.91, 128.39, 127.24, 126.98, 121.41, 15.84.

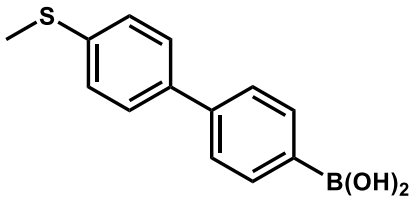

7

7. Synthesized following the same procedure as **3**, starting from **6** (1.0 g, 3.58 mmol). **7** was obtained as a white fluffy powder. (Yield: 664 mg, 76%)

^{1}H NMR (400 MHz, DMSO-d_6): δ (ppm) 8.03 (s, 2H), 7.86 (d, *J* = 7.7 Hz, 2H), 7.63 (dd, *J* = 10.5, 8.0 Hz, 4H), 7.35 (d, *J* = 8.5 Hz, 2H), 2.51 (s, 3H). ^{13}C{^{1}H} NMR (101 MHz, DMSO-d_6): δ (ppm) 140.83, 137.61, 136.53, 134.74, 132.97 127.05, 126.35, 125.20, 14.64.

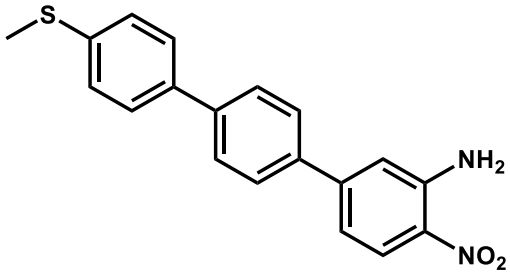

8

8. Synthesized following the same procedure as **4**, starting from **7** (265 mg, 2.0 mmol) and 5-chloro-2-nitroaniline (448mg, 2.6 mmol) with the following modifications. The solvent mixture used for the reaction is: 40 mL of dioxane, 100 μL of benzene and 10 mL of a 2.0 M aqueous K_2CO_3. After stirring under reflux for 18 h, the reaction mixture was hot filtered and dioxane was

removed by rotary evaporation. The precipitated solid was collected by filtration, washed with water (3 x 50 mL), and diethyl ether (3 x 50 mL). The solid was then redissolved in 150 mL of DCM, dried over $MgSO_4$, filtered, and the solvent was removed by rotary evaporator. The resulting solid was dried *in vacuo*. **8** was obtained as a bright yellow crystalline solid. (Yield: 405 mg, 78%) ^{1}H NMR (500 MHz, DMSO-d_6): δ (ppm) 8.06 (d, J = 9.0 Hz, 1H), 7.81 (d, J = 8.5 Hz, 2H), 7.74 (d, J = 8.2 Hz, 2H), 7.72–7.68 (m, 3H), 7.49 (s, 2H), 7.40–7.33 (m, 3H), 6.99 (dd, J = 9.0, 2.0 Hz, 1H), 2.52 (s, J = 1.2 Hz, 3H). ^{13}C{^{1}H} NMR (126 MHz, DMSO-d_6): δ (ppm) 146.47, 146.32, 139.90, 138.11, 136.94, 135.59, 129.53, 127.39, 127.06, 126.92, 126.35, 126.30, 116.16, 114.30, 14.60.

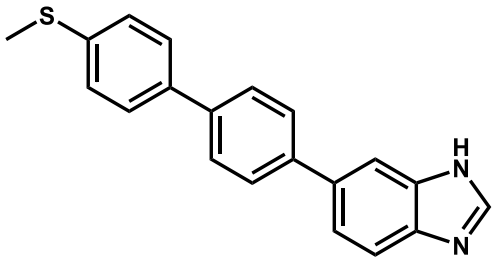

9

9. Synthesized following the same procedure as **5**, starting from **8** (250 mg, 790 μmol) with the following modifications. Benzene (100 μL) was added to the reaction to aid solubilizing the amine. After refluxing for 12 h, the mixture was hot filtered. The solid product was washed with ethyl acetate to remove excess starting material. **9** was obtained as a light yellow-orange powder. (Yield: 205 mg, 88%)

^{1}H NMR (500 MHz, DMSO-d_6): δ (ppm) 8.26 (s, 1H), 7.97 (br, 1H), 7.77 (dd, J = 9.6, 8.5 Hz, 4H), 7.69 (d, J = 8.2 Hz, 3H), 7.64–7.56 (m, 1H), 7.37 (d, J = 8.1 Hz, 2H), 2.52 (s, 3H). ^{13}C{^{1}H}

NMR (101 MHz, DMSO-d_6): δ (ppm) 143.29, 137.92, 137.37, 136.64, 136.40, 130.72, 127.87, 127.02, 126.92, 126.88, 126.85, 121.99, 121.06, 119.82, 112.46, 15.37.

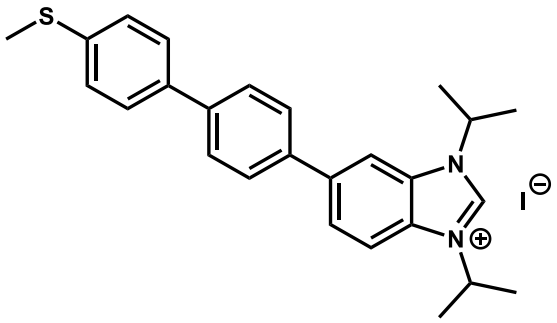

NHC2-HI

NHC2–HI. Synthesized following the same procedure as **NHC0–HI**, starting from **9** (100 mg, 316 μmol) with the following modifications. The reaction was stirred under reflux until consumption of the starting benzimidazole, as determined by NMR (typically ~72 h). An additional 4 equivalents of 2-iodopropane were added after 48 h. The product was precipitated using ethyl acetate. **NHC2–HI** was obtained as a white powder. (Yield: 24 mg, 14%)

^{1}H NMR (500 MHz, $CDCl_3$): δ (ppm) 11.10 (s, 1H), 7.92 (d, *J* = 8.7 Hz, 2H), 7.87 (d, *J* = 8.9 Hz, 1H), 7.76 (d, *J* = 7.8 Hz, 2H), 7.71 (d, *J* = 7.9 Hz, 2H), 7.61 (d, *J* = 8.2 Hz, 2H), 7.40 (d, *J* = 8.7 Hz, 2H), 5.27 (overlapping septets, 2H), 2.57 (s, 3H), 1.95 (overlapping doublets, 12H). ^{13}C{^{1}H} NMR (126 MHz, $CDCl_3$): δ (ppm) 140.85, 140.42, 140.37, 137.86, 136.69, 133.20, 131.65, 130.33, 128.03, 127.66, 127.39, 126.94, 126.75, 114.18, 111.72, 52.79, 52.55, 22.39, 22.39, 15.77.

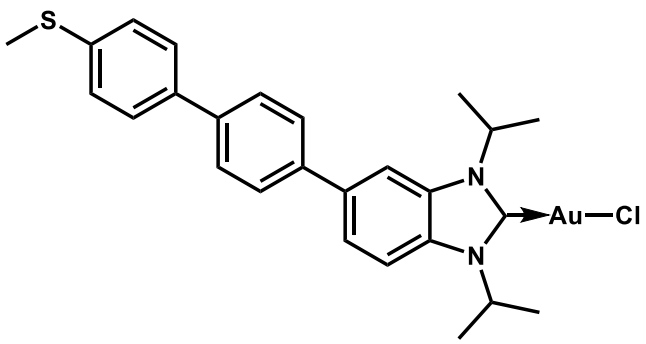

NHC2-AuCl

NHC2–AuCl. NHC2–AuCl was prepared following the general procedure outlined above for the synthesis of **NHC1–AuCl**, starting from **NHC2–HI** (10 mg, 18 μmol) KtOBu (2 mg, 21 μmol), and (SMe_2)AuCl (6 mg, 20 μmol). **NHC2–AuCl** was obtained as a white powder. (Yield: 11 mg, 90%)

X-ray diffraction quality crystals were grown by slow evaporation of a DCM solution of **NHC2–AuCl**.

^{1}H NMR (500 MHz, $CDCl_3$): δ (ppm) 7.84 (s, 1H), 7.73 (m, 3H), 7.68 (d, *J* = 7.7 Hz, 2H), 7.65 (d, *J* = 8.8 Hz, 1H), 7.61 (d, 2H), 7.39 (d, *J* = 7.9 Hz, 2H), 5.57 (overlapping septets, 2H), 2.57 (s, 3H), 1.81 (overlapping doublets, 12H). ^{13}C{^{1}H} NMR (126 MHz, $CDCl_3$): δ (ppm) 176.82, 140.17, 139.09, 138.23, 137.46, 137.01, 132.52, 131.73, 127.92, 127.47, 127.35, 126.95, 123.50, 113.30, 111.28, 54.58, 54.34, 21.81, 21.73, 15.82.

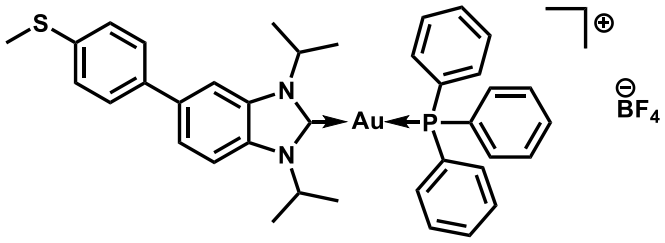

[NHC1-AuPPh$_3$][BF$_4$]

[NHC1–AuPPh$_3$][BF$_4$]. Synthesized following a modified literature procedure.[43] **NHC1–AuCl** (20 mg, 35 μmol) was dissolved in 5 mL of THF. In a separate vial, PPh_3 (9 mg, 36 μmol) and $AgBF_4$ (7 mg, 35 μmol) were dissolved in 5 mL of THF. This solution was added dropwise to the **NHC1–AuCl** solution and the reaction was stirred for 1 h, protected from light. The solution was then filtered, and the solvent was removed *in vacuo*. The residue was washed with hexanes. The resulting solid (yield: 22 mg, 73%) was a mixture of **[NHC1–AuPPh$_3$][BF$_4$]**, **[(NHC1)$_2$–Au][BF$_4$]**, and **[(PPh$_3$)$_2$Au][BF$_4$]**, as determined by NMR spectroscopy and reported characterization.[44] The **[NHC1–AuPPh$_3$][BF$_4$]:[(NHC1)$_2$–Au][BF$_4$]:[(PPh$_3$)$_2$Au][BF$_4$]** ratio in the final product is ca. 3:1:1. This mixture was used without further purification for the STM-BJ control experiment as **[NHC1–AuPPh$_3$][BF$_4$]** and **[(NHC1)$_2$–Au][BF$_4$]** should have the same conductance and **[(PPh$_3$)$_2$Au][BF$_4$]** will not conduct.

^{1}H NMR (400 MHz, $CDCl_3$): δ (ppm) 7.85–7.77 (m, 2H), 7.68–7.41 (bm, 15H), 7.67 (m, 1H), 7.56 (d, *J* = 8.4 Hz, 2H), 7.38 (d, *J* = 8.3 Hz, 2H), 5.34 (m, 2H), 2.54 (s, 3H), 1.94–1.83 (m, 12H). ^{13}C{^{1}H} NMR (101 MHz, $CDCl_3$): δ (ppm) 187.57, 138.78, 138.54, 136.62, 134.03, 133.29, 132.61, 131.73, 129.86, 127.89, 127.06, 124.77, 113.49, 110.75, 53.42, 53.24, 23.31, 23.16, 15.79. ^{31}P{^{1}H} NMR (162 MHz, $CDCl_3$): δ (ppm) 40.09.

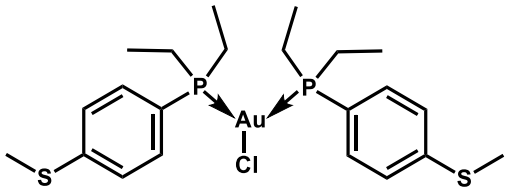

((4-MeSPh)Et$_2$P)$_2$AuCl

((4-MeSPh)Et$_2$P)$_2$AuCl. Prepared by adding a solution of diethyl(4-(methylthio)phenyl)phosphine[45] (79 mg, 370 μmol) in THF to a suspension of (SMe)$_2$AuCl (100 mg, 340 μmol) in THF. The reaction was stirred for 2 h. The suspension was then filtered and the solvent was removed *in vacuo*. The oily residue was dissolved in THF (~1 mL), layered with diethyl ether and placed in a freezer (-35°C) to crystallize. **((4-MeSPh)Et$_2$P)$_2$AuCl** was obtained as colorless crystals that melt at room temperature. (Yield: 33 mg, 13%)

^{1}H NMR (500 MHz, C_6D_6): δ (ppm) 7.51 (dd, *J* = 11.2, 8.1 Hz, 2H), 6.99 (d, *J* = 6.7 Hz, 2H), 1.90 (s, 3H), 1.87–1.56 (dm, 4H), 0.89 (dt, *J* = 19.6, 7.5 Hz, 6H). ^{13}C{^{1}H} NMR (126 MHz, C_6D_6): δ (ppm) 133.64, 133.54, 125.63, 125.54, 20.76, 20.49, 14.01, 8.96. ^{31}P{^{1}H} NMR (202 MHz, C_6D_6): δ (ppm) 38.10.

2.9 Single Crystal X-Ray Diffraction

Single crystal x-ray diffraction data was collected on an Agilent SuperNova diffractometer using mirror-monochromated CuK_α or MoK_α radiation. Data collection, integration, scaling (ABSPACK) and absorption correction (face-indexed Gaussian integration[46] or numeric analytical methods[47]) were performed in CrysAlisPro.[48] Structure solution was performed using ShelXT.[49] Subsequent refinement was performed by full-matrix least-squares on F^2 in ShelXL.[49] Olex2[50] was used for viewing and to prepare CIF files. Many disordered molecules were modeled as rigid fragments from the Idealized Molecular Geometry Library.[51] ORTEP graphics were prepared in

CrystalMaker.[52] Thermal ellipsoids are rendered at the 50% probability level. Details of crystallographic data and parameters for data collection and refinement are provided in Table 2.1.

Crystals were mounted on MiTeGen mounts with the aid of STP oil and cooled to 100 K on the diffractometer for screening and data collection, except in the case of **NHC1–AgCl** which was collected at room temperature. A minimum of 1 hemisphere of data to 0.8 Å resolution was collected for all compounds.

Structure solution and space group assignment were typically performed in ShelXT with no difficulty. In the final refinements, non-H atoms were refined anisotropically with no restraints unless noted; C-H hydrogens were placed in calculated positions and refined with riding isotropic ADPs and coordinates. The non-routine details of the refinements are given below:

NHC1–AuCl. Extinction correction was refined to 0.0090(8).

NHC2–AuCl. A molecule of dichloromethane was located in difference maps and modeled in two disordered positions. Each independent position was modeled as a rigid fragment with coordinates taken from the Idealized Molecular Geometry Library.

The final refinement had significant Fourier difference features (+/- 3-4 e- A-3) within 1-2 A of the gold atom. We could not identify any common reason (twinning, absorption) for these features and we conclude that the structure may suffer a whole-molecule disorder with an occupancy around 5% or less for the minor component. We were unable to build a disordered model that accounted for these difference features. However, the atomic positions and ADPs of the major component appear well-behaved in spite of the strongly featured difference map.

NHC1–CuCl. The terminal $C_6H_4SCH_3$ moiety was disordered over two positions in a 3:1 ratio. These were modeled with the following restraints: the two independent positions were made equivalent with SAME instructions; the anisotropic ADPs of the major component were stabilized with RIGU; the minor component was modeled with isotropic ADPs which were stabilized with SIMU. Each 8-atom C-C_6H_4-S group was also stabilized with a FLAT instruction

((4-MeSPh)Et$_2$P)$_2$AuCl. The asymmetric unit contains two independent ((4-MeSPh)Et$_2$P)$_2$AuCl molecules and four molecules of THF. One of the THFs is disordered over two positions in a near 1:1 ratio; these were modeled with the aid of SAME and RIGU restraints and a short-range SIMU instruction for overlapping ADPs.

Table 2.1: Selected Crystallographic Data

Compound	NHC0–AuCl	NHC1–AuCl	NHC2–AuCl
Formula	$C_{14}H_{20}AuClN_2S$	$C_{20}H_{24}N_2SClAu$	$C_{27}H_{30}AuCl_3N_2S$
MW	480.8	556.89	717.9
Space group	P-1	P-1	C2/c
***a* (Å)**	9.3400(5)	8.5453(3)	32.2745(12)
***b* (Å)**	9.4284(5)	10.0951(3)	7.7536(2)
***c* (Å)**	9.9843(5)	12.3151(4)	23.0815(7)
***α* (°)**	80.472(4)	104.024(3)	90
***β* (°)**	72.891(5)	106.985(3)	109.981(4)
***γ* (°)**	73.520(4)	94.210(3)	90
V (Å^3)	802.56(8)	973.77(6)	5428.4(3)
Z	2	2	8
ρ_{calc} (g cm^{-3})	1.99	1.899	1.757
T (K)	100	100.0(2)	99.9(2)
λ (Å)	1.54184	1.54184	1.54184
$2\theta_{min}$, $2\theta_{max}$	9.306, 146.01	7.81, 145.894	8.152,146.286
Nref	6986	8851	36522
R(int), R(σ)	0.0335, 0.0391	0.0277, 0.0273	0.0383, 0.0258
μ(mm^{-1})	19.868	16.486	13.762
Size (mm)	0.16 × 0.128 × 0.078	0.369 × 0.16 × 0.093	0.162 × 0.081 × 0.015
T_{max}, T_{min}	0.758, 0.355	0.638, 0.100	0.810, 0.275
Data	3175	3877	5405
Restraints	0	0	32
Parameters	177	232	334
R_1(obs)	0.0406	0.0239	0.0586
wR_2(all)	0.1055	0.0616	0.1522
S	1.064	1.115	1.118
Peak, hole (e$^-$ Å^{-3})	1.95, -3.58	0.9, -1.09	3.35, -3.71
CCDC deposition #	1832127	1832128	1832129

Compound	NHC1–CuCl	NHC1–AgCl	((4-SMePh)Et$_2$P)$_2$AuCl
Formula	$C_{20.5}H_{25}Cl_2CuN_2S$	$C_{21}H_{26}AgCl_3N_2S$	$C_{30}H_{50}AuClO_2P_2S_2$
MW	465.92	1105.43	801.17
Space group	$P2_1/c$	$P2_1/n$	$P2_1/c$
***a* (Å)**	12.3475(8)	14.2598(6)	22.3899(2)
***b* (Å)**	7.5762(7)	11.7679(5)	17.95980(10)
***c* (Å)**	23.0412(16)	15.0014(7)	18.6379(2)
***α* (°)**	90	90	90
***β* (°)**	104.263(7)	106.365(5)	111.6290(10)
***γ* (°)**	90	90	90
V (Å^3)	2089.0(3)	2415.37(19)	6966.94(11)
Z	4	4	8
ρ_{calc} (g cm^{-3})	1.481	1.52	1.528
T (K)	100.0(2)	293.94(19)	99.97(10)
λ (Å)	0.71073	1.54184	1.54184
$2\theta_{min}$, $2\theta_{max}$	6.81, 59.308	6.636, 59.204	7.09, 145.846
Nref	9914	11063	94068
R(int), R(σ)	0.0665, 0.1169	0.0283, 0.0468	0.0542, 0.0331
μ(mm^{-1})	1.409	1.262	10.814
Size (mm)	0.251 × 0.071 × 0.027	0.384 × 0.175 × 0.088	0.256 × 0.131 × 0.092
T_{max}, T_{min}	1.0, 0.805	0.979, 0.954	0.452, 0.183
Data	4913	5599	13776
Restraints	156	0	156
Parameters	284	259	743
R_1(obs)	0.068	0.0533	0.0363
wR_2(all)	0.1621	0.144	0.0942
S	1.062	1.085	1.103
Peak, hole (e$^-$ Å^{-3})	0.93, -1.13	0.83, -0.64	2.79, -1.23
CCDC deposition #	1832131	1832132	1832130

Crystal Structures: All thermal ellipsoids are rendered at the 50% probability level.

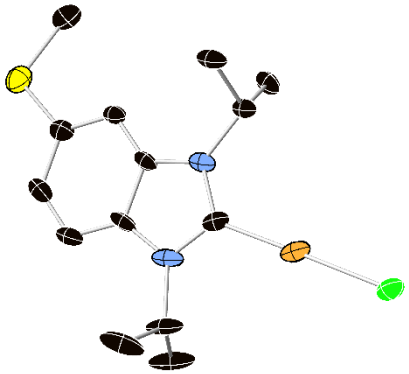

Figure 2.6: Crystal structure of NHC0–AuCl. Colour code: Au, gold; Cl, green; S, yellow; N, light blue; C, black. H atoms are removed for clarity.

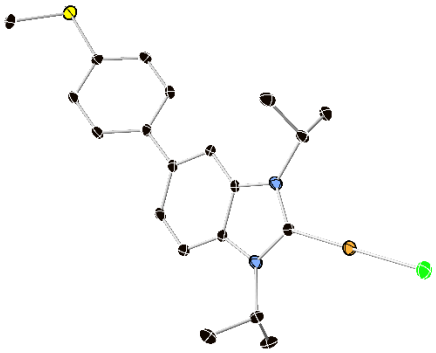

Figure 2.7: Crystal structure of NHC1–AuCl. Colour code: Au, gold; Cl, green; S, yellow; N, light blue; C, black. H atoms are removed for clarity.

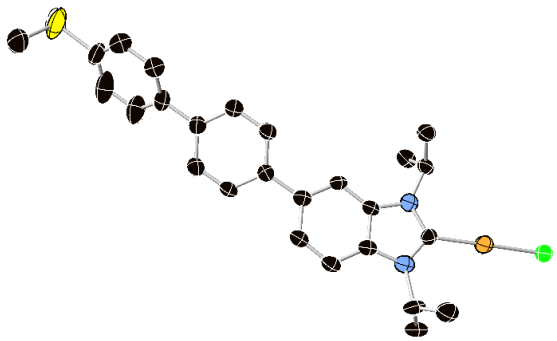

Figure 2.8: Crystal structure of NHC2–AuCl. Colour code: Au, gold; Cl, green; S, yellow; N, light blue; C, black. H atoms are removed for clarity.

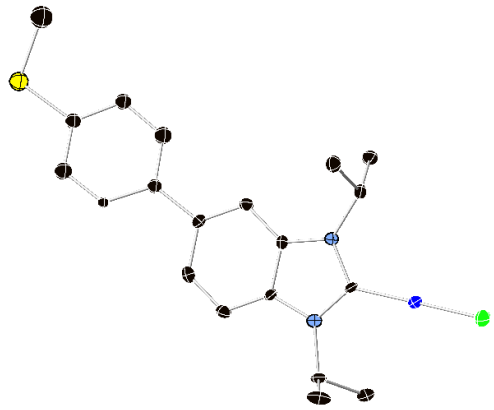

Figure 2.9: Crystal structure of NHC1–CuCl. Colour code: Cu, dark blue; Cl, green; S, yellow; N, light blue; C, black. H atoms are removed for clarity.

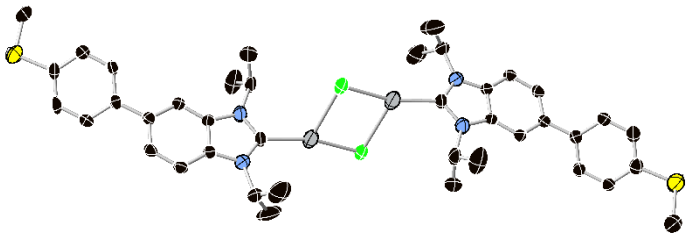

Figure 2.10: Complete crystal structure of NHC1–AgCl. Colour code: Ag, grey; Cl, green; S, yellow; N, light blue; C, black. H atoms are removed for clarity.

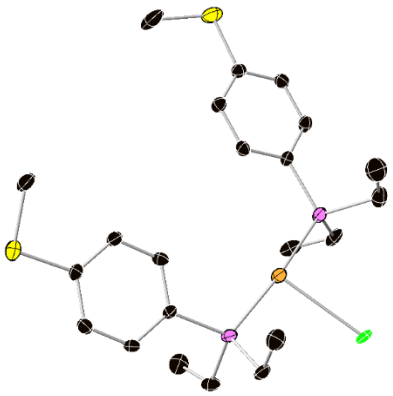

Figure 2.11: Crystal structure of ((4-MeSPh)Et_2P)$_2$AuCl. Colour code: Au, gold; Cl, green; S, yellow; P, pink; C, black. H atoms are removed for clarity.

2.10 Additional STM-BJ Data

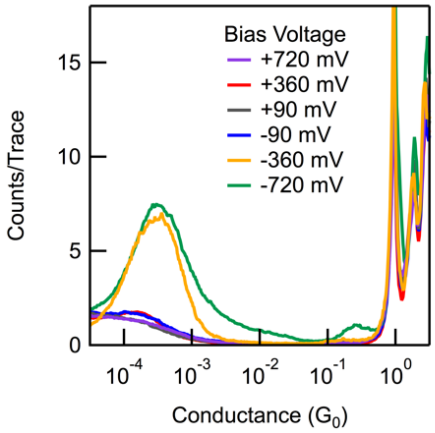

Figure 2.12: Bias Dependence. Conductance histograms for **NHC1–AuCl** as a function of tip bias measured in PC.

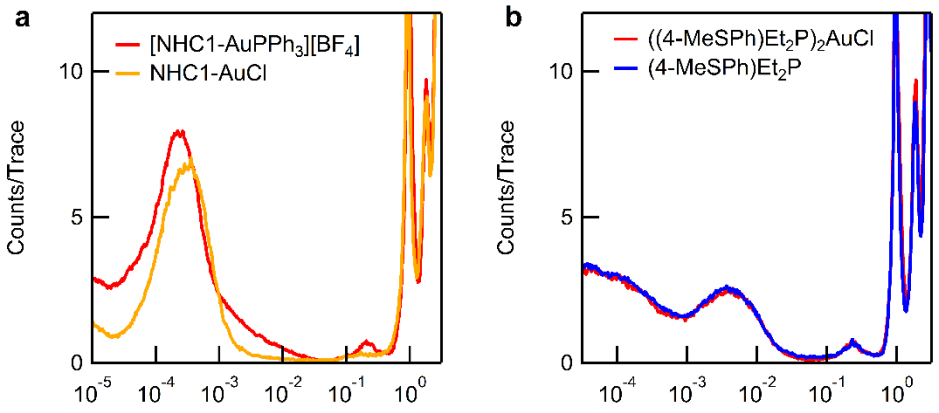

Figure 2.13: Control Measurements. **a.** Conductance histogram for [**NHC1–AuPPh$_3$][BF$_4$]** compared with that of **NHC1–AuCl** measured in PC at –360 mV tip bias. **b.** Conductance histograms of the complex **((4-MeSPh)Et$_2$P)$_2$AuCl** and the free ligand **(4-MeSPh)Et$_2$P** (without a AuCl terminal group) measured in PC at –360 mV tip bias.

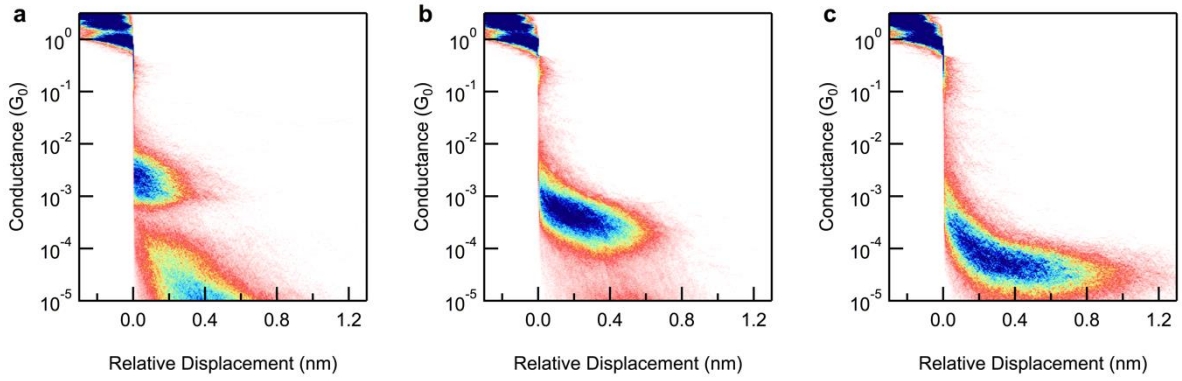

Figure 2.14: Conductance-displacement of NHC*n*–AuCl. Two-dimensional conductance-displacement histograms for **a. NHC0–AuCl**, **b. NHC1–AuCl** and **c. NHC2–AuCl**. Corresponding 1D histograms are shown in Figure 2.3b.

2.11 Additional Computational Data

In order to determine the individual contributions of NHC and SMe terminations to the binding energy, three different junction terminations were considered: (a) A molecule terminated

with two NHC linkers, (b) a molecule terminated with two SMe linkers, or (c) molecules with one NHC and one SMe linker. Exemplary junction structures are shown in Figure 2.15.

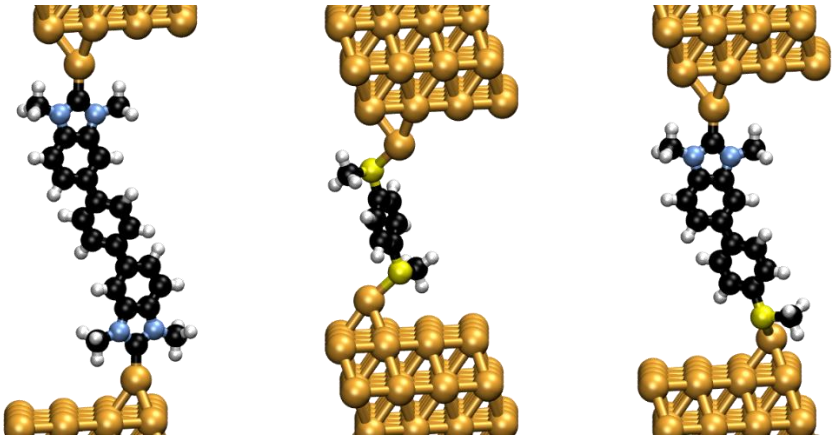

Figure 2.15: Junction structures used to calculate molecular binding energies. **a.** A biscarbene junction with one phenyl group. **b.** A bis-SMe junction with one phenyl group. **c.** An **NHC1–Au** junction.

Values of the binding energy of these junctions with different numbers of phenyl groups are given in Table 2.2 and include corrections to basis set superposition errors.[53] Positive values denote stable junctions with respect to the Au structure and isolated molecules. From the junctions with equal linker groups at both ends, the binding energy of a single NHC or SMe bond to Au is evaluated. For the junctions realized in experiment, most of the binding energy comes from the NHC-Au bond.

Table 2.2: Calculated binding energies (eV).

Number of Phenyls	**NHC-NHC**	**SMe-SMe**	**NHC-SMe**
0	4.19		2.88
1	4.14	1.43	2.73
2	4.17	1.40	2.69
Average	4.17	1.42	2.77
Average per bond	2.08	0.71	

The binding energies of the **NHC1–Au**, **NHC1–Ag** and **NHC1–Cu** junctions are 2.73, 2.35 and 2.75 eV, respectively. Subtracting the contribution of the SMe-Au contact, the binding energies of the NHC–Au, NHC–Ag and NHC–Cu bonds are 2.02, 1.64 and 2.04 eV. These results follow the trend in bond strength of M = Cu ≈ Au > Ag measured and calculated previously for nitrene fragments to a IMesM+ moiety.[54]

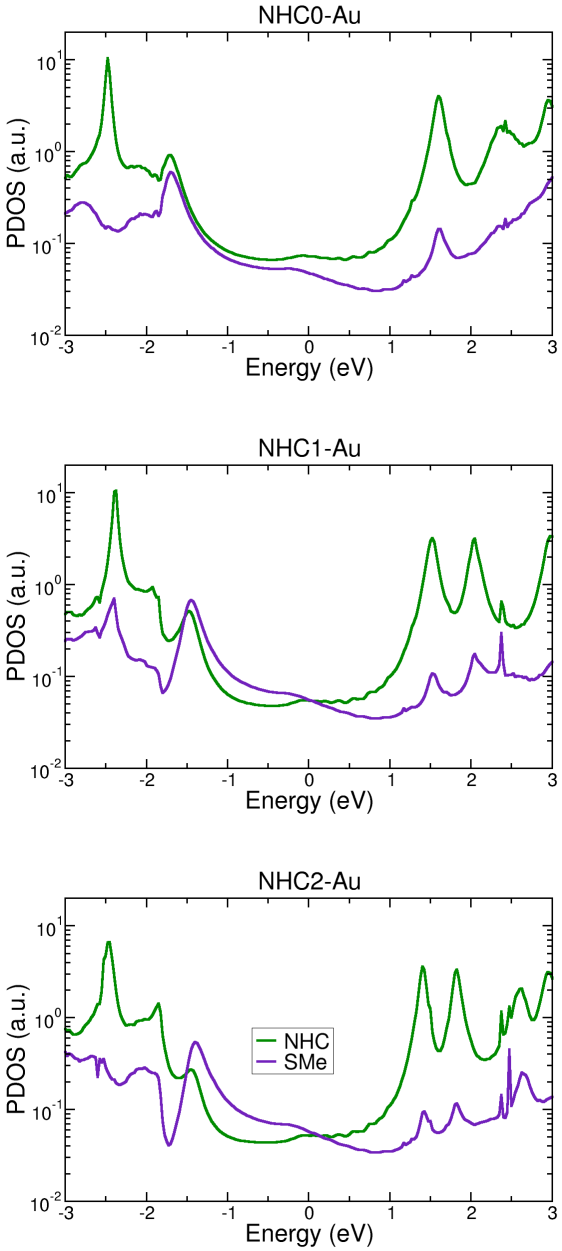

Figure 2.16: Projected density of states (PDOS) onto NHC and SMe linkers. PDOS onto the molecular atoms forming the NHC and on the SMe terminations, calculated from the Green's function. NHC features dominate the spectrum near the gap, except near –1.5 eV, where SMe states are important, more so for longer molecules.

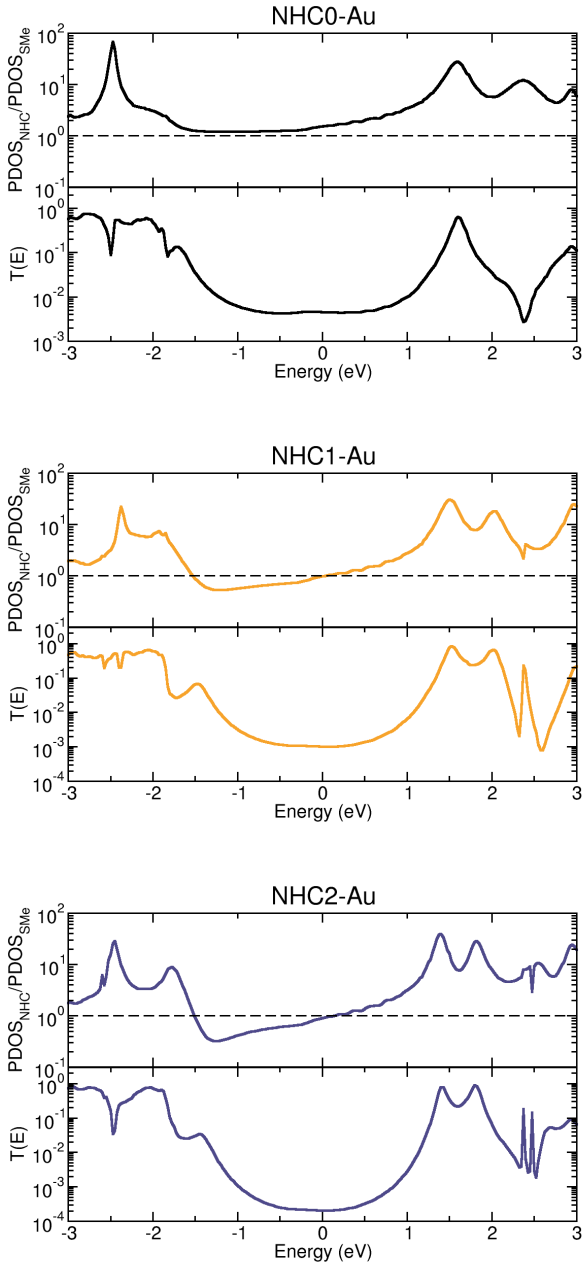

Figure 2.17: Ratio of NHC and SMe PDOS. Ratio of the PDOS on the NHC to the SMe units (top panels) and calculated transmission spectra (bottom panels).

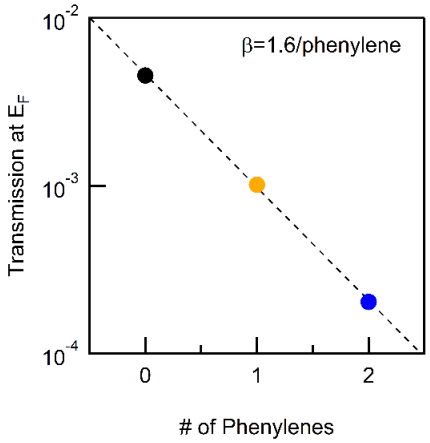

Figure 2.18: Exponential fit to calculated transmission values at E_f.

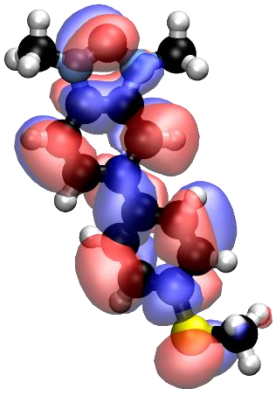

Figure 2.19: LUMO of the NHC1 free carbene.

We calculate the electronic transmission through molecular orbitals by projecting the electronic coupling matrix to the electrode for the NHC- or SMe-terminated contacts ($\Gamma_{NHC,SMe}$) onto eigenstates of the **NHC1** molecule. In the expression for the transmission function, one can introduce the completeness relation to obtain:

$$T = tr[G\Gamma_{NHC}G^{\dagger}\Gamma_{SMe}] = tr\left[G\sum_i|\psi_i\rangle\langle\psi_i|\Gamma_{NHC}\sum_j|\psi_j\rangle\langle\psi_j|G^{\dagger}\sum_k|\psi_k\rangle\langle\psi_k|\Gamma_{SMe}\sum_l|\psi_l\rangle\langle\psi_l|\right]$$

where ψ_i form a complete and orthogonal basis in a subspace of the full device (such as the molecule). For clarity, the dependence on energy and k-points is omitted. The matrix elements $\langle\psi_i|\Gamma_{NHC,SMe}|\psi_j\rangle$ represent the electronic coupling of eigenstates *i* and *j* to the leads on the NHC- or SMe-terminated contacts. Transmission through specific molecular orbitals is given by diagonal terms $\langle\psi_i|\Gamma_{NHC,SMe}|\psi_i\rangle$. Because these projections include only some terms of the total transmission, at certain energies the projected transmission can be higher than the total, indicating that other terms which decrease transmission are included in the projection.[31, 55]

Figure 2.20 shows the calculated spectra projecting the coupling matrix of either the NHC- or SMe-terminated contacts, onto the **NHC1** HOMO. From the spectral analysis, the HOMO is localized mostly on the SMe linker. The transmission spectra projected onto the HOMO are much smaller than the total transmission, even at energies close to the HOMO resonance around –1.5 eV, demonstrating that this orbital is not well coupled to either electrode.

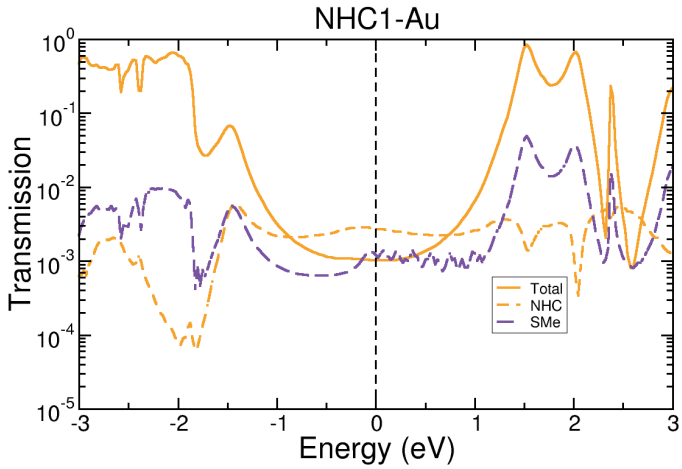

Figure 2.20: Calculated transmission spectra of **NHC1–Au** projecting the coupling matrices Γ at the NHC- or SMe-terminated contacts onto the HOMO of **NHC1**.

Figure 2.21 shows the calculated spectra projecting the coupling matrices onto the **NHC1** LUMO. Remarkably, the LUMO alone provides almost the total electronic transparency of the junction over more than 1 eV. This demonstrates that the NHC termination, which sets the character of the LUMO, provides excellent coupling for electron transport.

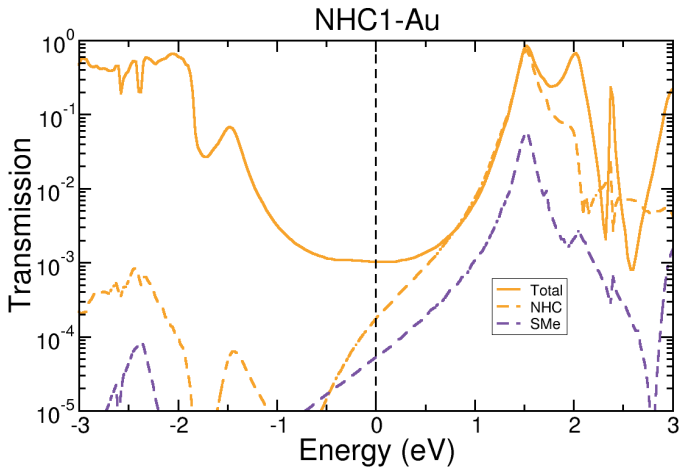

Figure 2.21: Calculated transmission spectra of **NHC1–Au** projecting the coupling matrices Γ at the NHC- or SMe-terminated contacts onto the LUMO of **NHC1**.

2.12 References

1. Reed, M. A.; Zhou, C.; Muller, C. J.; Burgin, T. P.; Tour, J. M., Conductance of a molecular junction. *Science* **1997,** *278*, 252-254.

2. Xu, B. Q.; Tao, N. J., Measurement of single-molecule resistance by repeated formation of molecular junctions. *Science* **2003,** *301*, 1221-1223.

3. Cheng, Z. L.; Skouta, R.; Vazquez, H.; Widawsky, J. R.; Schneebeli, S.; Chen, W.; Hybertsen, M. S.; Breslow, R.; Venkataraman, L., In situ formation of highly conducting covalent Au-C contacts for single-molecule junctions. *Nature Nanotechnology* **2011,** *6*, 353-357.

4. Zang, Y.; Pinkard, A.; Liu, Z.-F.; Neaton, J. B.; Steigerwald, M. L.; Roy, X.; Venkataraman, L., Electronically transparent Au-N bonds for molecular junctions. *Journal of the American Chemical Society* **2017,** *139*, 14845-14848.

5. Park, Y. S.; Whalley, A. C.; Kamenetska, M.; Steigerwald, M. L.; Hybertsen, M. S.; Nuckolls, C.; Venkataraman, L., Contact Chemistry and Single- Molecule Conductance: A Comparison of Phosphines, Methyl Sulfides, and Amines. *Journal of the American Chemical Society* **2007,** *129*, 15768-15769.

6. Martin, C. A.; Ding, D.; Sorensen, J. K.; Bjornholm, T.; van Ruitenbeek, J. M.; van der Zant, H. S. J., Fullerene-based anchoring groups for molecular electronics. *Journal of the American Chemical Society* **2008,** *130*, 13198-13199.

7. Bourissou, D.; Guerret, O.; Gabbai, F. P.; Bertrand, G., Stable Carbenes. *Chem Rev* **2000,** *100*, 39-92.

8. Arduengo, A. J.; Harlow, R. L.; Kline, M., A Stable Crystalline Carbene. *Journal of the American Chemical Society* **1991,** *113*, 361-363.

9. Hopkinson, M. N.; Richter, C.; Schedler, M.; Glorius, F., An overview of N-heterocyclic carbenes. *Nature* **2014,** *510*, 485-496.

10. Zhukhovitskiy, A. V.; MacLeod, M. J.; Johnson, J. A., Carbene Ligands in Surface Chemistry: From Stabilization of Discrete Elemental Allotropes to Modification of Nanoscale and Bulk Substrates. *Chem Rev* **2015,** *115*, 11503-11532.

11. Zhukhovitskiy, A. V.; Mavros, M. G.; Van Voorhis, T.; Johnson, J. A., Addressable carbene anchors for gold surfaces. *J Am Chem Soc* **2013,** *135*, 7418-7421.

12. Crudden, C. M.; Horton, J. H.; Ebralidze, II; Zenkina, O. V.; McLean, A. B.; Drevniok, B.; She, Z.; Kraatz, H. B.; Mosey, N. J.; Seki, T.; Keske, E. C.; Leake, J. D.; Rousina-Webb, A.; Wu, G., Ultra stable self-assembled monolayers of N-heterocyclic carbenes on gold. *Nat Chem* **2014,** *6*, 409-414.

13. Crudden, C. M.; Horton, J. H.; Narouz, M. R.; Li, Z.; Smith, C. A.; Munro, K.; Baddeley, C. J.; Larrea, C. R.; Drevniok, B.; Thanabalasingam, B.; McLean, A. B.; Zenkina, O. V.; Ebralidze, I. I.; She, Z.; Kraatz, H.-B.; Mosey, N. J.; Saunders, L. N.; Yagi, A., Simple direct formation of self-assembled N-heterocyclic carbene monolayers on gold and their application in biosensing. *Nature Communications* **2016,** *7*, 12654.

14. Herrmann, W. A.; Elison, M.; Fischer, J.; Köcher, C.; Artus, G. R. J., Metal Complexes of N-Heterocyclic Carbenes—A New Structural Principle for Catalysts in Homogeneous Catalysis. *Angewandte Chemie International Edition in English* **1995,** *34*, 2371-2374.

15. Vougioukalakis, G. C.; Grubbs, R. H., Ruthenium-Based Heterocyclic Carbene-Coordinated Olefin Metathesis Catalysts. *Chemical Reviews* **2010,** *110*, 1746-1787.

16. Fortman, G. C.; Nolan, S. P., N-Heterocyclic carbene (NHC) ligands and palladium in homogeneous cross-coupling catalysis: a perfect union. *Chemical Society Reviews* **2011,** *40*, 5151-5169.

17. Huynh, H. V., *The Organometallic Chemistry of N-Heterocyclic Carbenes*. Wiley: 2017.

18. Ott, L. S.; Cline, M. L.; Deetlefs, M.; Seddon, K. R.; Finke, R. G., Nanoclusters in Ionic Liquids: Evidence for N-Heterocyclic Carbene Formation from Imidazolium-Based Ionic Liquids Detected by 2H NMR. *Journal of the American Chemical Society* **2005,** *127*, 5758-5759.

19. Hurst, E. C.; Wilson, K.; Fairlamb, I. J. S.; Chechik, V., N-Heterocyclic carbene coated metal nanoparticles. *New Journal of Chemistry* **2009,** *33*, 1837-1840.

20. Weidner, T.; Baio, J. E.; Mundstock, A.; Große, C.; Karthäuser, S.; Bruhn, C.; Siemeling, U., NHC-Based Self-Assembled Monolayers on Solid Gold Substrates. *Australian journal of chemistry* **2011,** *64*, 1177-1179.

21. Foti, G.; Vázquez, H., Tip-induced gating of molecular levels in carbene-based junctions. *Nanotechnology* **2016,** *27*, 125702.

22. Kim, H. K.; Hyla, A. S.; Winget, P.; Li, H.; Wyss, C. M.; Jordan, A. J.; Larrain, F. A.; Sadighi, J. P.; Fuentes-Hernandez, C.; Kippelen, B.; Brédas, J.-L.; Barlow, S.; Marder, S. R., Reduction of the Work Function of Gold by N-Heterocyclic Carbenes. *Chemistry of Materials* **2017,** *29*, 3403-3411.

23. Venkataraman, L.; Klare, J. E.; Nuckolls, C.; Hybertsen, M. S.; Steigerwald, M. L., Dependence of single-molecule junction conductance on molecular conformation. *Nature* **2006,** *442*, 904-907.

24. Nagahara, L. A.; Thundat, T.; Lindsay, S. M., Preparation and Characterization of Stm Tips for Electrochemical Studies. *Review of Scientific Instruments* **1989,** *60*, 3128-3130.

25. Wang, G.; Ruhling, A.; Amirjalayer, S.; Knor, M.; Ernst, J. B.; Richter, C.; Gao, H. J.; Timmer, A.; Gao, H. Y.; Doltsinis, N. L.; Glorius, F.; Fuchs, H., Ballbot-type motion of N-heterocyclic carbenes on gold surfaces. *Nat Chem* **2017,** *9*, 152-156.

26. Capozzi, B.; Chen, Q.; Darancet, P.; Kotiuga, M.; Buzzeo, M.; Neaton, J. B.; Nuckolls, C.; Venkataraman, L., Tunable Charge Transport in Single-Molecule Junctions via Electrolytic Gating. *Nano Letters* **2014,** *14*, 1400-1404.

27. Capozzi, B.; Xia, J. L.; Adak, O.; Dell, E. J.; Liu, Z. F.; Taylor, J. C.; Neaton, J. B.; Campos, L. M.; Venkataraman, L., Single-molecule diodes with high rectification ratios through environmental control. *Nature Nanotechnology* **2015,** *10*, 522-U101.

28. Lovat, G.; Choi, B.; Paley, D. W.; Steigerwald, M. L.; Venkataraman, L.; Roy, X., Room-temperature current blockade in atomically defined single-cluster junctions. *Nat Nanotechnol* **2017,** *12*, 1050-1054.

29. Quek, S. Y.; Choi, H. J.; Louie, S. G.; Neaton, J. B., Length dependence of conductance in aromatic single-molecule junctions. *Nano Lett* **2009,** *9*, 3949-3953.

30. Soler, J. M.; Artacho, E.; Gale, J. D.; Garcia, A.; Junquera, J.; Ordejon, P.; Sanchez-Portal, D., The SIESTA method for ab initio order-N materials simulation. *Journal of Physics-Condensed Matter* **2002,** *14*, 2745-2779.

31. Papior, N.; Lorente, N.; Frederiksen, T.; Garcia, A.; Brandbyge, M., Improvements on non-equilibrium and transport Green function techniques: The next-generation TRANSIESTA. *Computer Physics Communications* **2017,** *212*, 8-24.

32. Perdew, J. P.; Burke, K.; Ernzerhof, M., Generalized gradient approximation made simple. *Physical Review Letters* **1996,** *77*, 3865-3868.

33. Paulsson, M.; Brandbyge, M., Transmission eigenchannels from nonequilibrium Green's functions. *Physical Review B* **2007,** *76*.

34. Kamenetska, M.; Koentopp, M.; Whalley, A. C.; Park, Y. S.; Steigerwald, M. L.; Nuckolls, C.; Hybertsen, M. S.; Venkataraman, L., Formation and Evolution of Single-Molecule Junctions. *Physical Review Letters* **2009,** *102*.

35. Lavrich, D. J.; Wetterer, S. M.; Bernasek, S. L.; Scoles, G., Physisorption and Chemisorption of Alkanethiols and Alkyl Sulfides on Au(111). *The Journal of Physical Chemistry B* **1998,** *102*, 3456-3465.

36. Pontes, R. B.; Novaes, F. D.; Fazzio, A.; da Silva, A. J. R., Adsorption of benzene-1,4-dithiol on the Au(111) surface and its possible role in molecular conductance. *Journal of the American Chemical Society* **2006,** *128*, 8996-8997.

37. Hybertsen, M. S.; Venkataraman, L., Structure-Property Relationships in Atomic-Scale Junctions: Histograms and Beyond. *Accounts of Chemical Research* **2016,** *49*, 452-460.

38. Vazquez, H.; Skouta, R.; Schneebeli, S.; Kamenetska, M.; Breslow, R.; Venkataraman, L.; Hybertsen, M. S., Probing the conductance superposition law in single-molecule circuits with parallel paths. *Nature Nanotechnology* **2012,** *7*, 663-667.

39. Hammer, B.; Morikawa, Y.; Norskov, J. K., CO chemisorption at metal surfaces and overlayers. *Phys Rev Lett* **1996,** *76*, 2141-2144.

40. Chakraborty, P., Sodium Methanethiolate. In *Encyclopedia of Reagents for Organic Synthesis*, John Wiley & Sons, Ltd: 2001.

41. Kuntz, K.; Emmitte, K. A.; Rheault, T. R.; Smith, S.; Hornberger, K.; Dickson, H.; Cheung, M. New benzimidazole thiophene compound useful for treating e.g. gastric cancer, gastric cancer, chronic wound healing and organ transplant rejection. US2008300247-A1; US2009124615-A9; US7615643-B2.

42. Gonell, S.; Poyatos, M.; Peris, E., Triphenylene-Based Tris(N-Heterocyclic Carbene) Ligand: Unexpected Catalytic Benefits. *Angewandte Chemie-International Edition* **2013,** *52*, 7009-7013.

43. Jahnke, M. C.; Pape, T.; Hahn, F. E., Ligand Exchange at a Gold(I) Carbene Complex. *Zeitschrift Fur Naturforschung Section B-a Journal of Chemical Sciences* **2013,** *68*, 467-473.

44. Gaillard, S.; Nun, P.; Slawin, A. M. Z.; Nolan, S. P., Expeditious Synthesis of [Au(NHC)(L)](+) (NHC = N-Heterocyclic Carbene; L = Phosphine or NHC) Complexes. *Organometallics* **2010,** *29*, 5402-5408.

45. Roy, X.; Schenck, C. L.; Ahn, S.; Lalancette, R. A.; Venkataraman, L.; Nuckolls, C.; Steigerwald, M. L., Quantum Soldering of Individual Quantum Dots. *Angewandte Chemie-International Edition* **2012,** *51*, 12473-12476.

46. Blanc, E.; Schwarzenbach, D.; Flack, H. D., The evaluation of transmission factors and their first derivatives with respect to crystal shape parameters. *Journal of Applied Crystallography* **1991,** *24*, 1035-1041.

47. Clark, R. C.; Reid, J. S., The analytical calculation of absorption in multifaceted crystals. *Acta Crystallographica Section A* **1995,** *51*, 887-897.

48. *CrysAlisPro*, Version 1.171.37.35; Oxford Diffraction /Agilent Technologies UK Ltd: Yarnton, England, 2014.

49. Sheldrick, G., SHELXT - Integrated space-group and crystal-structure determination. *Acta Crystallographica Section A* **2015,** *71*, 3-8.

50. Dolomanov, O. V.; Bourhis, L. J.; Gildea, R. J.; Howard, J. A. K.; Puschmann, H., OLEX2: a complete structure solution, refinement and analysis program. *Journal of Applied Crystallography* **2009,** *42*, 339-341.

51. Guzei, I., An idealized molecular geometry library for refinement of poorly behaved molecular fragments with constraints. *Journal of Applied Crystallography* **2014,** *47*, 806-809.

52. *CrystalMaker*, CrystalMaker Software Ltd: Oxford, England.

53. Vanduijneveldt, F. B.; Vanduijneveldtvanderijdt, J. G. C. M.; Vanlenthe, J. H., State-of-the-Art in Counterpoise Theory. *Chemical Reviews* **1994,** *94*, 1873-1885.

54. Fedorov, A.; Couzijn, E. P. A.; Nagornova, N. S.; Boyarkin, O. V.; Rizzo, T. R.; Chen, P., Structure and Bonding of Isoleptic Coinage Metal (Cu, Ag, Au) Dimethylaminonitrenes in the Gas Phase. *Journal of the American Chemical Society* **2010,** *132*, 13789-13798.

55. Schneider, N. L.; Neel, N.; Andersen, N. P.; Lu, J. T.; Brandbyge, M.; Kroger, J.; Berndt, R., Spectroscopy of transmission resonances through a C-60 junction. *Journal of Physics-Condensed Matter* **2015,** *27*.

Chapter 3: Determination of the Structure and Geometry of N-Heterocyclic Carbenes on Au(111) Using High-Resolution Spectroscopy

3.1 Preface

Significant portions of this chapter are adapted from a publication on this research entitled "Determination of the Structure and Geometry of N-Heterocyclic Carbenes on Au(111) Using High-Resolution Spectroscopy" by Giacomo Lovat, Evan A. Doud, Deyu Liu, Gregor Kladnik, Michael S. Inkpen, Michael L. Steigerwald, Dean Cvetko, Mark S. Hybertsen, Alberto Morgante, Xavier Roy, and Latha Venkataraman published in *Chemical Science*, **2019**, 10, 930-935. I synthesized and characterized the compounds used in this study and aided in writing the manuscript. Dr. Giacomo Lovat of the Venkataraman lab performed many of the spectroscopic measurements with assistance from several of the other authors.

3.2 Introduction

NHCs are exceptionally strong σ-donor ligands capable of binding to virtually any transition metal. They are receiving increasing interest for their ability to form functional self-assembled monolayers (SAMs) on metal surfaces.[1-8] Johnson, Crudden and their respective coworkers have demonstrated that NHC-based SAMs exhibit remarkable thermal and chemical stability that go well beyond thiol-based SAMs on Au,[1, 7] opening the door to novel applications in selective heterogeneous catalysis,[9-10] nanotechnology[11] and sensing.[2] Moreover, the strength and directionality of NHC–metal bonds, by now well-established in coordination chemistry, offer

exciting new possibilities for passivating and/or manipulating the work function of metal surfaces.[12] While a substantial body of work has been devoted to NHCs since their discovery,[13-21] this research has thus far mainly focused on the design of homogeneous catalysts. By contrast, many fundamental questions regarding the structure of NHC SAMs and their electronic coupling with metal surfaces remain unanswered.[1, 7-8, 22] Recently, some unique insights have been provided through the application of NHCs as linker groups in molecular-scale electronics.[23-26] Additionally, investigating these interactions could aid in the development of novel superatomic materials utilizing the unique properties of NHCs.

To date, most models of NHC-bound SAMs on metal surfaces postulate that the molecules adopt an upright geometry, with the heterocyclic system perpendicular to the surface.[7-8, 22, 27-30] In this orientation, a donor–acceptor interaction from the carbene lone pair to a surface atom is the primary contribution to the NHC–metal bond. In contrast, Baddeley, Papageorgiou, and their respective co-workers recently reported that some NHCs can form flat-lying mononuclear complexes $(NHC)_2M$ (M = Cu, Ag, Au) on surfaces, where the coordinated metal site is pulled out of the surface plane.[23, 31] Such adatoms are key structural components in SAMs of thiol molecules on Au(111),[32] and provide a clear experimental signature of surface reorganization induced by strong molecule–surface interactions. With the exception of a single report utilizing high resolution electron energy loss spectroscopy (HREELS),[25] the conflicting conclusions regarding the structure of NHC SAMs may be attributed to the use of scanning tunneling microscope (STM) imaging or low resolution X-ray photoelectron spectroscopy (LR-XPS) to probe these systems.[26] Such methods do not provide the chemical sensitivity required to determine the precise orientation of NHCs in SAMs, the nature of their bonding to the surface, or the unambiguous detection of any

associated Au adatoms. As a result, the role of N-substituents in influencing NHC SAM structure remains ill-defined.

In this work, we use synchrotron radiation to perform high-resolution X-ray photoelectron spectroscopy (HR-XPS) and near-edge X-ray absorption fine-structure spectroscopy (NEXAFS), and combine these measurements with density functional theory (DFT) calculations to establish a detailed picture of the geometry and bonding of a series of NHCs assembled on Au(111) in ultra-high vacuum (UHV). HR-XPS is highly sensitive to the chemical composition of the NHC layer and detects small changes to core-level electron binding energies that result from NHC–Au interactions, providing unique measurements of surface coverage and surface adatom density. NEXAFS allows us to unequivocally determine the orientation of the molecules relative to the surface by probing their unoccupied electronic states. Such information is key to understanding the relationship between the NHC molecular structure and their adsorption geometry. It can be obtained clearly through spectroscopic measurements. In contrast, surface imaging techniques only focus on small areas of the surface and they cannot resolve precisely the orientation of molecules bound to the surface. By rationalizing our experimental results using DFT calculations, we quantify the impact of the NHC structure and conformation on the strength of the molecule–Au interaction. Importantly, we show that through changes in the substituents on the N atoms, we can alter the steric environment around the carbenic C atom, which strongly affects the surface tilt angle and adsorption behavior of the molecules. This study complements and extends previous important efforts to characterize these systems. It further shows how thermal annealing in combination with careful selection of N-substituents can modulate the structure of NHCs on Au(111) surfaces.

3.3 Compounds Studied and Monolayer Formation

Three NHCs with different steric properties are investigated: 1,3-dimethylimidazol-2-ylidene (NHC^{Me}), 1,3-diisopropylbenzimidazol-2-ylidene ($^{B}NHC^{iPr}$), and 1,3-bis(2,6-diisopropylphenyl)imidazol-2-ylidene (NHC^{dipp}). Details for the syntheses of the NHC precursors are found in Section 3.8. Monolayers were prepared in UHV via thermal decomposition/sublimation of NHC–CO_2 precursors,[22] as illustrated in Figure 3.1 and described in Section 3.9. Briefly here, the precursors are placed in a Pyrex cell and connected to the pre-chamber through a leak valve. This cell is evacuated, heated to ~70 °C, and the carbene is introduced as a vapor into a pre-chamber containing a clean Au(111) crystal kept between −20 and −30 °C for ~5 min while maintaining a partial molecular pressure of 10^{-7} mbar. After deposition we confirm that the molecules deposited on the substrate have lost their CO_2 moieties, ostensibly through thermal decomposition, by measuring the O 1s spectrum of the layer using XPS.[22]

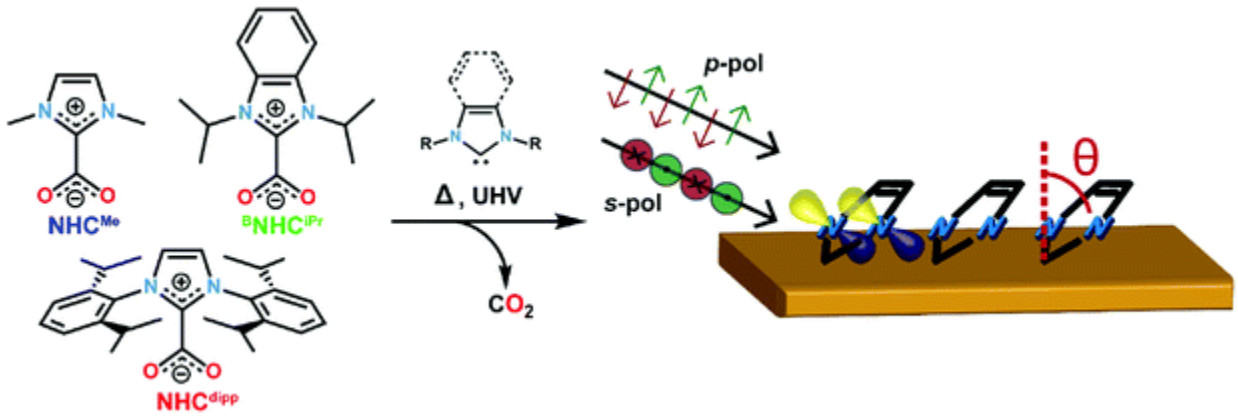

Figure 3. 22: Schematic showing the molecular structure of the NHC precursors, the thermal decomposition/sublimation deposition approach to create the NHC monolayers, and the NEXAFS dichroism measurement. Free NHC molecules are generated in the gas phase upon heating.

3.4 NEXAFS Studies

To determine the orientation of the NHC relative to the Au (111) surface normal (defined as the tilt angle θ in Figure 3.1), we first present NEXAFS linear dichroism results for each molecule.[33] Figure 3.2a shows the NEXAFS spectra collected at the N K-edge with the electric field of the incident photons perpendicular (p-polarization) and parallel (s-polarization) to the surface for NHC^{Me}, $^{B}NHC^{iPr}$, NHC^{dipp} monolayers. The key result is that the dependence of the NEXAFS spectra on the photon polarization (dichroism) varies with the carbene N-substituents.[33] The lowest energy NEXAFS resonance at ~401 eV arises from the N 1s → π*-LUMO (lowest unoccupied molecular orbital) transition. It is strongly enhanced with p-polarized photons for NHC^{Me}, moderately enhanced for $^{B}NHC^{iPr}$, and virtually absent for NHC^{dipp}; the opposite trend is observed for s-polarized photons. Since the π*-LUMO is delocalized over the whole imidazole ring for all three molecules, we can use the relative intensities of the ~401 eV NEXAFS p-polarized and s-polarized peaks to determine the average tilt angle θ for each carbene monolayer.[33] We find that NHC^{Me} is almost flat (θ ~ 72°), $^{B}NHC^{iPr}$ has an intermediate tilt angle (θ ~ 40°), and NHC^{dipp} is almost standing up (θ ~ 13°). The small tilt angle for NHC^{dipp} can be attributed to the steric bulk introduced by the side groups forcing the molecule to stand and preventing the NHC-ring from interacting directly with the surface. This is corroborated by the NHC^{dipp} NEXAFS spectra collected at the C K-edge (Figure 3.12).

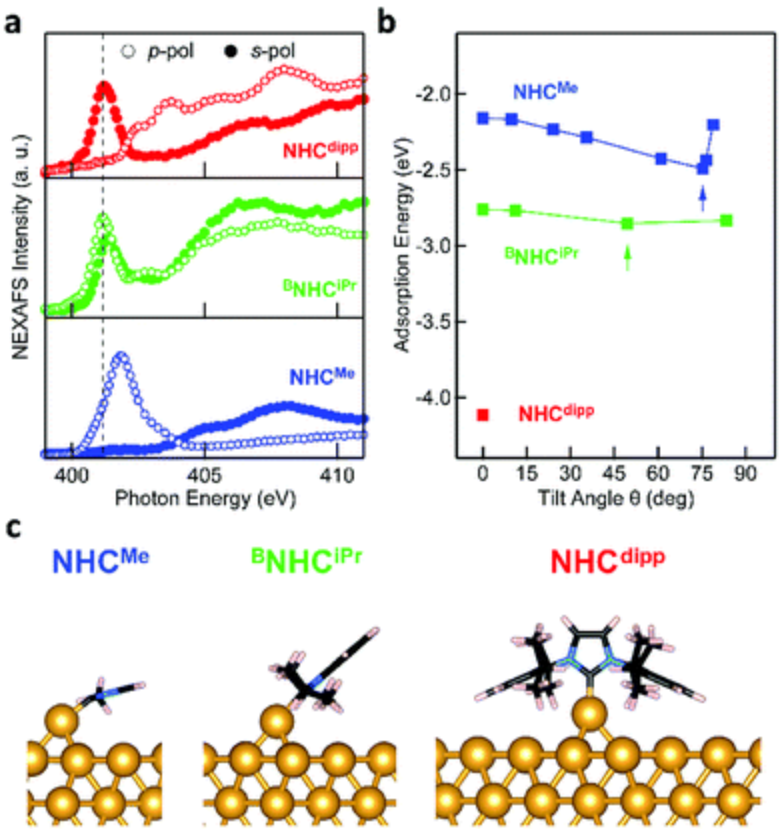

Figure 3. 23: a. NEXAFS spectra collected a the N K-edge for NHC^{Me} (blue, bottom panel), $^{B}NHC^{iPr}$ (green), and NHC^{dipp} (red) monolayers on Au(111). Each spectrum is measured using X-ray photons with incident electric field in a plane perpendicular to the surface (p-pol, empty circles) or in a plane parallel to the surface (s-pol, filled circles). The N 1s → π*-LUMO resonance (~401 eV, dashed black line) is significantly enhanced in p-pol for NHC^{Me}, and in s-pol for NHC^{dipp}, indicating a tilt angle θ ~ 72° and ~13° respectively. For $^{B}NHC^{iPr}$, both s- and p-pol spectra show the π*-LUMO resonance, yielding θ ~ 40°. **b.** Calculated adsorption energy of NHC^{Me} (blue) and $^{B}NHC^{iPr}$ (green) on an Au adatom as a function of θ. The adsorption energy of NHC^{dipp} (red) is calculated only for θ = 0°. The arrows indicate the lowest energy structure tilt angles, in good agreement with experimental observations. **c.** DFT-optimized energy minimum structure of a single NHC^{Me}, $^{B}NHC^{iPr}$ and NHC^{dipp} adsorbed on an Au adatom sitting on a hollow site of an Au(111) slab. These structures are consistent with the experimentally observed tilt angles.

It is remarkable that these variations in the tilt angle do not result in significant differences in the NHC monolayer stability as a function of temperature. Indeed, HR-XPS measurements show that NHC^{Me}, $^{B}NHC^{iPr}$ and NHC^{dipp} all come off the surface around ~300 °C either through desorption or decomposition (Figure 3.6). This implies that all three NHCs, despite their varied

orientations, form strong donor–acceptor bonds to Au. The van der Waals interactions alone are unlikely to result in high desorption temperatures for such small cyclic compounds.[34] The nature of the NHC–Au bond in these monolayers, and/or their macroscopic structure, is likely more complex than readily determined from the NEXAFS data alone. We therefore turn to DFT calculations to provide further insights.

3.5 Computational Investigation of Binding Geometry

We first consider two simple adsorption models for all three carbenes and use DFT calculations to evaluate their structure and bonding energy. We consider a single NHC molecule adsorbed either on a pristine Au(111) surface or an Au adatom sitting on a hollow site of the Au(111) surface. We will show later that this is not the structure that is consistent with our data for NHC^{Me}. Total energy and geometry optimization calculations, detailed in Section 3.11, are performed using Quantum ESPRESSO[35] with an exchange and correlation functional that accounts for van der Waals interactions.[36-37] A 4-layer Au(111) slab comprising 3 × 3, 4 × 3, and 5 × 5 surface unit cells is used to model surface-adsorbed NHC^{Me}, $^{B}NHC^{iPr}$ and NHC^{dipp}, respectively. The adsorption energy is defined as the difference between the energy of the combined system and the sum of the energies for each component separately. It is negative for bound systems.

The adsorption energy of NHC^{Me} in a constrained flat-lying geometry on an Au(111) slab is small (−0.91 eV). The carbene lone pair lies parallel to the Au slab and does not form a strong σ-bond to an Au atom (Figure 3.7). Removing the constraint on the tilt angle in this model results in NHC^{Me} adopting a binding geometry nearly normal to the Au(111) surface ($\theta \sim 15°$). This geometrical change is accompanied by a 0.58 eV increase of the adsorption energy of the molecule

(−1.49 eV; Figure 3.8). However, these results are at odds with the NEXAFS data indicating that θ ~ 72° for NHC^{Me}.

A significantly different outcome is obtained when the NHCs are relaxed on top of an Au adatom, as shown in Figure 3.2b. The adsorption energy for the NHCs at different tilt angles is calculated by constraining the geometry of the NHC ring relative to the surface normal. In its most stable conformation (Figure 3.2b and 3.2c), NHC^{Me} has a tilt angle θ ~ 75°, in excellent agreement with the NEXAFS data. The corresponding adsorption energy of −2.49 eV is 1 eV larger than when NHC^{Me} is bound to a flat Au(111) surface (Table 3.2). The maximum adsorption energy for $^{B}NHC^{iPr}$ is −2.85 eV (Table 3.2), corresponding to an optimized tilt angle θ ~ 50°. The adsorption energy for $^{B}NHC^{iPr}$, however, is only weakly dependent on θ, a consequence of the competition between steric repulsion imparted by the bulkier side substituents and the van der Waals interaction of the benzene ring towards the Au surface. The weak dichroism in the NEXAFS spectrum of $^{B}NHC^{iPr}$ (Figure 3.2a) agrees well with the theoretical results. The shallow energy minimum implies that there is no strong driving force to orient the molecule in a preferential geometry. Moreover, the computed lowest energy θ for $^{B}NHC^{iPr}$ is close to the theoretical angle at which no dichroism is expected (θ ~ 55°). Due to its bulkier N-substituents, NHC^{dipp} can only bind vertically, irrespective of the presence of an adatom (Figure 3.9). The adsorption energies for NHC^{dipp} bound to the Au(111) surface and to an Au adatom are −2.69 eV and −4.11 eV, respectively (Table 3.2).

For all three NHCs, the adsorption energy is larger when the molecule binds to an Au adatom. This is the result of the metal s- and d-orbitals being more accessible in the adatom resulting in a stronger donor–acceptor bond. This is reflected in the shorter NHC–Au bond length when the molecule is modeled on an Au adatom (see Table 3.1). However, among the three NHCs,

NHC^{dipp} stands out. The calculated adsorption energy for the adatom-bound model is significantly larger than the corresponding values for the other two NHCs. We attribute this difference to the van der Waals interactions of the dipp groups with the Au surface. The difference in adsorption energy between the pristine surface-bound and adatom-bound models is also significantly larger for the NHC^{dipp} system than for the other two NHCs. This can be explained by steric effects between the bulky dipp substituents and the surface, which significantly lengthen the NHC–Au bond (2.15 Å) and distort the molecule when NHC^{dipp} is bound to a pristine Au(111) surface. By contrast, when NHC^{dipp} is bound to an Au adatom, the dipp groups are further away from the surface, the carbenic carbon can get closer to the Au adatom (NHC–Au^{ad} bond length = 2.02 Å), and the molecule can relax to a less strained conformation. This is most easily seen looking at the orientation of the dipp groups. They are almost parallel to the surface in the perfect slab model (Figure 3.9) and close to the unstrained geometry in the adatom model (i.e. the C^{NHC}–N^{NHC}–C^{dipp} angle is ~124°; Figure 3.2c).

3.6 XPS Investigation of the NHC Bound Surface

The DFT calculations presented above suggest that NHCs bind significantly more strongly to an Au adatom than to a perfect Au(111) surface. XPS measurements can detect the presence of such adatoms on the surface. Figure 3.3a presents the N 1s core level XPS spectra of NHC^{Me}, $^{B}NHC^{iPr}$ and NHC^{dipp} monolayers. A single N 1s peak is observed in the NHC^{Me} and NHC^{dipp} spectra, consistent with only one type of N-containing species on the surface. The spectrum of $^{B}NHC^{iPr}$ shows two peaks. The first and more intense main peak is very close in energy to that of NHC^{dipp}. It is attributed to surface-bound $^{B}NHC^{iPr}$. The second, lower-energy peak is attributed to incipient

second-layer growth and/or a small amount of undissociated $^{B}NHC^{iPr}$–CO_2 adducts on the surface. Note that the NHC^{Me} N 1s peak (401.2 eV) is at a significantly higher binding energy than the corresponding peaks for the $^{B}NHC^{iPr}$ and NHC^{dipp} monolayers (~400.5 eV). The correlation between this shift and the positions of the NEXAFS N 1s → π*-LUMO resonance (Figure 3.2a) for these monolayers indicates that the latter is related to the N 1s core binding energy (an initial state effect). Such a shift to higher binding energy results from charge depletion at the N in the NHC^{Me} monolayer due to interaction of its π-electron system with the Au surface. This is consistent with the orientation of the molecule as determined by NEXAFS.

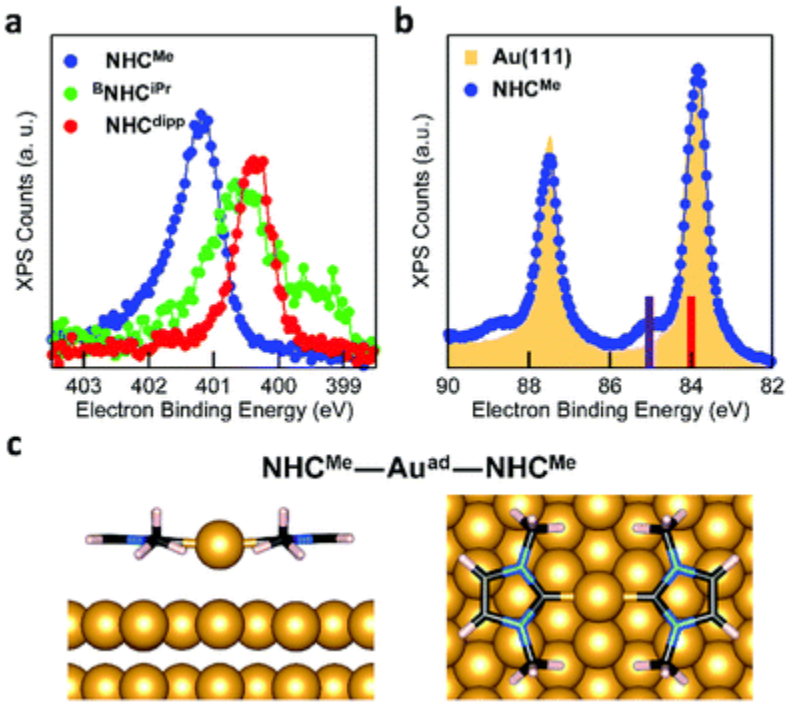

Figure 3. 24: a. XPS N 1s spectra of NHC^{Me} (blue), $^{B}NHC^{iPr}$ (green), and NHC^{dipp} (red) monolayers on Au(111). The NHC^{Me} N 1s peak is shifted to higher binding energy relative to both NHC^{dipp} and $^{B}NHC^{iPr}$. **b.** XPS Au $4f_{5/2,7/2}$ spectra of a clean Au(111) surface (yellow filled area) and the NHC^{Me} monolayer (blue) on the same Au(111) surface. The satellite peaks at ~1 eV higher binding energy are attributed to the presence of a high density of Au adatoms. Solid bars on the binding energy axis are the calculated XPS peak positions for bulk Au (red, 84.00 eV) and the Au adatom in the NHC^{Me}–Au^{ad}–NHC^{Me} complex (purple, 85.03 eV) adsorbed on the Au(111) slab. **c.** DFT-optimized energy minimum structure of the NHC^{Me}–Au^{ad}–NHC^{Me} complex adsorbed on a 4-layer Au(111) slab (only the upper two layers are shown). The NHC^{Me} rings are nearly coplanar to the surface and the adatom is on a hollow site.

Figure 3.3b compares the XPS spectra of the Au core level 4f spin–orbit doublet for a clean Au(111) surface and an NHC^{Me} monolayer grown on the same Au(111) surface.[38] The NHC^{Me} monolayer spectrum features a doublet of satellite peaks at higher binding energies. Fits of the Au $4f_{7/2}$ peak indicate that the new set of peaks is shifted by +1.1 eV with respect to the Au bulk component (Figure 3.10a). Two contributions can explain the difference in the binding energy of the Au 4f peak: (1) a chemical shift; or (2) a screening shift that both result for an Au atom that is

lifted significantly from the surface. Comparing the area under each peak, we find that 1/6 of the surface is covered by adatoms (Figure 3.10a).

To explore the origin of these satellite peaks, we consider two possible adsorption scenarios for NHC^{Me}: (1) the adsorption of a single NHC^{Me} on an Au adatom ($NHC^{Me}–Au^{ad}$), and (2) the formation of a flat-lying bis(NHC) complex with an Au adatom ($NHC^{Me}–Au^{ad}–NHC^{Me}$). We calculate the binding energy shift for the Au adatom 4f core level relative to the bulk (ΔE_{BE}) using the transition state model[39-40] of the excited system and the projector augmented-wave method implemented in the Vienna Ab initio Simulation Package (VASP).[41-42] Figure 3.3c presents the computed structure for the fully relaxed $NHC^{Me}–Au^{ad}–NHC^{Me}$ complex adsorbed on a 5 × 4 unit cell. For the complex, ΔE_{BE} = 0.91 eV, in good agreement with the experimental value (ΔE_{BE} = 1.1 eV). By contrast, the computed binding energy shift for $NHC^{Me}–Au^{ad}$ (ΔE_{BE} = 0.16 eV) is much smaller, suggesting that the satellite peaks in Figure 3.3b come from $NHC^{Me}–Au^{ad}–NHC^{Me}$ complexes on the surface. The formation of this bis(NHC) complex pulls the Au adatom away from the surface by more than 1 Å ($Au^{ad}–Au^{surf}$ distance is 2.06 and 3.09 Å for $NHC^{Me}–Au^{ad}$ and $NHC^{Me}–Au^{ad}–NHC^{Me}$, respectively). The change in the electron binding energy of the Au adatom, due to chemical shift and screening effects, is similar to what has been observed in thiol-based monolayers.[38]

As a comparison, the Au 4f XPS spectrum of the NHC^{dipp} monolayer shows no satellite peaks at higher binding energy. The bulky dipp groups prevent the formation of such bis(NHC) complexes (Figure 3.10b). A careful analysis of the STM images presented in a recent study[22] of NHC^{Me} monolayers on Au(111) further corroborate our conclusion that the molecules indeed form flat-lying $NHC^{Me}–Au^{ad}–NHC^{Me}$ complexes as opposed to $NHC^{Me}–Au^{ad}$ species oriented normal to

the surface, as originally proposed. To illustrate this point, Figure 3.11 compares an STM image simulated from our optimized structure and an experimental STM image reproduced from Wang et al.[22]

The behavior of $^{B}NHC^{iPr}$ differs from that of NHC^{Me} and NHC^{dipp}. This suggests a thermally activated process for the formation of the flat-lying bis(NHC) complexes. Figure 3.4a compares the N 1s XPS spectrum of a $^{B}NHC^{iPr}$ monolayer deposited at −20 °C with that of the monolayer annealed to 90 °C. The low-temperature monolayer shows a broad peak at ∼400.5 eV, indicating the formation of a mostly disordered surface structure (Figure 3.2a). Remarkably, the XPS peak shape and energy change significantly upon thermal annealing. The high temperature N 1s XPS peak is sharp and shifted to a higher binding energy (∼401.5 eV). This spectrum is similar to that observed for the NHC^{Me}–Au^{ad}–NHC^{Me} complexes (Figure 3.3a). The striking reorganization of the molecular layer is also captured in the NEXAFS dichroism collected at the N K-edge (Figure 3.4b). The N 1s → π*-LUMO resonance is greatly enhanced in p-polarized light, pointing to a nearly flat geometry for the annealed monolayer.

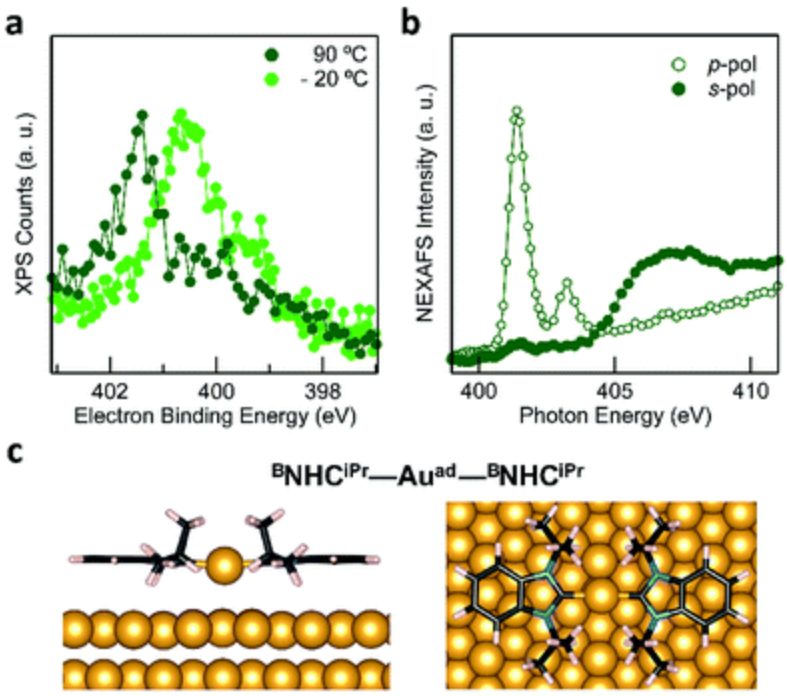

Figure 3. 25: a. XPS N 1s spectra of a $^{B}NHC^{iPr}$ monolayer deposited on a cold substrate at −20 °C (light green), and then annealed to 90 °C (dark green). The broad peak in the low-temperature spectrum comprises different components likely due to multiple molecular adsorption sites and/or of second-layer molecules. Thermal annealing generates a single sharp N 1s peak shifted to higher binding energy by ∼1 eV. **b.** NEXAFS spectrum collected at the N K-edge for the $^{B}NHC^{iPr}$ monolayer annealed to 90 °C: a strong dichroism is clearly visible. The N 1s → π*-LUMO resonance is strongly enhanced in p-pol indicating that the molecules lie nearly flat on the surface. **c.** DFT-optimized energy minimum structure of a $^{B}NHC^{iPr}$–Au^{ad}–$^{B}NHC^{iPr}$ complex adsorbed on an Au(111) 5 × 7 slab. Note that the adatom is above a hollow site on the Au(111) surface.

These spectroscopic changes make the adsorption behavior of $^{B}NHC^{iPr}$ at high temperature similar to that of NHC^{Me}. This prompted us to investigate theoretically the possibility that $^{B}NHC^{iPr}$ forms flat-lying bis(NHC) complexes, provided sufficient energy is available. Similar to its NHC^{Me} analogue, the modeled structure of the $^{B}NHC^{iPr}$–Au^{ad}–$^{B}NHC^{iPr}$ complex on an Au(111) slab (Figure 3.4c) shows that the Au adatom is pulled away from the surface by ∼1 Å (Table 3.1). While this should in principle also alter the Au 4f XPS spectra, we do not observe Au satellite peaks in Figure 3.10b. The lower surface density of $^{B}NHC^{iPr}$ accounts for this result. Using the intensity of the N

1s XPS peak, we estimate that the $^{B}NHC^{iPr}$ surface density at 90 °C is ~10 times lower than that of NHC^{Me} at −20 °C. At this implied density of Au adatoms, the shifted Au 4f XPS satellite would be undetectable. Two effects combine to explain the lower surface density: (1) the footprint of the flat-lying benzannulated $^{B}NHC^{iPr}$ is larger than that of NHC^{Me}; and (2) the elevated temperature for the measurement leads to a further decrease in the packing density.

3.7 Conclusion and Outlook

The strong carbene–Au interaction offers exciting opportunities as an alternative to the traditional thiol–Au bond, which suffers from limited chemical, electrochemical and thermal stability. By combining high-resolution X-ray photoelectron spectroscopy and computational modeling, this work reveals how adsorption energy, molecular orientation and metal surface structure are closely interconnected in a series of NHC monolayers. We find that NHCs bind significantly more strongly to an Au adatom than to a flat Au(111) surface. We show that with sufficient time and thermal energy, the molecule is capable of reorganizing the underlying gold surface structure. The orientation of the NHC on the surface is determined by the N-substituents. The smallest group – methyl – favors a planar geometry in which the NHC ring is parallel to the surface and organized into NHC^{Me}–Au^{ad}–NHC^{Me} complexes. Bulkier groups force the molecule into a more vertical orientation and prevent the formation of such flat-lying complexes. By thermally annealing the monolayer, we show it is possible to modulate the structure of surface-bound NHCs. Specifically, conversion from a single, vertically oriented NHC moiety to bis(NHC) complexes has been observed for $^{B}NHC^{iPr}$. While the initial orientation of NHCs on the surface appears to have little effect on the high thermal stability of NHCs SAMs, we expect that the

geometry and electronic structure of the surface-bound carbenes will ultimately prove critical in controlling their (electro)chemical stability, reactivity and functionality, through steric hindrance of reactive sites as well as the extent of intermolecular and molecule–surface interactions.

3.8 Synthetic Details

2-Iodopropane was purchased from Acros Organics. CD_2Cl_2, CD_3OD, and D_2O were purchased from Cambridge Isotope. Tetrahydrofuran (THF) was purchased from Fisher Scientific. 1,3-Bis(2,6-diisopropylphenyl)-1,3-dihydro-2H-imidazol-2-ylidene, 1H-benzimidazole and K_2CO_3 were purchased from Sigma-Aldrich. 1,3-Dimethylimidazolium chloride was purchased from TCI Chemicals. 1,3-Diisopropylbenzimidazolium iodide was synthesized following literature procedures.[43] All reactions were carried out under inert atmosphere in a N_2-filled glovebox, unless otherwise noted.

1,3-dimethylimidazolium-2-carboxylate (NHC^{Me}–CO_2)

In a N_2 filled glovebox, 1,3-dimethylimidazolium chloride (198 mg, 1.5 mmol) and potassium *tert*-butoxide (255 mg, 2.2 mmol) were suspended in 20 mL THF in a 20 mL scintillation vial. The suspension was stirred for 1 hour at room temperature and then filtered through a 0.2 μm PTFE syringe filter into a Schlenk flask equipped with a stir bar. The Schlenk flask containing the reaction mixture was sealed with a rubber septum. The flask was removed from the glove box and connected to a Schlenk line. CO_2 was bubbled through the solution for 30 min. The precipitated solid was collected via filtration through a medium porosity frit, washed with THF (3 x 20 mL), and dried *in vacuo*. NHC^{Me}–CO_2 was obtained as a white solid. (Yield: 110 mg, 53%). Spectroscopic characterization data matched with previous reported data.[44]

1,3-diisopropylbenzimidazolium-2-carboxylate ($^{B}NHC^{iPr}–CO_2$)

$^{B}NHC^{iPr}–CO_2$ was synthesized following the same procedure as $NHC^{Me}–CO_2$, starting from 1,3-diisopropylbenzimidazolium iodide (500 mg, 1.5 mmol). $^{B}NHC^{iPr}–CO_2$ was obtained as a white solid. (Yield: 167 mg, 45%). Spectroscopic characterization data matched with previous reported data.[45]

1,3-bis(2,6-diisopropylphenyl)imidazolium-2-carboxylate ($NHC^{dipp}–CO_2$)

$NHC^{dipp}–CO_2$ was synthesized following the same procedure as $NHC^{Me}–CO_2$, starting from 1,3-bis(2,6-diisopropylphenyl)-1,3-dihydro-2H-imidazol-2-ylidene (100 mg, 250 μmol) and omitting the initial deprotonation step. $NHC^{dipp}–CO_2$ was obtained as a white solid (Yield: 31 mg, 28%). Spectroscopic characterization data matched with previous reported data.[46]

3.9 NEXAFS Sample Preparation

The NHC monolayers were prepared and characterized *in situ* at the ALOISA beamline of the Elettra synchrotron light laboratory (Trieste, Italy). Monolayers were deposited in a preparation chamber (base pressure $< 2 \times 10^{-9}$ mbar) by first cleaning the Au(111) single crystal by repeated cycles of Ar^+ sputtering and thermal annealing to 800 K. Cleanliness was checked by ensuring no O, N, and C signal in XPS. The compounds were sublimed onto the Au(111) surface using a Pyrex cell connected to the preparation chamber through a leak valve. The cell was gently heated to ~70 °C for 4 - 5 minutes to keep a constant NHC pressure in the chamber of about 10^{-7} mbar. The substrate was kept at -20 to -30 °C to grow the monolayer phase. Measurements were carried out in an experimental chamber with base pressure $< 2 \times 10^{-10}$ mbar.

3.10 Details of XPS and NEXAFS Measurements

X-ray photoemission spectroscopy (XPS) measurements were performed at the ALOISA beamline with the x-ray beam at grazing incidence (4°) to the sample surface. Photoelectrons from the sample were collected at an emission angle normal to the surface using a hemispherical electron analyzer with an acceptance angle of 2°, and an overall energy resolution of ~0.2 eV. The energy scale for XPS spectra was calibrated by aligning the Au $4f_{7/2}$ peak to a binding energy of 84.00 eV.

Near edge X-ray absorption fine-structure (NEXAFS) measurements were performed on the N and C K-edge by sweeping the incident photon energy from 394 to 413 eV and from 278 to 310 eV, respectively. The photon incidence angle was set to 6°. Spectra were acquired using a Channeltron detector with a wide acceptance angle in the partial electron yield mode. The photon flux was monitored on the last optical element along the beam path. The sample normal was oriented either parallel (*p*-pol) or perpendicular (*s*-pol) to the light polarization.

The relative intensity of the nitrogen NEXAFS signal in *p*-pol and *s*-pol for the N 1s to LUMO transition was used for estimating the orientation of the carbene ring relative to the surface plane, whereas the orientation of the aryl groups for NHC^{dipp} was determined with the polarization-dependent signal of the C1s NEXAFS. The molecular tilt angle θ is estimated relative to the surface plane using the formula: $\tan(\theta) = \sqrt{2I_s/I_p}$, where I_s and I_p are the intensities of the π*-LUMO NEXAFS peak from the *s*-pol and *p*-pol spectra, respectively.[33]

3.11 Details of DFT Calculations

The PWSCF software in the Quantum Espresso package was used to simulate the adsorption of the NHCs on an Au(111) slab.[35] The "optB88-vdW" exchange and correlation functional was used for all calculations as it has been demonstrated to provide a good description of dispersion interactions. All structures were relaxed until interatomic forces in the self-consistent calculation were smaller than 0.026 eV/Å and energy variations smaller than 10^{-5} Ry. Adsorption relaxations were performed using an Au(111) 4-layer slab. The two bottom layers were held fixed while the top two ones were relaxed. The slab size was 3×3, 4×4 and 5×5 unit cells for NHC^{Me}, $^{B}NHC^{iPr}$, and NHC^{dipp}, respectively, whereas slabs of size 5×4 and 5×7 unit cells were used for the $NHC^{Me}–Au^{ad}–NHC^{Me}$ and $^{B}NHC^{iPr}–Au^{ad}–^{B}NHC^{iPr}$ complexes. The Au adatom was relaxed on a hollow position of the Au(111) surface slab prior to optimizing the adatom-adsorbed NHC systems. Convergence of the calculations relative to the cell size was also tested. The adsorption energies were calculated as follows by subtracting the sum of the energies of the separately relaxed molecule and slab systems from the total energy. All illustrations of ball-and-stick adsorption models were produced using VESTA 3 software.[35]

3.12 Additional Experimental and Theoretical Data

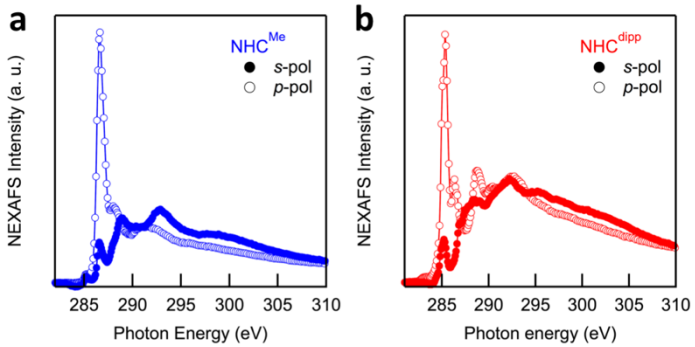

Figure 3. 26: NEXAFS spectra collected at the C K-edge of **a.** NHC^{Me} monolayer and **b.** NHC^{dipp} in *s*-pol (filled markers) and *p*-pol (empty markers). The first 1s to LUMO resonance corresponds to a π* orbital localized on the NHC ring (E_{photon} = 286.6 eV) in NHC^{Me} and to π* orbital localized on the aryl substituents (E_{photon} = 285.3 eV) in NHC^{dipp}. The second resonance in NHC^{dipp} is the π* orbital localized on the NHC ring (E_{photon} = 286.3 eV). Using the polarization-dependent data for NHC^{dipp}, we determine that the angle of the aryl substituent plane relative to the Au surface plane is ~29°.

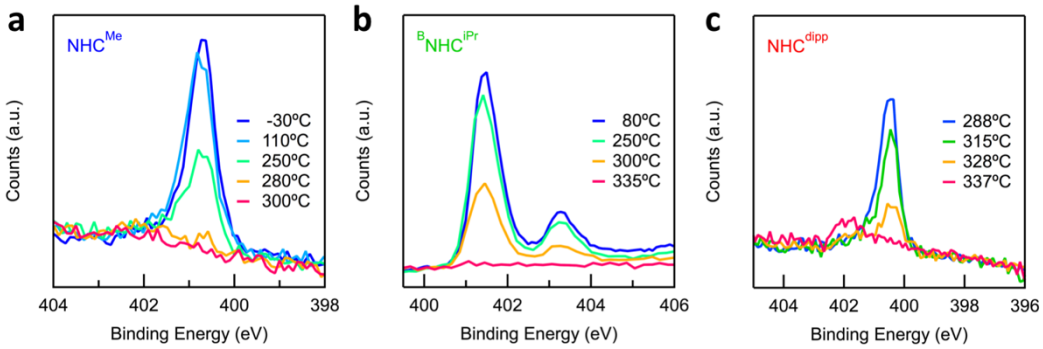

Figure 3. 27: N 1s XPS spectra collected at different temperatures for **a.** NHC^{Me}, **b.** $^{B}NHC^{iPr}$, and **c.** NHC^{dipp} monolayers. All NHCs exhibit similar desorption temperatures at ~280-330 ºC.

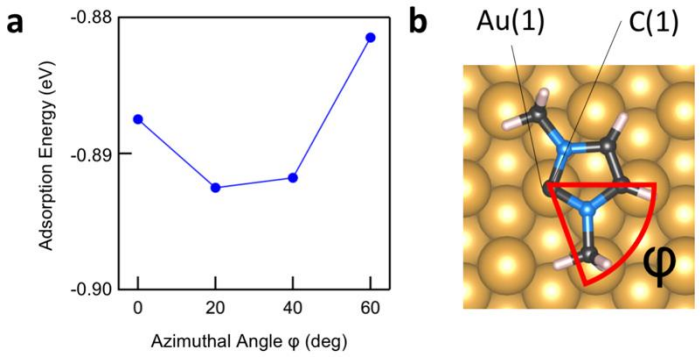

Figure 3. 28: a. Adsorption energy as a function of the azimuthal angle φ for NHC^{Me} adsorbed in a flat adsorption geometry on a 3×3 Au slab. NHC^{Me} carbenic carbon atom C(1) lies atop an Au(111) surface atom, Au(1). The angle of rotation of the molecule about the axis normal to the surface plane defined by C(1) and Au(1) and indicated by the arrow. The variation of adsorption energy as the molecule is rotated is ~0.01 eV. **b.** Modeled structure of NHC^{Me} on a 3×3 Au slab used to calculate the adsorption energy as a function of azimuthal angle.

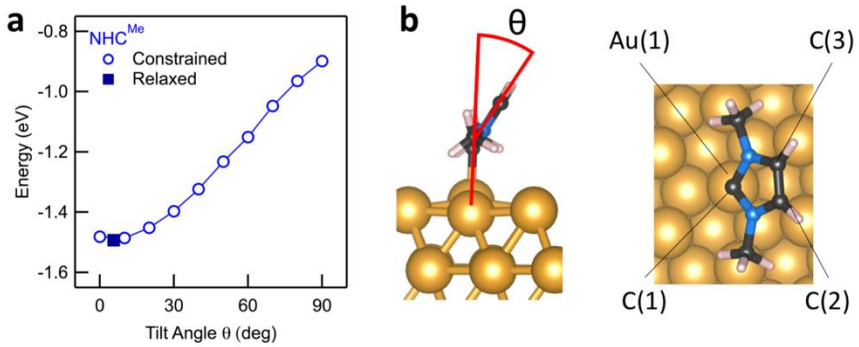

Figure 3. 29: a. Adsorption energy as a function of tilt angle θ for NHC^{Me} adsorbed on a 3×3 Au slab. The hollow blue circles are the adsorption energies calculated with two constraints: the angles defined by Au(1)-C(1)-C(2) and Au(1)-C(1)-C(3) are kept fixed during optimization. This ensures that θ remains fixed to a chosen value. A steep increase in adsorption energy is observed as θ increases. The solid square data point is obtained after lifting all constraints (starting from θ = 30º); the adsorption energy is –1.49 eV at θ ~15º. **b.** Modeled structure of NHC^{Me} on a 3×3 Au slab used to calculate the adsorption energy as a function of tilt angle.

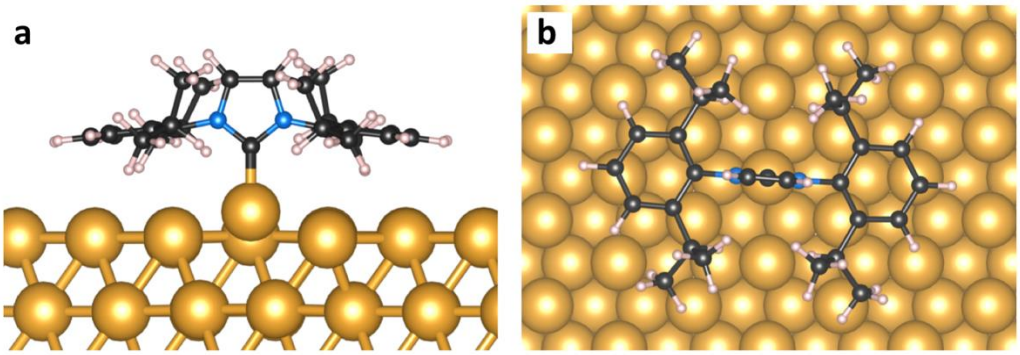

Figure 3. 30: DFT-optimized energy minimum structure of NHC^{dipp} on a 5×5 Au(111) slab. **a.** Side-view, and **b.** top-view. The carbene lone pair binds directionally to the slab Au atom pulling it out of the surface plane, while the large aryl substituents prevent the NHC ring from tilting towards the surface. The aryl substituents are bent upwards, displaying a nearly planar orientation relative to the surface plane (~7º).

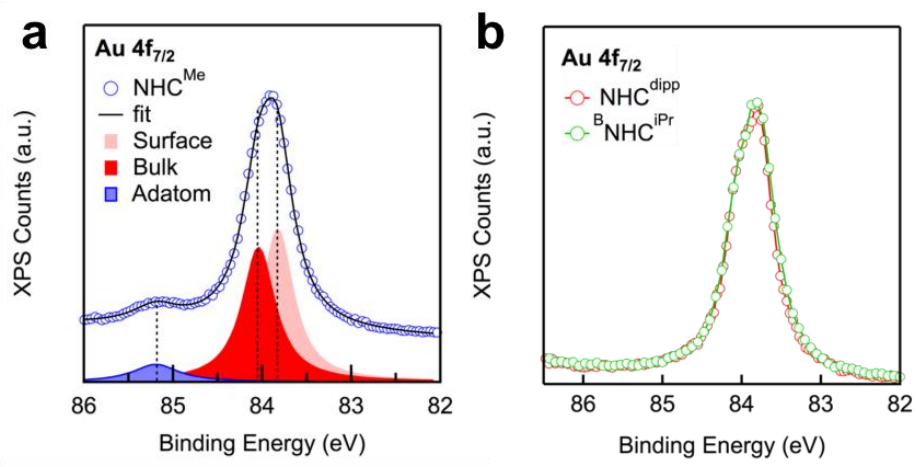

Figure 3. 31: a. Au $4f_{7/2}$ XPS spectrum (collected at 140 eV photon energy) for NHC^{Me} monolayer on Au(111). The XPS spectrum is fitted with three peaks using Voigt functions, corresponding to bulk (84.0 eV), surface, (83.8 eV) and adatom (85.1 eV) components. The FWHM of the surface and bulk components are set equal reported values (0.43 and 0.47 eV, respectively for bulk and surface components).[47-48] The FWHM of the adatom satellite was found to be 0.58 eV. A small linear background photoemission intensity was subtracted from the data. **b.** Au $4f_{7/2}$ XPS spectra (collected at 140 eV photon energy) for $^{B}NHC^{iPr}$ (at 90 °C) and NHC^{dipp} monolayers on Au(111). No satellite peak is observed.

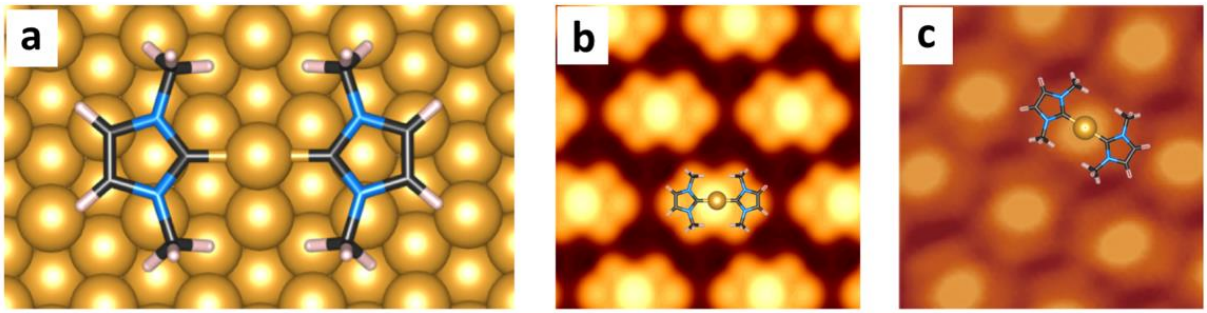

Figure 3. 32: a. DFT-optimized energy minimum structure of a NHC^{Me}–Au^{ad}–NHC^{Me} complex adsorbed on a 5×4 Au(111) slab. **b.** Simulated constant current STM image of the NHC^{Me}–Au^{ad}–NHC^{Me} complex adsorbed on a 5×4 Au(111) slab. The simulated image was obtained by integrating the density of states up to –0.45 eV from Fermi; an isovalue of 5×10^{-8} was used to plot the 2D map. The Au adatom appears as a very bright circular spot in the center of the complex due to its high density of states near Fermi. A ball-and-stick model of the complex is overlaid on the simulated image. **c.** Experimental STM image adapted from Figure 3b in Wang *et al.*[49] The image was recorded at –0.45 V substrate bias in constant current mode (I = 15 pA). A bright circular spot appears in the center of each twofold symmetric structure whose contour closely resembles that of the simulated STM image. A ball-and-stick model of the complex is overlaid on the image. The packing of the NHC^{Me}–Au^{ad}–NHC^{Me} complex on the surface observed in **c.** is not captured by the calculation presented in **b.** as this would require using a much larger unit cell beyond our capabilities.

Table 3.3: Selected atomic distances as calculated by DFT.

	Distance (Å)	
	Au^{ad}–C	Au^{ad}-surface
NHC^{Me}	2.072	2.178
$^{B}NHC^{iPr}$	2.061	2.143
NHC^{dipp}	2.042	2.183
NHC^{Me}–Au^{ad}–NHC^{Me}	2.055	3.088
$^{B}NHC^{iPr}$–Au^{ad}–$^{B}NHC^{iPr}$	2.069	3.094

Table 3.4: Calculated DFT adsorption energy.

	Adsorption energy (eV)	
	On surface	On adatom
NHC^{Me}	-1.49	-2.49
$^{B}NHC^{iPr}$	-2.14	-2.85
NHC^{dipp}	-2.69	-4.11
NHC^{Me}–Au^{ad}–NHC^{Me}	-2.48	

3.13 References

1. Crudden, C. M.; Horton, J. H.; Ebralidze, II; Zenkina, O. V.; McLean, A. B.; Drevniok, B.; She, Z.; Kraatz, H. B.; Mosey, N. J.; Seki, T.; Keske, E. C.; Leake, J. D.; Rousina-Webb, A.; Wu, G., Ultra stable self-assembled monolayers of N-heterocyclic carbenes on gold. *Nat. Chem.* **2014,** *6*, 409-414.

2. Crudden, C. M.; Horton, J. H.; Narouz, M. R.; Li, Z.; Smith, C. A.; Munro, K.; Baddeley, C. J.; Larrea, C. R.; Drevniok, B.; Thanabalasingam, B.; McLean, A. B.; Zenkina, O. V.; Ebralidze, II; She, Z.; Kraatz, H. B.; Mosey, N. J.; Saunders, L. N.; Yagi, A., Simple direct formation of self-assembled N-heterocyclic carbene monolayers on gold and their application in biosensing. *Nat. Commun.* **2016,** *7*, 12654.

3. Ling, X.; Roland, S.; Pileni, M. P., Supracrystals of N-Heterocyclic Carbene-Coated Au Nanocrystals. *Chemistry of Materials* **2015,** *27*, 414-423.

4. Ling, X.; Schaeffer, N.; Roland, S.; Pileni, M. P., Superior Oxygen Stability of N-Heterocyclic Carbene-Coated Au Nanocrystals: Comparison with Dodecanethiol. *Langmuir* **2015,** *31*, 12873-12882.

5. MacLeod, M. J.; Johnson, J. A., PEGylated N-Heterocyclic Carbene Anchors Designed To Stabilize Gold Nanoparticles in Biologically Relevant Media. *Journal of the American Chemical Society* **2015,** *137*, 7974-7977.

6. Roland, S.; Ling, X.; Pileni, M. P., N-Heterocyclic Carbene Ligands for Au Nanocrystal Stabilization and Three-Dimensional Self-Assembly. *Langmuir* **2016,** *32*, 7683-7696.

7. Zhukhovitskiy, A. V.; Mavros, M. G.; Van Voorhis, T.; Johnson, J. A., Addressable carbene anchors for gold surfaces. *J. Am. Chem. Soc.* **2013,** *135*, 7418-7421.

8. Weidner, T.; Baio, J. E.; Mundstock, A.; Grosse, C.; Karthauser, S.; Bruhn, C.; Siemeling, U., NHC-Based Self-Assembled Monolayers on Solid Gold Substrates. *Aust. J. Chem.* **2011,** *64*, 1177-1179.

9. Mata, J. A.; Poyatos, M.; Peris, E., Structural and catalytic properties of chelating bis- and tris-N-heterocyclic carbenes. *Coordination Chemistry Reviews* **2007,** *251*, 841-859.

10. Ranganath, K. V. S.; Onitsuka, S.; Kumar, A. K.; Inanaga, J., Recent progress of N-heterocyclic carbenes in heterogeneous catalysis. *Catalysis Science & Technology* **2013,** *3*, 2161-2181.

11. Man, R. W. Y.; Li, C. H.; MacLean, M. W. A.; Zenkina, O. V.; Zamora, M. T.; Saunders, L. N.; Rousina-Webb, A.; Nambo, M.; Crudden, C. M., Ultrastable Gold Nanoparticles Modified by Bidentate N-Heterocyclic Carbene Ligands. *Journal of the American Chemical Society* **2018,** *140*, 1576-1579.

12. Kim, H. K.; Hyla, A. S.; Winget, P.; Li, H.; Wyss, C. M.; Jordan, A. J.; Larrain, F. A.; Sadighi, J. P.; Fuentes-Hemandez, C.; Kippelen, B.; Bredas, J. L.; Barlow, S.; Marder, S. R., Reduction of the Work Function of Gold by N-Heterocyclic Carbenes. *Chemistry of Materials* **2017,** *29*, 3403-3411.

13. Arduengo, A. J.; Harlow, R. L.; Kline, M., A Stable Crystalline Carbene. *Journal of the American Chemical Society* **1991,** *113*, 361-363.

14. Diez-Gonzalez, S.; Marion, N.; Nolan, S. P., N-heterocyclic carbenes in late transition metal catalysis. *Chem. Rev.* **2009,** *109*, 3612-3676.

15. Enders, D.; Niemeier, O.; Henseler, A., Organocatalysis by N-heterocyclic carbenes. *Chem. Rev.* **2007,** *107*, 5606-5655.

16. Herrmann, W. A., N-heterocyclic carbenes: a new concept in organometallic catalysis. *Angewandte Chemie, International Edition* **2002,** *41*, 1290-1309.

17. Herrmann, W. A.; Elison, M.; Fischer, J.; Kocher, C.; Artus, G. R. J., Metal-Complexes of N-Heterocyclic Carbenes - a New Structural Principle for Catalysts in Homogeneous Catalysis. *Angewandte Chemie, International Edition in English* **1995,** *34*, 2371-2374.

18. Herrmann, W. A.; Elison, M.; Fischer, J.; Kocher, C.; Artus, G. R. J., N-heterocyclic carbenes([+]): Generation under mild conditions and formation of group 8-10 transition metal complexes relevant to catalysis. *Chemistry - a European Journal* **1996,** *2*, 772-780.

19. Herrmann, W. A.; Köcher, C., N-Heterocyclic Carbenes. *Angewandte Chemie, International Edition in English* **1997,** *36*, 2162-2187.

20. Marion, N.; Diez-Gonzalez, S.; Nolan, S. P., N-heterocyclic carbenes as organocatalysts. *Angew Chem Int Ed Engl* **2007,** *46*, 2988-3000.

21. Marion, N.; Nolan, S. P., N-heterocyclic carbenes in gold catalysis. *Chem Soc Rev* **2008,** *37*, 1776-1782.

22. Wang, G.; Ruhling, A.; Amirjalayer, S.; Knor, M.; Ernst, J. B.; Richter, C.; Gao, H. J.; Timmer, A.; Gao, H. Y.; Doltsinis, N. L.; Glorius, F.; Fuchs, H., Ballbot-type motion of N-heterocyclic carbenes on gold surfaces. *Nat. Chem.* **2017,** *9*, 152-156.

23. Doud, E. A.; Inkpen, M. S.; Lovat, G.; Montes, E.; Paley, D. W.; Steigerwald, M. L.; Vázquez, H.; Venkataraman, L.; Roy, X., In Situ Formation of N-Heterocyclic Carbene-Bound Single-Molecule Junctions. *Journal of the American Chemical Society* **2018,** *140*, 8944-8949.

24. Foti, G.; Vázquez, H., Tip-induced gating of molecular levels in carbene-based junctions. *Nanotechnology* **2016,** *27*, 125702.

25. Larrea, C. R.; Baddeley, C. J.; Narouz, M. R.; Mosey, N. J.; Horton, J. H.; Crudden, C. M., N-Heterocyclic Carbene Self-assembled Monolayers on Copper and Gold: Dramatic Effect of Wingtip Groups on Binding, Orientation and Assembly. *Chemphyschem* **2017,** *18*, 3536-3539.

26. Bakker, A.; Timmer, A.; Kolodzeiski, E.; Freitag, M.; Gao, H. Y.; Mönig, H.; Amirjalayer, S.; Glorius, F.; Fuchs, H., Elucidating the Binding Modes of N-Heterocyclic Carbenes on a Gold Surface. *Journal of the American Chemical Society* **2018,** *140*, 11889-11892.

27. Hurst, E. C.; Wilson, K.; Fairlamb, I. J. S.; Chechik, V., N-Heterocyclic carbene coated metal nanoparticles. *New Journal of Chemistry* **2009,** *33*, 1837-1840.

28. Richter, C.; Schaepe, K.; Glorius, F.; Ravoo, B. J., Tailor-made N-heterocyclic carbenes for nanoparticle stabilization. *Chem. Commun.* **2014,** *50*, 3204-3207.

29. Tang, Q.; Jiang, D. E., Comprehensive View of the Ligand Gold Interface from First Principles. *Chemistry of Materials* **2017,** *29*, 6908-6915.

30. Zhukhovitskiy, A. V.; MacLeod, M. J.; Johnson, J. A., Carbene Ligands in Surface Chemistry: From Stabilization of Discrete Elemental Allotropes to Modification of Nanoscale and Bulk Substrates. *Chem. Rev.* **2015,** *115*, 11503-11532.

31. Jiang, L.; Zhang, B.; Medard, G.; Seitsonen, A. P.; Haag, F.; Allegretti, F.; Reichert, J.; Kuster, B.; Barth, J. V.; Papageorgiou, A. C., N-Heterocyclic carbenes on close-packed coinage metal surfaces: bis-carbene metal adatom bonding scheme of monolayer films on Au, Ag and Cu. *Chem. Sci.* **2017,** *8*, 8301-8308.

32. Cossaro, A.; Mazzarello, R.; Rousseau, R.; Casalis, L.; Verdini, A.; Kohlmeyer, A.; Floreano, L.; Scandolo, S.; Morgante, A.; Klein, M. L.; Scoles, G., X-ray diffraction and computation yield the structure of alkanethiols on gold(111). *Science* **2008,** *321*, 943-946.

33. Stohr, J., *NEXAFS Spectroscopy*. Heidelberg: 1992.

34. Wetterer, S. M.; Lavrich, D. J.; Cummings, T.; Bernasek, S. L.; Scoles, G., Energetics and kinetics of the physisorption of hydrocarbons on Au(111). *Journal of Physical Chemistry B* **1998,** *102*, 9266-9275.

35. Giannozzi, P.; Baroni, S.; Bonini, N.; Calandra, M.; Car, R.; Cavazzoni, C.; Ceresoli, D.; Chiarotti, G. L.; Cococcioni, M.; Dabo, I., QUANTUM ESPRESSO: a modular and open-source software project for quantum simulations of materials. *Journal of Physics: Condensed Matter* **2009,** *21*, 395502.

36. Berland, K.; Cooper, V. R.; Lee, K.; Schroder, E.; Thonhauser, T.; Hyldgaard, P.; Lundqvist, B. I., van der Waals forces in density functional theory: a review of the vdW-DF method. *Rep. Prog. Phys.* **2015,** *78*, 066501.

37. Langreth, D. C.; Lundqvist, B. I.; Chakarova-Kack, S. D.; Cooper, V. R.; Dion, M.; Hyldgaard, P.; Kelkkanen, A.; Kleis, J.; Kong, L.; Li, S.; Moses, P. G.; Murray, E.; Puzder, A.; Rydberg, H.; Schroder, E.; Thonhauser, T., A density functional for sparse matter. *J Phys Condens Matter* **2009,** *21*, 084203.

38. Cossaro, A.; Floreano, L.; Verdini, A.; Casalis, L.; Morgante, A., Comment on "local methylthiolate adsorption geometry on au(111) from photoemission core-level shifts". *Phys. Rev. Lett.* **2009,** *103*, 119601; author reply 119602.

39. Goransson, C.; Olovsson, W.; Abrikosov, I. A., Numerical investigation of the validity of the Slater-Janak transition-state model in metallic systems. *Physical Review B* **2005,** *72*.

40. Janak, J. F., Proof that∂E∂ni=εin density-functional theory. *Physical Review B* **1978,** *18*, 7165-7168.

41. Kresse, G.; Furthmuller, J., Efficient Iterative Schemes for *Ab Initio* Total-Energy Calculations Using a Plane-Wave Basis Sset. *Physical Review B* **1996,** *54*, 11169.

42. Kresse, G.; Furthmuller, J., Efficiency of ab-initio total energy calculations for metals and semiconductors using a plane-wave basis set. *Computational Materials Science* **1996,** *6*, 15-50.

43. Han, Y.; Huynh, H. V.; Koh, L. L., Pd(II) complexes of a sterically bulky, benzannulated N-heterocyclic carbene and their catalytic activities in the Mizoroki–Heck reaction. *Journal of Organometallic Chemistry* **2007,** *692*, 3606-3613.

44. Holbrey, J. D.; Reichert, W. M.; Tkatchenko, I.; Bouajila, E.; Walter, O.; Tommasi, I.; Rogers, R. D., 1,3-Dimethylimidazolium-2-carboxylate: the unexpected synthesis of an ionic liquid precursor and carbene-CO2 adduct. *Chemical Communications* **2003**, 28-29.

45. DeJesus, J. F.; Trujillo, M. J.; Camden, J. P.; Jenkins, D. M., N-Heterocyclic Carbenes as a Robust Platform for Surface-Enhanced Raman Spectroscopy. *Journal of the American Chemical Society* **2018,** *140*, 1247-1250.

46. Wang, G.; Ruhling, A.; Amirjalayer, S.; Knor, M.; Ernst, J. B.; Richter, C.; Gao, H. J.; Timmer, A.; Gao, H. Y.; Doltsinis, N. L.; Glorius, F.; Fuchs, H., Ballbot-type motion of N-heterocyclic carbenes on gold surfaces. *Nat Chem* **2017,** *9*, 152-156.

47. Klimes, J.; Bowler, D. R.; Michaelides, A., Chemical accuracy for the van der Waals density functional. *Journal of Physics-Condensed Matter* **2010,** *22*.

48. Dion, M.; Rydberg, H.; Schroder, E.; Langreth, D. C.; Lundqvist, B. I., Van der waals density functional for general geometries (vol 92, art no 246401, 2004). *Physical Review Letters* **2005,** *95*.

49. Momma, K.; Izumi, F., VESTA 3 for three-dimensional visualization of crystal, volumetric and morphology data. *Journal of Applied Crystallography* **2011,** *44*, 1272-1276.

Chapter 4: NHCs as Superatomic Ligands

4.1 Preface

This chapter details some of the exploratory investigations I have performed on the synthesis of NHC-ligated superatoms. This work is ongoing and by no means complete, however the foundations for several interesting avenues of research are presented in this chapter. The results described below consist mostly of synthetic details and crude crystal structures that still require full refinement, have incomplete data, or too low quality of data for full refinement.

4.2 Introduction

As was shown in Chapter 1, the structure and composition of the ligand shell of a superatom provides both functionality and access to the core. Careful consideration of the ligand shell is necessary when selecting a superatom for use in the synthesis of a new material. Chapters 2 and 3 introduced NHCs as a potential ligand for superatoms, demonstrating attractive materials properties as well as how they interact with surfaces. Further, the development of novel superatomic materials will require not only new methods of assembly but also of accessing the chemically rich core. I sought to utilize a family of NHC based ligands to synthesize superatoms which could be assembled in ways previously unexplored and may provide more facile access to the superatomic core.

There are several examples of NHC ligated molecular cluster or superatom syntheses. Previous work in our group by Dr. Bonnie Choi[1] utilized NHCs as a capping ligand for a series of MnTe superatoms is one such example. Another is the use of selective ligand exchange in a series

of site-differentiated Re_6Se_8 superatoms.[2] However, in these examples as well as others,[3-4] these NHC ligands serve only as capping or passivating ligands and with little or no further functionality. In the few instances where these NHC ligands have been synthesized with further functionality, they have been shown to be very robust and to exhibit properties useful to materials scientists.[3] The lack of exploration in this area is surprising, considering the well-known syntheses of NHC ligands and their highly functionalizable nature.

As shown in Chapter 2, NHC containing molecules can form single molecule junctions and exhibit attractive conductance properties.[5] Theoretical calculations performed on the NHC containing linkers in Chapter 2 also demonstrated that there is strong electronic coupling in the M – NHC contact. The properties NHC's exhibit in a single molecule junction as well as their potential for functionaliztion, suggests that they should be investigated as superatomic ligands. The conductance and strong electronic coupling could likely provide access to the superatomic core that traditional phosphine ligands do not allow while the functionalization of the NHC backbone could enable new methods of assembly for use in superatomic materials.

4.3 Selection of NHC Ligands and NHC Library

To investigate NHCs as potential superatomic ligands, there were two factors to consider when selecting a particular NHC as a starting point. First, the benzimidazolium-based NHC family was chosen over the well-studied imidazolium family. The benzimidazolium family was chosen due to the highly tunable nature of the benzimidazole backbone and the ease with which it could be modified with redox active group.[6-7] The second factor to consider was which R-groups of the N-substituents would be ideal for binding to a superatom. Although NHCs are used in number of

organometallic complexes, the majority of these complexes utilize NHCs in which there are sterically demanding aryl groups as the N-substituents. The large buried volume[8] of NHCs containing these substituents could make binding to superatoms containing first row transition metals difficult. Additionally, Chapter 3 describes how NHCs with aryl substituents bind rigidly to surfaces which could translate to less stable binding for superatoms as well. However, small alkyl groups like methyl- or ethyl- may not provide adequate protection to the M – NHC bond and benzimidazole-based NHCs with these substituents often undergo dimerization as the free carbene, complicating synthesis.[9] For these reasons, the isopropyl group was chosen as the primary N-substituent to be used. With these two factors in mind, 1,3-diisopropylbenzimidazol-2-ylidene (**D^{i}PrBI**, Figure 4.1a) was chosen as the starting NHC ligand.

The highly tunable nature of the benzimidazole backbone allows for NHCs that contain functional groups not present in typical imidazole-based NHC ligands. To explore this functionality, NHCs containing a redox-active quinone group, 1,3-diisopropyl-4,5-napthoquino-imidazol-2-ylidene[6] (**D^{i}PrNQI**, Figure 4.1b), or a functionalizable aryl-bromide, 1,3-diisopropyl-6-bromo-benzimidazol-2-ylidene (**6Br-D^{i}PrBI**, Figure 4.1c), were synthesized, as their hydrobromide or hydroiodide salts, respectively. To explore the effects of steric bulk of the N-substituents on the ability for NHCs to act as ligands for superatoms, dibenzyl- (**DBnBI**, Figure 4.1d) and dineopentyl- (**D^{neo}PBI**, Figure 4.1e) N-substituted NHCs were synthesized as well, as their hydrobromide or hydrochloride salts respectively.

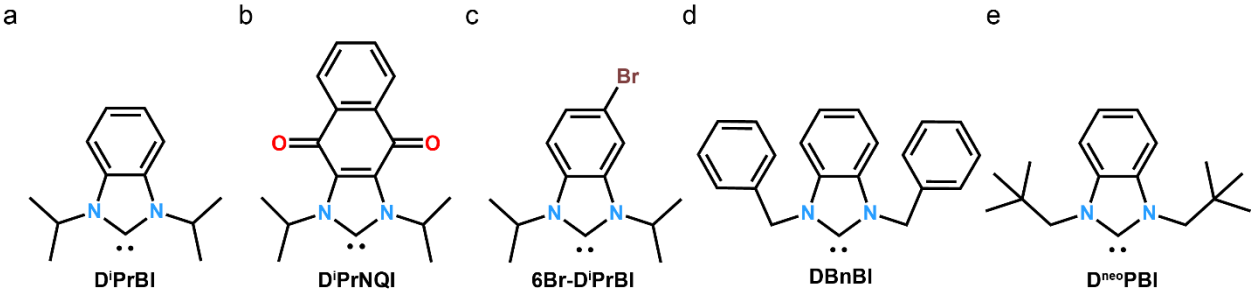

Figure 4.1: **a-e.** Structures of the NHCs used in this study.

4.4 Synthetic Strategy

With a potential library of NHCs chosen to act as ligands, a method of installation of the NHC ligands was necessary. Two methods were considered; directly synthesizing superatoms with NHC ligands and ligand exchange reactions. Following previously published procedures or slight modifications thereof[1], attempts to synthesize superatoms with **D^{i}PrBI** directly were unsuccessful. Instead, two methods of ligand exchange were investigated; either performing the exchange in solution using the $Co_6S_8(PPh_3)_6$ superatom in the presence of excess ligand[10] or photochemically using the carbonyl site-differentiated $Co_6Se_8(PEt_3)_{6-x}(CO)_x$ (x = 1 or 2) superatom.[11]

Equipped with the ligand exchange strategies and the NHC library described above, I began to explore the synthesis of superatoms with functional NHC ligands. Unfortunately, this work is very much incomplete with the majority of results being determined solely through crude SCXRD structures. However, I believe that this work is significant in that it provides potential avenues for future investigation as well as reveals unusual reactivity of the superatoms.

4.5 $Co_6S_8(PPh_3)_6$ Ligand Exchange Experiments

Previous work[10] in our lab demonstrated that the PPh_3 ligands of the $Co_6S_8(PPh_3)_6$ superatom could be exchanged with PEt_3 ligands cleanly and with relative ease. I applied this same methodology using **D^{i}PrBI** in an attempt to install NHC ligands. Heating a THF solution of $Co_6S_8(PPh_3)_6$ with 6 equivalents of **D^{i}PrBI** for 48 hrs however did not yield NHC ligated superatom. The only products isolated out of the reaction were $Co_6S_8(PPh_3)_6$, **D^{i}PrBI** salts, or amorphous powders.

The same reaction was also attempted with excess **D^{i}PrNQI** ligand. Once again, the majority of products were $Co_6S_8(PPh_3)_6$ and **D^{i}PrNQI** salts, however SCXRD analysis of some isolated crystals revealed a successful ligand exchange of two PPh_3 ligands with **D^{i}PrNQI** with the two NHCs being in the *trans*- position to yield *trans*-$Co_6S_8(PPh_3)_4$(**D^{i}PrNQI**)$_2$. Unfortunately, the highly symmetric spacegroup (I4/m) of the crystal as well as the low quality of the crystals themselves prevented full refinement of the NHC ligand. Interestingly the packing of the superatoms within the crystal lattice indicates that there is some form of interaction between the **D^{i}PrNQI** ligands, as shown in Figure 4.2, which results in an infinite 1D chain-like packing along the *c* axis. From the available data, the nature of this interaction cannot be determined. It is possible that there is simply a π–π stacking interaction between the aromatic systems of the ligands. There is also a possibility that the quinone moieties of the ligands were reduced by the electron rich superatom, resulting in a more complex ligand interaction. Frustratingly, this result has very low reproducibility and conditions to synthesize the *trans*-$Co_6S_8(PPh_3)_4$(**D^{i}PrNQI**)$_2$ superatom reliably have not been determined, making full characterization of the product impossible.

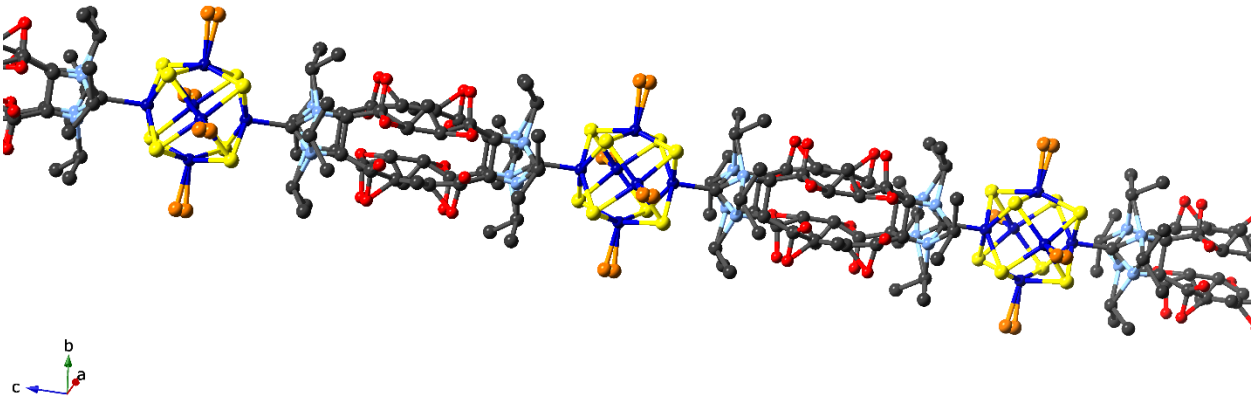

Figure 4.2: Infinite 1D chain-like packing of the *trans*- $Co_6S_8(PPh_3)_4$(**D^{i}PrNQI**)$_2$ superatom along the *c* axis. High symmetry, high disorder, and low quality data prevent full refinement, R_1 = 12.45% for the structure. Phenyl rings of the PPh_3 ligands and hydrogen atoms have been omitted for clarity. Color code: Co: blue; P: orange; S: yellow; N: light blue; C: black; O: red.

4.6 Ligand Exchange Using Site-differentiated $Co_6Se_8(PEt_3)_{6-x}(CO)_x$ (x = 1 or 2) Superatoms

Inspired by the work of Dr. Anouck Champsaur of the Nuckolls Lab[11] with the site-differentiated $Co_6Se_8(PEt_3)_{6-x}(CO)_x$ (x = 1 or 2) superatoms and difficulty in reliably synthesizing the *trans*-**D^{i}PrNQI** substituted $Co_6S_8(PPh_3)_6$ superatoms resulted in a shift in focus to the photochemical ligand exchange strategy. Seeking to mimic the results obtained using the $Co_6S_8(PPh_3)_6$ superatoms, *trans*-$Co_6Se_8(PEt_3)_4$(**D^{i}PrNQI**)$_2$ was the initial target using this method. Briefly, a solution of the *trans*-substituted $Co_6Se_8(PEt_3)_4(CO)_2$ superatom and a slight excess of the **D^{i}PrNQI** ligand in THF in a quartz round bottom flask was irradiated overnight or until the FT-IR spectrum indicated no $Co_6Se_8(PEt_3)_4(CO)_2$ remaining in the reaction mixture. After filtering and inducing crystallization via slow diffusion of a hexanes layer, again a mixture of products was obtained.

From this mixture of products, crystals were isolated which SCXRD analysis revealed the ligand exchange was successful. Unlike in the $Co_6S_8(PPh_3)_6$ experiment, the data was of high enough quality that the **D^{i}PrNQI** ligands could be fully refined, Figure 4.3a. Again, the structure exhibits the interesting 1D chain-like packing along the *c* axis, Figure 4.3b, and measuring the centroid to centroid distances of the **D^{i}PrNQI** rings returns a separation of 3.33 Å, well within what would be considered a π–π stacking interaction. Like in the above $Co_6S_8(PPh_3)_6$ example, there was difficulty in reliably reproducing the *trans*-substituted product. Thus, characterization beyond SCXRD analysis could not be performed.

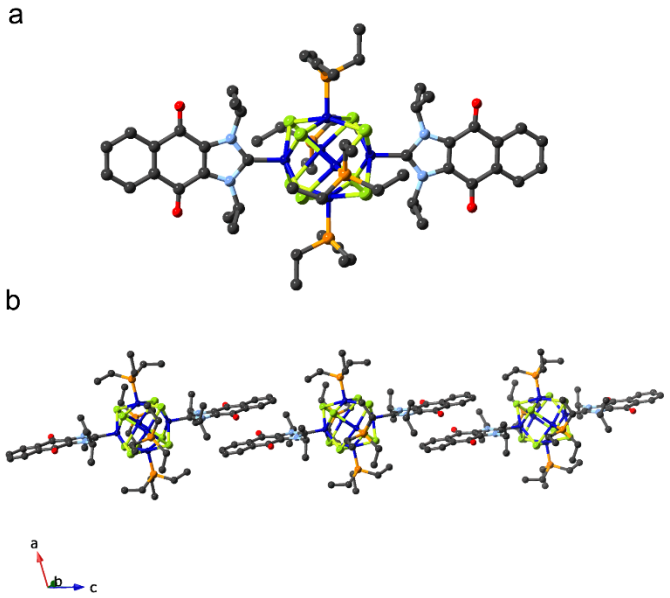

Figure 4.3: a. Structure of *trans*-$Co_6Se_8(PEt_3)_4$(**D^{i}PrNQI**)$_2$ obtained from SCXRD. **b.** Infinite 1D chain-like packing of the *trans*-$Co_6Se_8(PEt_3)_4$(**D^{i}PrNQI**)$_2$ superatom along the *c* axis. These structures are from crude SCXRD data that still requires complete refinement, R_1 = 9.43%. Hydrogen atoms removed for clarity. Color code: Se: green; Co: blue; P: orange; N: light blue; C: black; O: red.

Frustrated by the inability to reliably reproduce the synthesis of *trans*-$Co_6Se_8(PEt_3)_4$(**D^{i}PrNQI**)$_2$, I re-evaluated the synthetic strategy employed in the ligand

exchanges. I chose to return to the use of as a ligand and to focus on only the mono-substituted $Co_6Se_8(PEt_3)_5(CO)$ superatom to reduce the complexity of the system and to determine how to reliably perform the ligand exchange. I also began to use Ag(I) halide complexes of the NHC ligands as carbene transfer reagents in the experiments.[12] This change eliminated the need to produce the free carbene, further simplifying the reaction conditions.

With the above changes to the synthetic strategy, I attempted the ligand exchange reaction with $Co_6Se_8(PEt_3)_5$(**D^{i}PrBI**) as the new target. A solution of the mono-substituted $Co_6Se_8(PEt_3)_5(CO)$ superatom and a slight excess of the **D^{i}PrBI**-Ag(I)I ligand in THF was irradiated overnight or until the FT-IR spectrum indicated no $Co_6Se_8(PEt_3)_5(CO)$ remaining in the reaction mixture. Upon crystallization after work-up, a rather surprising product was identified. Instead of producing $Co_6Se_8(PEt_3)_5$(**D^{i}PrBI**) as expected, the open-open faced superatom $[Co_5Se_8(PEt_3)_5]_2[Ag_2I_4]$ was obtained, nearly the opposite of what was expected. From the crude SCXRD structure given in Figure 4.4a, one cobalt atom has been removed from the superatom core, causing a severe deformation of the core and the formation of what appears to be diselenide-like bonds within the core. While this structure was extremely interesting, this was yet again not the desired target and difficulty in purifying the product prevented complete characterization beyond SCXRD analysis.

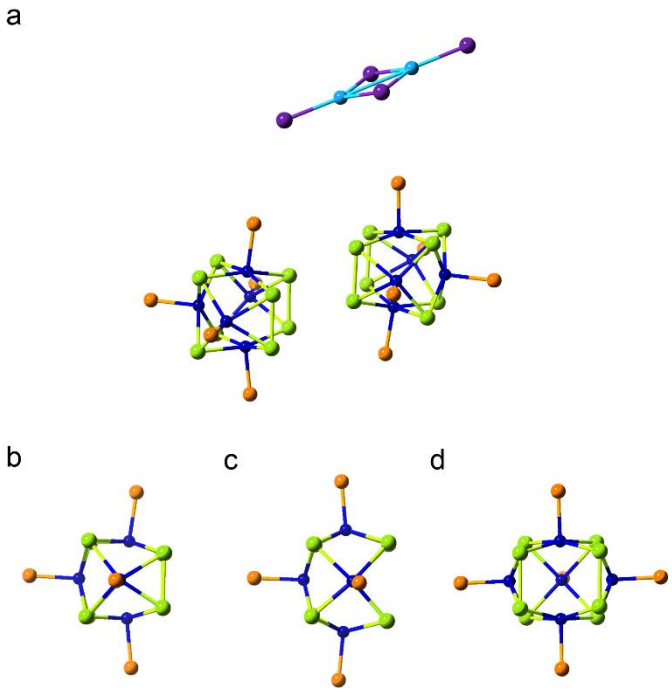

Figure 4.5: a. Structure of $[Co_5Se_8(PEt_3)_5]_2[Ag_2I_4]$ obtained from SCXRD. **b-d.** Views of different faces of one of the $[Co_5Se_8(PEt_3)_5]^+$ clusters, highlighting the deformation of the core and the formation of what appears to be two diselenide bonds. This structure is from crude SCXRD data that may be of too poor of quality for complete refinement, R1 = 10.47%. Ethyl groups of PEt_3 ligands and toluene solvent molecules removed for clarity Color code: I: purple; Ag: teal; Se: green; Co: blue; P: orange.

4.7 Ligand Exchange Using the Oxidized $[Co_6Se_8(PEt_3)_{6-x}(CO)_x][PF_6]$ (x = 1 or 2)

Although the desired product was obtained in some of the above examples, the irreproducibility and difficulty in purifying the products presented a major challenge to developing a method of synthesizing superatoms with NHC ligands. Turning to the one literature example of a successful NHC ligand exchange on a superatom[2], we see that a positively charged, electron-poor superatom was used. Following this example, I began to investigate the use of the oxidized superatoms, $[Co_6Se_8(PEt_3)_{6-x}(CO)_x][PF_6]$ (x = 1 or 2), in the ligand exchange reactions.

Using the same conditions that yielded the open cluster described above except using the oxidized $[Co_6Se_8(PEt_3)_5(CO)][PF_6]$ superatom, the ligand exchange reaction was repeated. After 6hrs I observed almost complete disappearance of the starting material, much faster than any of the previous reaction. Upon work-up and crystallization, the only major products recovered were crystals of **D^{i}PrBI** salts and the desired $[Co_6Se_8(PEt_3)_5$(**D^{i}PrBI**)$][PF_6]$ superatom. Fortunately, the exchanged product was slightly soluble in toluene, so it could be separated from the salts of **D^{i}PrBI** relatively easily, allowing for ^{1}H and ^{31}P NMR characterization. High quality crystals could also be grown from diffusion of an ether layer into a THF solultion of the superatom. The structure of $[Co_6Se_8(PEt_3)_5$(**D^{i}PrBI**)$][PF_6]$ as determined by SCXRD is given in Figure 4.6a. From the structure, we see that the Co – C_{NHC} bond distance is ~1.91 Å, which is significantly shorter than the other reported M – C_{NHC} bonds in other NHC ligated superatoms[1-2] which could indicate a greater degree of electronic coupling of the core to the NHC ligand.

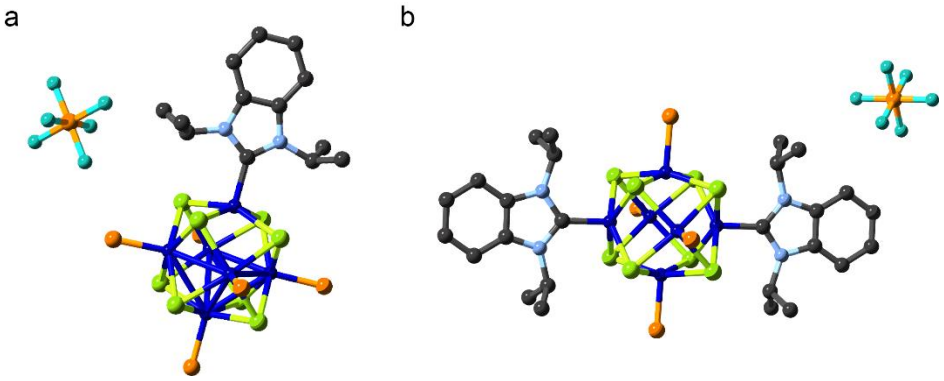

Figure 4.6: a. Crude structure of $[Co_6Se_8(PEt_3)_5$(**D^{i}PrBI**)$][PF_6]$ obtained from SCXRD data, R = 9.75% without complete refinement. **b.** Crude structure of *trans*-$[Co_6Se_8(PEt_3)_4$(**D^{i}PrBI**$)_2][PF_6]$ obtained from SCXRD data, R = 7.35% without complete refinement. Ethyl groups of PEt_3 ligands, solvent molecules, and hydrogen atoms omitted for clarity. Color code: Se: green; Co: blue; P: orange; N: light blue; C: black; F: aqua.

The ligand exchange reaction was also performed using the oxidized *trans*-$[Co_6Se_8(PEt_3)_4(CO)_2][PF_6]$ and again, the reaction proceeded quickly and produced the expected *trans*-$[Co_6Se_8(PEt_3)_4(\mathbf{D^iPrBI})_2][PF_6]$ along with excess **D^{i}PrBI** salts. Again, fairly high-quality crystals could be obtained and a crude crystal structure was obtained, as shown in Figure 4.6b. The Co – C_{NHC} bond distance is ~1.89 Å, which is even shorter than the distance for $[Co_6Se_8(PEt_3)_5(\mathbf{D^iPrBI})][PF_6]$, also suggesting some degree of electronic coupling to the superatom core.

Encouraged by these results, the next step was to increase the complexity of the ligand and attempt to install the **6Br-D^{i}PrBI** ligand which contains an aryl bromide moiety, an extremely versatile functionality used in a number of synthetic transformations. Exchange reactions with $[Co_6Se_8(PEt_3)_5(CO)][PF_6]$ and **6Br-D^{i}PrBI**-AgI behave as expected and the reaction is complete within several hours. Work-up followed by crystallization yields the $[Co_6Se_8(PEt_3)_5(\mathbf{6Br\text{-}D^iPrBI})][PF_6]$ and excess **6Br-D^{i}PrBI** salts. The structure of $[Co_6Se_8(PEt_3)_5(\mathbf{6Br\text{-}D^iPrBI})][PF_6]$ is given in Figure 4.7a. Surprisingly, attempts to purify the product and remove excess **6Br-D^{i}PrBI** salts were successful when silica-gel column chromatography with a 90:9:1 DCM:Acetone:MeOH solvent mixture was used. Further, the ionic product can easily be reduced with cobaltocene to yield the neutral $Co_6Se_8(PEt_3)_5$(**6Br-D^{i}PrBI**). As stated previously, the installation of an aryl bromide is extremely exciting as this opens the door for functionalization that is not common in superatomic ligands.

4.8 Attempts at Functionalization of $Co_6Se_8(PEt_3)_5$(6Br-D^{i}PrBI)

With a versatile synthetic handle now easily installable onto a superatom via ligand exchange, I began to explore potential useful synthetic transformations. The Pd-catalyzed Miyaura borylation was initially chosen as a target transformation due to how common this reaction is utilized in synthetic chemistry, especially for use in Suzuki couplings. Using common borylation conditions[13], I attempted to install a boronic pinacol ester onto the benzimidazole backbone of the **6Br-D^{i}PrBI** NHC ligand. Work up of the reaction followed by ^{1}H NMR analysis of the product, revealed that the borylation was unsuccessful and that instead the $Co_6Se_8(PEt_3)_5$(**6Br-D^{i}PrBI**) starting material had been re-oxidized. The source of this oxidation is unknown, however the catalyst used in the reaction was $PdCl_2$(dppf) and the presence of the ferrocene containing dppf ligand could have played a role. Although this attempt at borylation was unsuccessful, this is an interesting challenge that should be explored in the future, with careful attention paid to the conditions of the reaction.

Again, inspired by previous work done by Dr. Anouck Champsaur[14], the installation of a boronic acid functionality was explored using the $Co_6Se_8(PEt_3)_5$(**6Br-D^{i}PrBI**) superatom. Also ubiquitous in the Suzuki coupling reaction, aryl boronic acids are readily formed using alkyl lithium reagents and an alkyl borate. Lithiation of the $Co_6Se_8(PEt_3)_5$(**6Br-D^{i}PrBI**) superatom using nBuLi at -78°C followed by the addition of tri-isopropylborate, acidic work up, and crystallization resulted in the isolation of a very small amount of plate-like crystals. SCXRD analysis of these crystals proved to be difficult due to their size and the data collected was very low quality, however the very crude solutions obtained do suggest that boronic acid formation was successful, as shown in Figure 4.7b. This was extremely promising and this procedure

should be repeated on a much larger scale so that the product can be fully characterized and used in Suzuki coupling reactions.

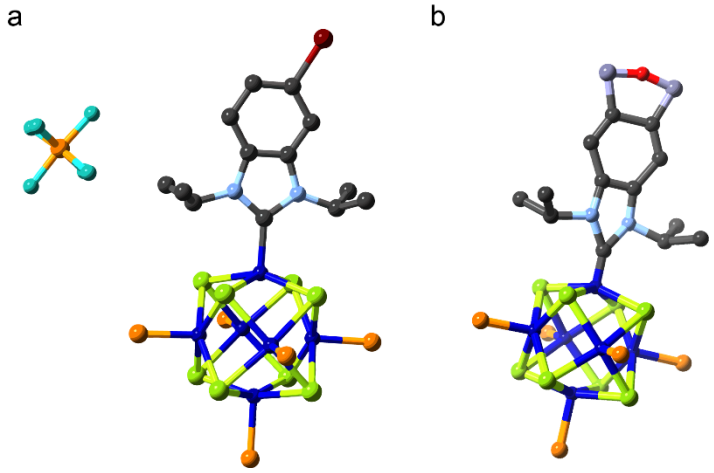

Figure 4.7: a. Crude structure of $[Co_6Se_8(PEt_3)_5(\mathbf{6Br\text{-}D^iPrBI})][PF_6]$ obtained from SCXRD data, R = 4.74% without complete refinement. **b.** Crude structure obtained from SCXRD analysis of crystals isolated from the boronic acid formation reaction using $Co_6Se_8(PEt_3)_5(\mathbf{6Br\text{-}D^iPrBI})$, R = 17.15% without complete refinement, suggesting that boronic acid formation was succesful. Ethyl groups of PEt_3 ligands, solvent molecules, and hydrogen atoms omitted for clarity. Color code: Se: green; Co: blue; Br: maroon; P: orange; B: lavender; N: light blue; C: black; O: red; F: aqua.

4.9 Effects of Bulky N-substituents

As demonstrated above, di-isopropyl substituted NHCs readily bind to the superatomic core, but was there indeed a limit to the size of N-substituents that could bind to the superatoms? I began to investigate this question using the di-benzylic- and di-neopentyl- substituted NHCs, **DBnBI** and **D^{neo}PBI** respectively (Figure 4.1d and e).

Using a similar procedure for the exchange of $[Co_6Se_8(PEt_3)_5(CO)][PF_6]$ and using **DBnBI**-AgBr, $[Co_6Se_8(PEt_3)_5(\mathbf{DBnBI})][PF_6]$ was readily obtained, crude structure given in Figure 4.8a. From the structure obtained, we see that the benzylic N-substituents preferentially

orient on the same side of the NHC ligand and perpendicular to the NHC ligand plane. I hypothesized that rotation of the benzylic groups could impart some degree of lability of the **DBnBI** ligands. I repeated the exchange reaction while also refluxing the reaction mixture. Upon work-up, SCXRD analysis of the crystals isolated were, remarkably, another open faced, $[Co_5Se_8(PEt_3)_5][PF_6]$, shown in figure 4.8b.

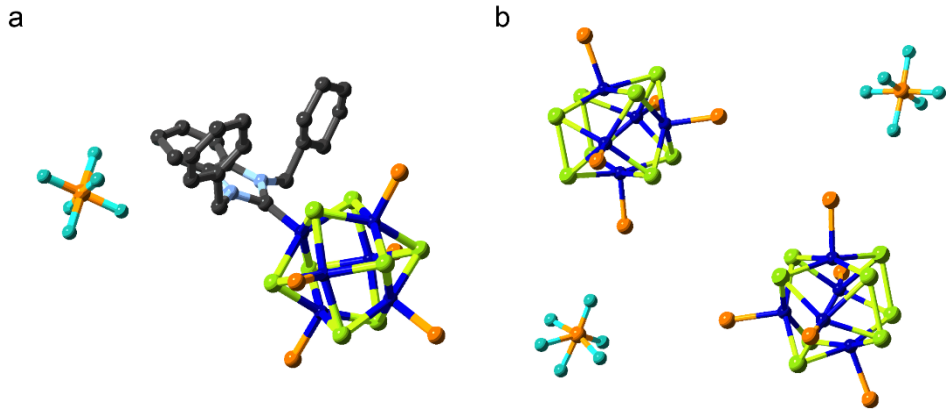

Figure 4.8: a. Crude structure of $[Co_6Se_8(PEt_3)_5($**DBnBI**$)][PF_6]$ obtained from SCXRD data, R = 13.63% without complete refinement. **b.** Structure of $[Co_5Se_8(PEt_3)_5][PF_6]$ obtained from SCXRD R = 21.03% without complete refinement. Ethyl groups of PEt_3 ligands, solvent molecules, and hydrogen atoms omitted for clarity. Color code: Se: green; Co: blue; P: orange; N: light blue; C: black; F: aqua.

Moving to the bulkier **D^{neo}PBI** ligand and again under the same conditions as those used for the synthesis of $[Co_6Se_8(PEt_3)_5($**D^{i}PrBI**$)][PF_6]$, another rather interesting result was obtained. Instead of behaving similarly to the **DBnBI** ligand, the dimerized $[Co_{12}Se_{16}(PEt_3)_{10}][PF_6]_2$ superatomic salt was obtained.[15] Because the $[Co_6Se_8(PEt_3)_5(CO)][PF_6]$ superatom only contained one photolabile ligand only a dimer was possible; however, could the *trans*-$[Co_6Se_8(PEt_3)_4(CO)_2][PF_6]$ superatom be used to form oligomers or polymers? To answer this, the reaction was performed again using *trans*-$[Co_6Se_8(PEt_3)_4(CO)_2][PF_6]$. From this reaction, only the [*trans*-$Co_{12}Se_{16}(PEt_3)_8(CO)_2][PF_6]_2$ salt was obtained, crude crystal structure given in

Figure 4.9. From this result, the dimerization process does not proceed past formation of the dicationic [*trans*-$Co_{12}Se_{16}(PEt_3)_8(CO)_2$], perhaps because the product is too electron deficient. This conclusion should be investigated and iterative reduction followed by additional fusion reactions could result in the formation of tunable superatom oligomers.

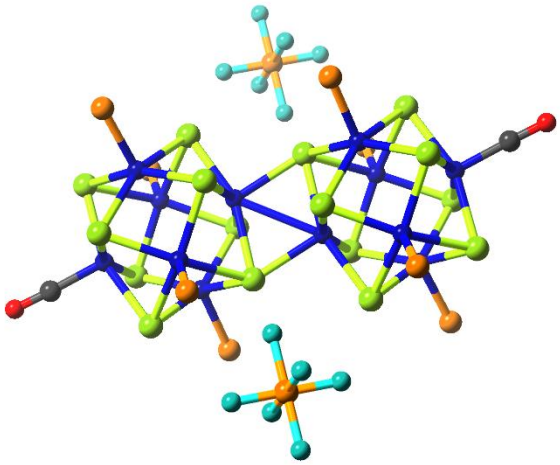

Figure 4.9: Structure of [*trans*-$Co_{12}Se_{16}(PEt_3)_8(CO)_2$][$PF_6$]$_2$ obtained from SCXRD data, R = 7.27% without complete refinement. Ethyl groups of PEt_3 ligands and hydrogen atoms omitted for clarity. Color code: Se: green; Co: blue; P: orange; C: black; O: red; F: aqua.

4.10 Conclusions and Outlook

The use of NHCs as ligands for superatoms, especially highly functionalized NHC ligands, offers many exciting possibilities to expand current properties and assembly methods for superatoms. The initial goal of elucidating a reliable method for installing NHC ligands onto superatoms was realized, however many unexpected results were obtained and several new questions and challenges were uncovered. As this work developed, new synthetic techniques and purification methods were utilized and future work should include applying these methods to

previously unsuccessful attempts. There are several potential avenues of future work presented by these results which could expand the currently available superatom tool-box

4.11 Synthetic Details

2-Iodopropane was purchased from Acros Organics. 4-bromo-2-nitroaniline and Ammonium chloride were purchased from Alfa Aesar. DMSO-d_6, benzene-d_6, and $CDCl_3$ were purchased from Cambridge Isotope. Dichloromethane (DCM), diethyl ether, dioxane, ethyl acetate, hexanes, isopropanol, sodium chloride, and tetrahydrofuran (THF) were purchased from Fisher Scientific. Silica gel was purchased from Silicycle. Triethylorthoformate was purchased from TCI. All other reagents and solvents were purchased from Sigma-Aldrich. Dry and deoxygenated solvents were prepared by elution through a dual-column solvent system (MBraun SPS). All reactions and sample preparations were carried out under inert atmosphere using standard Schlenk techniques or in a nitrogen-filled glovebox unless otherwise noted. ^{1}H, ^{13}C, and ^{31}P NMR spectra were recorded on Bruker DRX300, DRX400, and DMX500 spectrometers. ^{1}H and ^{13}C spectra were referenced using DMSO-d_6, C_6D_6, or $CDCl_3$, with the residual solvent peak as the internal standard, and ^{31}P spectra were referenced using H_3PO_4. Chemical shifts were reported in ppm, with ^{1}H multiplicities reported as: s (singlet), d (doublet), t (triplet), q (quartet), p (pentet), m (multiplet), and br (broad) or as indicated. Coupling constants, *J*, are reported in Hz and integration is provided.

D^{i}PrBI[16], 2,3-dibromo-1,4-napthoquinone[17], diisopropylformamidine[18], 1,2-bis(neopentylamine)benzene[19], **D^{neo}PBI**-AgCl[20], $Co_6S_8(PPh_3)_6$[10], and isomers and oxidized versions of the $Co_6Se_8(PEt_3)_{6-x}(CO)_x$ (x = 1 or 2) superatoms[11] were all synthesized according to

published procedures. All free NHCs were synthesized through deprotonation using 1.1 eq. KO^{t}Bu in THF. All NHC-Ag(I)X precursors were synthesized following literature procedure[12].

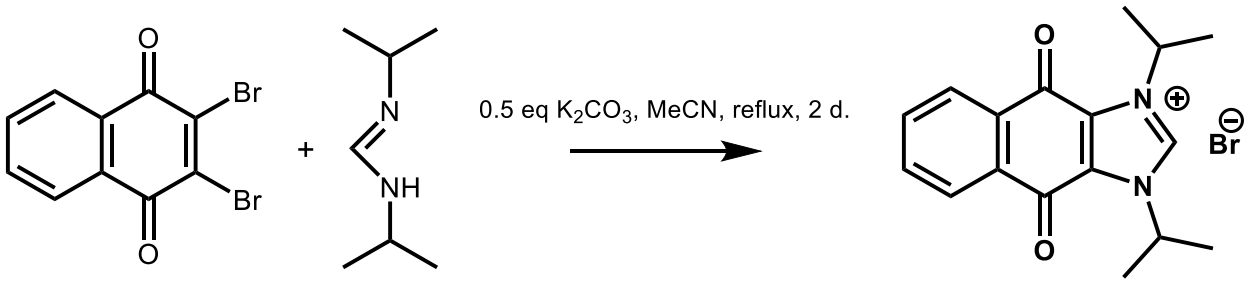

Figure 4.10: Synthetic scheme for the synthesis of **D^{i}PrNQI**-HBr.

D^{i}PrNQI-HBr: **D^{i}PrNQI**-HBr was synthesized by slight modification of a literature procedure[6] using 2,3-dibromo-1,4-napthoquinone and diisopropylformamidine. **D^{i}PrNQI**-HBr was obtained as a bright yellow powder. (Yield: 1.41 g, 50%)

^{1}H NMR (300 MHz, Chloroform-*d*) δ 11.63 (s, 1H), 8.27 (dd, *J* = 5.8, 3.3 Hz, 2H), 7.91 (dd, *J* = 5.8, 3.3 Hz, 2H), 5.75 (p, *J* = 6.8 Hz, 2H), 1.91 (d, *J* = 6.7 Hz, 12H).

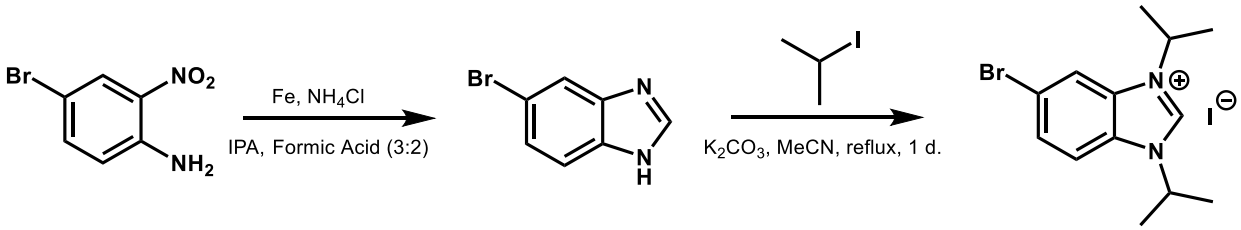

Figure 4.11: Synthetic scheme for the synthesis of **6Br-D^{i}PrBI**-HI.

6Br-D^{i}PrBI-HI: **6Br-D^{i}PrBI**-HI was synthesized by slight modification of a literature procedure[16] starting from 4-bromo-2-nitroaniline. **6Br-D^{i}PrBI**-HI was obtained as an off-white solid. (Yield 1.29 g, 65%)

^{1}H NMR (300 MHz, Chloroform-*d*) δ 11.17 (s, 1H), 8.13 (d, *J* = 1.4 Hz, 1H), 7.94 (dd, *J* = 8.8, 1.4 Hz, 1H), 7.54 (d, *J* = 8.8 Hz, 1H), 5.15 (dt, *J* = 16.8, 6.7 Hz, 2H), 1.87 (dd, *J* = 6.7, 2.3 Hz, 12H).

DBnBI-HBr**: DBnBI**-HBr was synthesized by slight modification of a literature procedure using benzylbromide. **DBnBI**-HBr was obtained as a white powder. (Yield 1.47 g, 92%)

^{1}H NMR (400 MHz, DMSO-d_6) δ 10.07 (s, 1H), 7.97 (dd, *J* = 6.3, 3.1 Hz, 2H), 7.64 (dd, *J* = 6.3, 3.1 Hz, 2H), 7.56 – 7.31 (m, 10H), 5.80 (s, 4H).

General Procedure for photo-assisted ligand exchange reactions: In a N_2 filled glove box, 50 mg of superatom and appropriate equivalents of NHC ligand or transfer reagents were dissolved in 10 mL of THF in a quartz round bottom flask equipped with a stir bar. The flask was then capped with a rubber septa and taped, removed from the glove box, and irradiated under a blue LED for several hours. The reaction mixture was then filtered and solvent removed *en vacuo*.

4.12 NMR Data

$[Co_6Se_8(PEt_3)_5(\mathbf{D^iPrBI})][PF_6]$**:** ^{1}H NMR (300 MHz, Chloroform-*d*) δ 7.54 (dd, *J* = 6.1, 3.2 Hz, 2H), 7.22 (dd, *J* = 6.2, 3.1 Hz, 2H), 5.97 (m, 2H) 1.95 (dd, *J* = 11.5, 7.6 Hz, 12H), 0.53 (br, 1H), 0.37 (br, 9H), 0.25 (br, 36H), -0.67 (d, *J* = 7.2 Hz, 24H). ^{31}P NMR (162 MHz, Chloroform-*d*) δ -148.75 (m) -431.58 (br) -500.33 (br).

4.13 Single Crystal X-Ray Diffraction

Single crystal x-ray diffraction data was collected on an Agilent SuperNova diffractometer using mirror-monochromated CuK_{α} radiation. Data collection, integration, scaling (ABSPACK) and absorption correction (face-indexed Gaussian integration[21] or numeric analytical methods[22]) were performed in CrysAlisPro.[23] Structure solution was performed using ShelXT.[24] Subsequent refinement was performed by full-matrix least-squares on F^2 in ShelXL.[24] Olex2[25] was used for viewing and to prepare CIF files. Many disordered molecules were modeled as rigid fragments from the Idealized Molecular Geometry Library.[26] ORTEP graphics were prepared in CrystalMaker.[27] Selected details of crystallographic data are provided in Table 4.1.

Crystals were mounted on MiTeGen mounts with the aid of STP oil and cooled to 100 K on the diffractometer for screening and data collection, except in the case of **NHC1–AgCl** which was collected at room temperature. A minimum of 1 hemisphere of data to 0.8 Å resolution was collected for all compounds.

Structure solution and space group assignment were typically performed in ShelXT with no difficulty. The structures given in this chapter are not completely refined and full refinement or recollection of the data remains necessary.

Table 4.1: Selected Crystallographic Data.

Compound	*trans*-$Co_6S_8(PPh_3)_4$(**D^{i}PrNQI**)$_2$	*trans*-$Co_6Se_8(PEt_3)_4$(**D^{i}PrNQI**)$_2$	$[Co_5Se_8(PEt_3)_5]_2[Ag_2I_4]$	$[Co_6Se_8(PEt_3)_5$(**D^{i}PrBI**)$][PF_6]$
Space group	I4/m	C2/c	P-1	$P2_1/n$
***a* (Å)**	16.1171(3)	20.0368(16)	13.9540(3)	15.1327(7)
***b* (Å)**	16.1171(3)	21.6925(13)	14.1837(4)	26.9579(16)
***c* (Å)**	18.4287(4)	17.7940(13)	32.4898(6)	18.7638(8)
***α* (°)**	90	90	86.466(2)	90
***β* (°)**	90	104.175(7)	85.125(2)	94.588(4)
***γ* (°)**	90	90	67.011(2)	90
V (Å^3)	4787.06(16)	7498.6(10)	5908.1(3)	7630.1(7)
T (K)	100	100.0(2)	100.0(2)	100.0(2)
λ (Å)	1.54184	1.54184	1.54184	1.54184
R_1(obs)	0.1245	0.0943	0.1047	0.0975
wR_2(all)	0.3357	0.2308	0.3139	0.3353

Compound	*trans*-$[Co_6Se_8(PEt_3)_4$(**D^{i}PrBI**)$_2][PF_6]$	$[Co_6Se_8(PEt_3)_5$(**6Br-D^{i}PrBI**)$][PF_6]$	$Co_6Se_8(PEt_3)_5$(**6B(OH)$_2$-D^{i}PrBI**)	$[Co_6Se_8(PEt_3)_5$(**DBnBI**)$][PF_6]$
Space group	R-3	$P2_1/c$	Pnna	P-1
***a* (Å)**	32.1399(7)	25.3078(6)	27.241(9)	19.3542(9)
***b* (Å)**	32.1399(7)	16.6081(3)	16.716(4)	19.5208(11)
***c* (Å)**	20.4159(4)	37.3847(8)	15.172(6)	21.8832(10)
***α* (°)**	90	90	90	114.082(5)
***β* (°)**	90	96.421(2)	90	101.120(4)
***γ* (°)**	120	90	90	93.137(4)
V (Å^3)	18263.7(7)	15614.8(6)	6909(4)	7323.8(7)
T (K)	100	100.0(2)	100.0(2)	99.9(2)
λ (Å)	1.54184	1.54184	1.54184	1.54184
R_1(obs)	0.0735	0.1029	0.1715	0.1363
wR_2(all)	0.2296	0.2970	0.3911	0.2627

Compound	$[Co_5Se_8(PEt_3)_5][PF_6]$	$[trans\text{-}Co_{12}Se_{16}(PEt_3)_8(CO)_2][PF_6]_2$
Space group	$P2_1/c$	P-1
***a* (Å)**	22.5386(9)	12.6104(4)
***b* (Å)**	17.0389(11)	13.3984(4)
***c* (Å)**	31.7142(19)	14.7251(6)
***α* (°)**	90	115.259(4)
***β* (°)**	92.505(5)	98.163(3)
***γ* (°)**	90	95.575(3)
V (Å³)	12167.7(12)	2192.42(16)
T (K)	100	100.0(2)
λ (Å)	1.54184	1.54184
R_1(obs)	0.2103	0.727
wR_2(all)	0.5040	0.2143

4.14 References

1. Choi, B. N.; Paley, D. W.; Siegrist, T.; Steigerwald, M. L.; Roy, X., Ligand Control of Manganese Telluride Molecular Cluster Core Nuclearity. *Inorganic Chemistry* **2015,** *54*, 8348-8355.

2. Durham, J. L.; Wilson, W. B.; Huh, D. N.; McDonald, R.; Szczepura, L. F., Organometallic rhenium(III) chalcogenide clusters: coordination of N-heterocyclic carbenes. *Chemical Communications* **2015,** *51*, 10536-10538.

3. Smith, C. A.; Narouz, M. R.; Lummis, P. A.; Singh, I.; Nazemi, A.; Li, C. H.; Crudden, C. M., N-Heterocyclic Carbenes in Materials Chemistry. *Chemical Reviews* **2019,** *119*, 4986-5056.

4. Deng, L.; Holm, R. H., Stabilization of fully reduced iron-sulfur clusters by carbene ligation: The [Fe(n)S(n)](0) oxidation levels (n=4, 8). *Journal of the American Chemical Society* **2008,** *130*, 9878-9886.

5. Doud, E. A.; Inkpen, M. S.; Lovat, G.; Montes, E.; Paley, D. W.; Steigerwald, M. L.; Vazquez, H.; Venkataraman, L.; Roy, X., In Situ Formation of N-Heterocyclic Carbene-Bound Single-Molecule Junctions. *Journal of the American Chemical Society* **2018,** *140*, 8944-8949.

6. Sanderson, M. D.; Kamplain, J. W.; Bielawski, C. W., Quinone-annulated N-heterocyclic carbene-transition-metal complexes: Observation of pi-backbonding using FT-IR spectroscopy and cyclic voltammetry. *Journal of the American Chemical Society* **2006,** *128*, 16514-16515.

7. Rosen, E. L.; Varnado, C. D.; Tennyson, A. G.; Khramov, D. M.; Kamplain, J. W.; Sung, D. H.; Cresswell, P. T.; Lynch, V. M.; Bielawski, C. W., Redox-Active N-Heterocyclic Carbenes: Design, Synthesis, and Evaluation of Their Electronic Properties. *Organometallics* **2009,** *28*, 6695-6706.

8. Clavier, H.; Nolan, S. P., Percent buried volume for phosphine and N-heterocyclic carbene ligands: steric properties in organometallic chemistry (vol 46, pg 841, 2010). *Chemical Communications* **2010,** *46*, 9260-9261.

9. Poater, A.; Ragone, F.; Giudice, S.; Costabile, C.; Dorta, R.; Nolan, S. P.; Cavallo, L., Thermodynamics of N-heterocyclic carbene dimerization: The balance of sterics and electronics. *Organometallics* **2008,** *27*, 2679-2681.

10. Ong, W. L.; O'Brien, E. S.; Dougherty, P. S. M.; Paley, D. W.; Higgs, C. F.; McGaughey, A. J. H.; Malen, J. A.; Roy, X., Orientational order controls crystalline and amorphous thermal transport in superatomic crystals. *Nature Materials* **2017,** *16*, 83-88.

11. Champsaur, A. M.; Velian, A.; Paley, D. W.; Choi, B.; Roy, X.; Steigerwald, M. L.; Nuckolls, C., Building Diatomic and Triatomic Superatom Molecules. *Nano Letters* **2016,** *16*, 5273-5277.

12. Wang, H. M. J.; Lin, I. J. B., Facile synthesis of silver(I)-carbene complexes. Useful carbene transfer agents. *Organometallics* **1998,** *17*, 972-975.

13. Ishiyama, T.; Murata, M.; Miyaura, N., Palladium(O)-Catalyzed Cross-Coupling Reaction of Alkoxydiboron with Haloarenes - a Direct Procedure for Arylboronic Esters. *Journal of Organic Chemistry* **1995,** *60*, 7508-7510.

14. Champsaur, A. M.; Yu, J.; Roy, X.; Paley, D. W.; Steigerwald, M. L.; Nuckolls, C.; Bejger, C. M., Two-Dimensional Nanosheets from Redox-Active Superatoms. *Acs Central Science* **2017,** *3*, 1050-1055.

15. Champsaur, A. M.; Hochuli, T. J.; Paley, D. W.; Nuckolls, C.; Steigerwald, M. L., Superatom Fusion and the Nature of Quantum Confinement. *Nano Letters* **2018,** *18*, 4564-4569.

16. Crudden, C. M.; Horton, J. H.; Ebralidze, II; Zenkina, O. V.; McLean, A. B.; Drevniok, B.; She, Z.; Kraatz, H. B.; Mosey, N. J.; Seki, T.; Keske, E. C.; Leake, J. D.; Rousina-Webb, A.; Wu, G., Ultra stable self-assembled monolayers of N-heterocyclic carbenes on gold. *Nat Chem* **2014,** *6*, 409-414.

17. Anuratha, M.; Jawahar, A.; Umadevi, M.; Sathe, V. G.; Vanelle, P.; Terme, T.; Meenakumari, V.; Benial, A. M. F., SERS investigations of 2,3-dibromo-1,4-naphthoquinone on silver nanoparticles. *Spectrochimica Acta Part a-Molecular and Biomolecular Spectroscopy* **2013,** *105*, 218-222.

18. Kuhn, K. M.; Grubbs, R. H., A facile preparation of imidazolinium chlorides. *Organic Letters* **2008,** *10*, 2075-2077.

19. Daniele, S.; Drost, C.; Gehrhus, B.; Hawkins, S. M.; Hitchcock, P. B.; Lappert, M. F.; Merle, P. G.; Bott, S. G., Synthesis and structures of crystalline dilithium diamides and aminolithium amides derived from N,N '-disubstituted 1,2-diaminobenzenes or 1,8-diaminonaphthalene. *Journal of the Chemical Society-Dalton Transactions* **2001**, 3179-3188.

20. Kuhl, O.; Saravanakumar, S.; Ullah, F.; Kindermann, M. K.; Jones, P. G.; Kockerling, M.; Heinicke, J., Anellated N-heterocyclic carbenes: 1,3-dineopentyl-benzimidazol-2-ylidene, structural aspects of C-protonated precursor salts and an AgCl complex. *Polyhedron* **2008,** *27*, 2825-2832.

21. Blanc, E.; Schwarzenbach, D.; Flack, H. D., The evaluation of transmission factors and their first derivatives with respect to crystal shape parameters. *Journal of Applied Crystallography* **1991,** *24*, 1035-1041.

22. Clark, R. C.; Reid, J. S., The analytical calculation of absorption in multifaceted crystals. *Acta Crystallographica Section A* **1995,** *51*, 887-897.

23. *CrysAlisPro*, Version 1.171.37.35; Oxford Diffraction /Agilent Technologies UK Ltd: Yarnton, England, 2014.

24. Sheldrick, G., SHELXT - Integrated space-group and crystal-structure determination. *Acta Crystallographica Section A* **2015,** *71*, 3-8.

25. Dolomanov, O. V.; Bourhis, L. J.; Gildea, R. J.; Howard, J. A. K.; Puschmann, H., OLEX2: a complete structure solution, refinement and analysis program. *Journal of Applied Crystallography* **2009,** *42*, 339-341.

26. Guzei, I., An idealized molecular geometry library for refinement of poorly behaved molecular fragments with constraints. *Journal of Applied Crystallography* **2014,** *47*, 806-809.

27. *CrystalMaker*, CrystalMaker Software Ltd: Oxford, England.

Chapter 5: Nickel Phosphinidene Molecular Clusters from Organocyclophosphine Precursors

5.1 Preface

Significant portions of this chapter are adapted from a publication on this research entitled "Nickel Phosphinidene Molecular Clusters from Organocyclophosphine Precursors" by Evan A. Doud, Chiara J. Butler, Daniel W. Paley, and Xavier Roy published in *Chemistry – A European Journal*, **2019**, 25, 10840-10844. In this work I sought expand the library of available superatoms. I synthesized and characterized the compounds used in this study with the aid of a talented undergraduate student, Chiara J. Butler. Dr. Dan Paley assisted with single crystal X-ray diffraction refinement.

5.2 Introduction

Superatoms, and more broadly clusters, are of fundamental interest and importance as a bridge between molecular chemistry and solid state chemistry[1] due to their unique physical and chemical properties.[2-4] Transition metal chalcogenide molecular superatoms and clusters, in particular, have been extensively investigated in this context: their chemistry is well established,[5] and their combination of atomic precision, tunability and functionality makes them attractive building blocks for creating novel materials with tailored properties.[6-13] The properties and use of superatoms as building blocks in novel materials was discussed in greater detail in Chapter 1. Additionally, many metal chalcogenide clusters can be used as single-source molecular precursors to various bulk phases.[14]

Analogous to metal chalcogenides, metal pnictides have a rich structural chemistry. Metal phosphides play a critical role in many applications, including as catalyst in the hydrodesulfurization of hydrocarbon feedstocks and in the hydrogen evolution reaction.[15-16] While nanocrystals of metal phosphide have been studied extensively,[17-20] their molecular cluster counterparts have received scant attention,[21-22] especially when compared to metal chalcogenides, and have not been considered in a superatom context. This is primarily due to synthetic challenges associated with the design of appropriate precursors and with the coordination geometry of the phosphide anion, which typically produces extended structures instead of clusters. To circumvent these issues, phosphinidene groups (PR), which are isolobal to the chalcogen, have been used as "functional phosphides" to create a limited number of metal phosphinidene clusters.[23-25] These compounds are typically prepared using RPX_2 precursors, where X is H, Cl or $SiMe_3$.

Here we report a new family of nickel-rich molecular clusters prepared using organocyclophosphines $(PR)_n$ as precursors. Organocyclophosphines have been known since 1877[26] but their synthetic utility beyond mere laboratory curiosities was only recognized much later.[27] They have seldom been employed as precursors for molecular clusters and the few reported approaches do not produce monomeric phosphinidene ligands but instead leave the cyclic framework intact.[28-30] By reacting various organocyclophosphines with bis(1,5-cyclooctadiene)nickel(0) ($Ni(COD)_2$) and trialkylphosphine (PR'_3), we observe cleavage of the phosphorus ring P–P bonds and formation of phosphinidene-bridged nickel clusters. By changing the steric environments of both the organocyclophosphines and the trialkylphosphine capping ligand, we form molecular clusters of different sizes, structures and compositions. Remarkably, certain combinations of $(PR)_n$ and PR'_3 produce clusters with open Ni coordination sites. As an

illustration of their potential utility as single-source molecular precursors to catalytically-active compounds, we show that the clusters convert to Ni_2P phase via low temperature thermolysis.

5.3 Synthesis of Nickel Phosphinidene Molecular Clusters

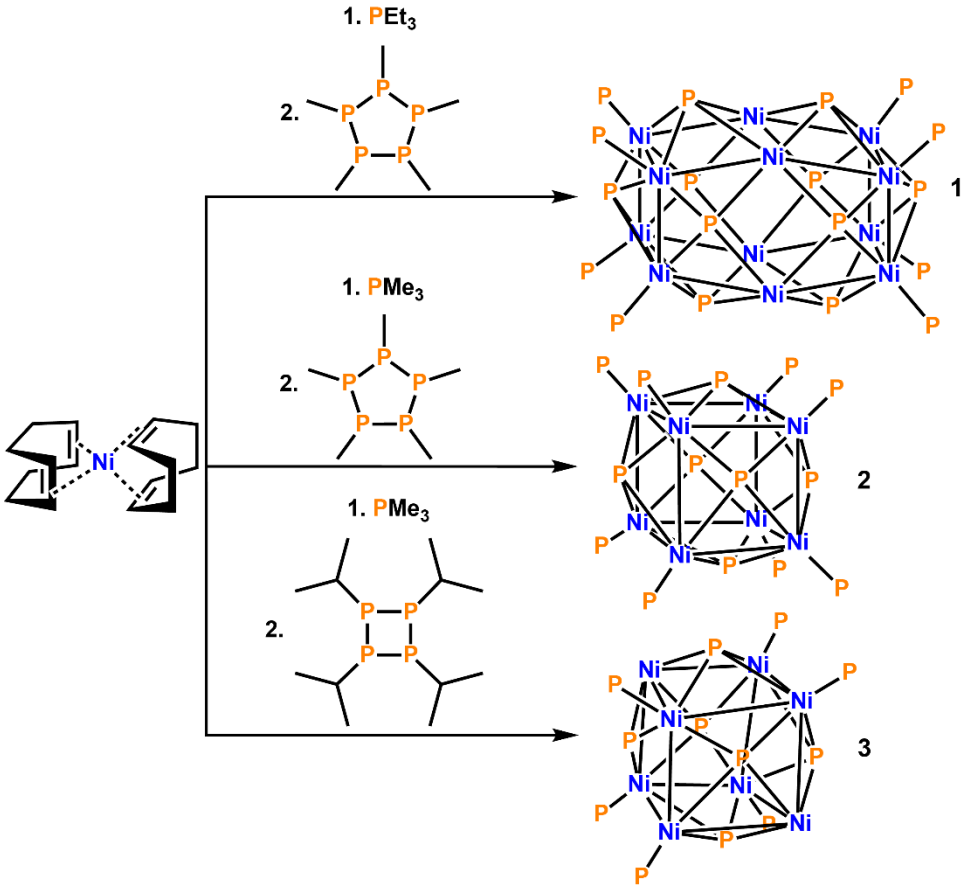

Figure 5.33. Synthesis of nickel phosphinidene molecular clusters **1-3**.

Our synthetic approach is illustrated in Figure 5.1. Pentamethylcyclopentaphosphine, $((PMe)_5)$ and tetra(isopropyl)cyclotetraphosphine $((P^iPr)_4)$ are prepared by reacting $MePCl_2$ and $^iPrPCl_2$ with LiH and Mg, respectively.[31] We first explore the reactivity of these cyclic molecules

with $Ni(COD)_2$ and their potential use as precursors for making bulk nickel phosphide. When $(PMe)_5$ is added to a toluene solution of $Ni(COD)_2$ in a 1:5 stoichiometric ratio, a black precipitate forms instantly. This solid is highly air sensitive, insoluble in all organic solvents and amorphous, as determined from powder x-ray diffraction (PXRD) (Figure 5.5). Heating the solid to 450 °C in a quartz tube sealed under vacuum yields a crystalline material whose PXRD pattern indicates the presence of various nickel phosphide phases, dominated by Ni_5P_4, and Ni metal (Figure 5.6).

To form molecular clusters, we add an excess of PR_3' to terminate the polymerization reaction and passivate the surface Ni metal atoms. The structure of the cluster is determined by the alkyl substituents R and R' on the phosphinidene and capping ligand, respectively. When we combine $Ni(COD)_2$, $(PMe)_5$ and PEt_3 in toluene at room temperature, we obtain a black solution from which large black prismatic single crystals form upon layering with hexanes. The resulting compound is a molecular cluster with the formula $Ni_{12}(PMe)_{10}(PEt_3)_8$ (**1**), as determined by single crystal x-ray diffraction (SCXRD) (Figure 5.2a). The core structure is formed by two fused, face-sharing cubes of Ni atoms with each open Ni_4 face capped with a quadruply bridging μ_4-PMe group. The eight Ni atoms located at the vertices of the rectangular prism are capped by eight PEt_3 while the four face-bridging Ni atoms located along the belt of the cluster are devoid of PEt_3, leaving an open coordination site on each metal center. To some extent, this structure resembles that of the cluster $Ni_{12}Cl_2(PPh)_2(P_2Ph_2)_4(PHPh)_8$ reported by Fenske and co-workers,[32] albeit the electronic structure of **1** is completely different.

5.4 Structural Analysis, Characterization, and Oxidation of $Ni_{12}(PMe)_{10}(PEt_3)_8$

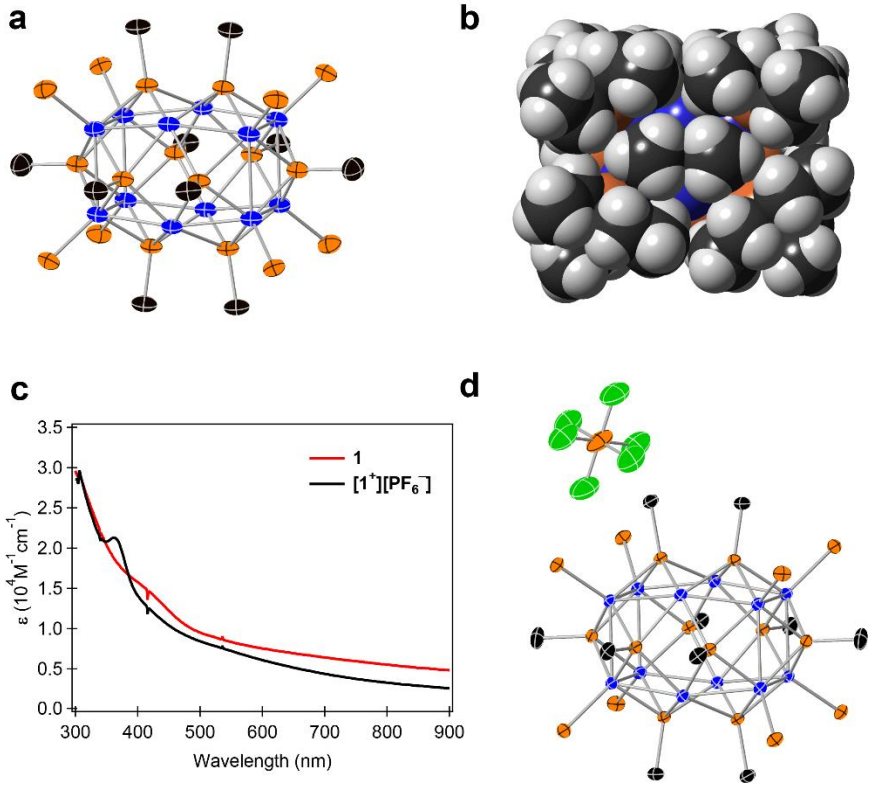

Figure 5.34: a. Molecular structure of **1** showing the thermal ellipsoid at 50 % probability. **b.** Space filling model of **1**. **c.** Electronic absorption spectra of **1** (red) and [**1**$^+$][PF_6^-] (black) **d.** Molecular structure of [**1**$^+$][PF_6^-] showing the thermal ellipsoid at 50 % probability. . Color code: Ni: blue; P: orange; C: black; F: green. H atoms and Et groups are removed for clarity.

The Ni–Ni distances along the rectangular prism edges range from 2.56 to 2.69 Å, suggesting interactions between the metal atoms. Consistent with this hypothesis, the Ni vertices adopt an 18 electron count if we assume that each atom is bonded to three neighboring metal centers. The shortest distance between neighboring face-capping μ_4-P atoms is 2.51 Å, significantly longer than the expected bond length for a singly P–P bond (2.24 Å).[33] The separation between the Ni atoms located along the belt of the cluster is much longer (~3.2 Å), indicating that there is no bonding between these atoms. The electron count of these Ni atoms is 16. The space-

filling model of **1** in Figure 5.2b shows that the steric bulk of the PEt_3 and PMe groups prevents the coordination of a ligand to the belt metal atoms.

Once crystallized, **1** is poorly soluble in tetrahydrofuran (THF) and toluene, and essentially insoluble in other organic solvents. The ^{31}P NMR spectrum of **1** shows two broad peaks at –3.8 and –19.2 ppm (Figure 5.11). Figure 5.2c shows the electronic absorption spectrum of the cluster: the absorption coefficient is largest at short wavelength, and we observe a weak shoulder at ~410 nm with a long tail across the whole visible region. The broad, mostly featureless spectrum is typical of molecular clusters with metal-metal bonding,[14] which is consistent with our SCXRD analysis. UV-Vis spectra were recorded using a 1.0 cm quartz cell on a Shimadzu UV-1800 spectrophotometer.

Cluster **1** is readily oxidized and the resulting cationic cluster $\mathbf{1}^+$ is significantly more soluble in THF. To prepare $\mathbf{1}^+$, the neutral cluster is suspended in THF with one equivalent of ferrocenium hexafluorophosphate, $[Fc^+][PF_6^-]$. After 12 h, most of the cluster is dissolved and a dark brown solution is obtained. The cluster salt $[\mathbf{1}^+][PF_6^-]$ is isolated by evaporating the solvent and washing the residue with toluene to remove Fc. Black rectangular prismatic single crystals of $[\mathbf{1}^+][PF_6^-]$ are grown by dissolving the solid in THF and layering the solution with hexanes. SCXRD confirms that the cluster is singly oxidized and that its core structure is maintained (Figure 5.2d). A comparison of the bond lengths and angles for **1** and $\mathbf{1}^+$ reveals a small contraction and slight distortion of the Ni_{12} core when compared to the neutral one. The electronic absorption spectrum of $[\mathbf{1}^+][PF_6^-]$ is similar to that of **1** but the weak shoulder is sharper, stronger and blue shifted to 361 nm as shown in Figure 5.2c.

5.5 Structural Tunability of the Nickel Phosphinidene Molecular Cluster Core

The structure of the core can be modified by changing the substituents R and R' in $(PR)_n$ and PR'_3. For instance, when PMe_3 is used as the capping ligand instead of PEt_3, a new cluster is obtained, $Ni_8(PMe)_6(PMe_3)_8$ (**2**). Figure 5.3a shows the crystal structure of **2**, which consists of an essentially regular Ni_8 cube (Ni–Ni distances: 2.64–2.66 Å; Ni–Ni–Ni angles: 89.2–90.6º) whose Ni atoms are coordinated by PMe_3. Each face is capped by a μ_4-PMe group. This structure has been observed in related Ni clusters, including $Ni_8(PPh)_6(CO)_8$ [34] and $Ni_8(PPh)_6(PPh_3)_4Cl_4$.[35] Moreover, this structure is closely related to the cubic close-packed $Ni_9Te_6(PEt_3)_8$ cluster[36] shown in Figure 5.3b, in which Te atoms are replaced by isolobal PMe groups and the central Ni atom is missing.

We also examine the effect of increasing the steric bulk on the organocyclophosphine. By replacing $(PMe)_5$ with $(P^iPr)_4$, we obtain the cluster $Ni_8(P^iPr)_6(PMe_3)_6$ (**3**). Its crystal structure shows that the core is similar to that of **2** but the Ni_8 cube is highly distorted (Figure 5.3c). Two Ni atoms located at opposite vertices lack coordinated PMe_3 ligands due to the increased steric bulk of P^iPr, and the bond lengths between these uncapped Ni atoms and neighboring Ni metal centers is short (~2.49 Å), suggesting especially strong interactions. By contrast, the separation between neighboring PMe_3-coordinated Ni atoms is significantly longer (2.73 Å), resulting in an overall rhombohedral distortion of the core.

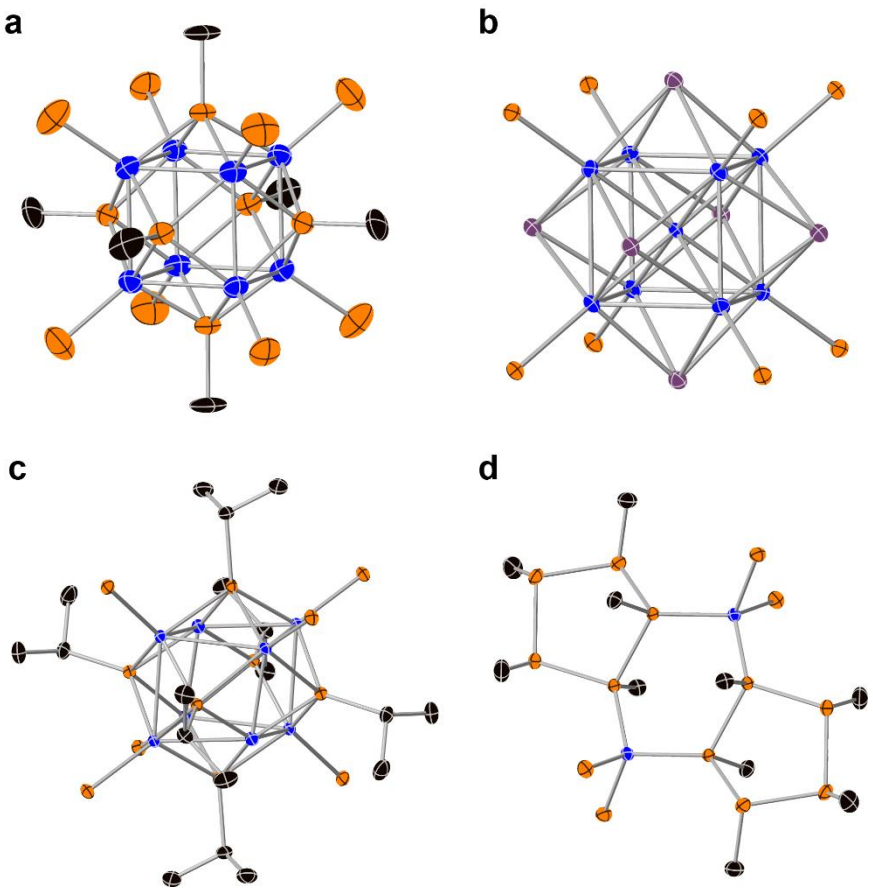

Figure 5.35. Molecular structures of **a. 2 b.** $Ni_9Te_6(PEt_3)_8$ **c. 3**, and **d. 4**. Thermal ellipsoids shown at 50% probability. Color code is the same as in Figure 5.2 with Te: purple. H atoms and R' groups on the capping ligands are removed for clarity.

The mechanism by which these clusters form is unknown but the fragmentation of the phosphorus ring is evidently accomplished by the zerovalent $Ni(COD)_2$ complex, which is oxidized along the process. By reacting an excess of PMe_3 and $(PMe)_5$ with $Ni(COD)_2$, we isolated the dimeric complex $Ni_2(PMe_3)_2((PMe)_5)_2$ (**4**) in which the $(PMe)_5$ rings are intact and bridging the two Ni atoms (Figure 5.3d). **4** may well be an intermediate in the cluster forming reaction and reveals how the Ni complex binds the organocyclophosphine before cleavage of the P–P bonds.

The intact $(PMe)_5$ rings in **4** provide a rationalization as to why we don't observe the formation of any cluster when we decrease the $Ni(COD)_2$:cyclophosphine stoichiometric ratio in the reaction.

5.6 Thermolysis of $Ni_{12}(PMe)_{10}(PEt_3)_8$ into Ni_2P

The reaction of $Ni(COD)_2$ and $(PMe)_5$ without any capping ligand added to the solution produces an amorphous solid that is converted to a mixture of polycrystalline nickel phosphide phases upon annealing. By contrast, the thermolysis of **1** gives essentially pure phase Ni_2P. To convert the cluster into Ni_2P, **1** is sealed under vacuum in a quartz tube and heated to 450 °C in a tube furnace, leaving one end of the tube cold. The condensate at the cold end of the tube is primarily PEt_3, along with unidentified phosphorus containing decomposition products (Figures 5.12 & 5.13). The PXRD pattern of the resulting black solid (black trace in Figure 5.4) confirms the complete decomposition of **1** and the formation of Ni_2P (calculated Ni_2P PXRD pattern is in blue in Figure 5.4). From the intensity of the diffraction peaks, we conclude that while Ni_2P is the majority phase, with a very small amount of NiP impurity, marked by * in Figure 5.4, present. These results establish that nickel phosphinidene clusters such as **1** can be used as single-source molecular precursor to bulk phosphides. The Ni_2P phase formed using **1** is noteworthy due to its outstanding catalytic activity.[15-16, 37]

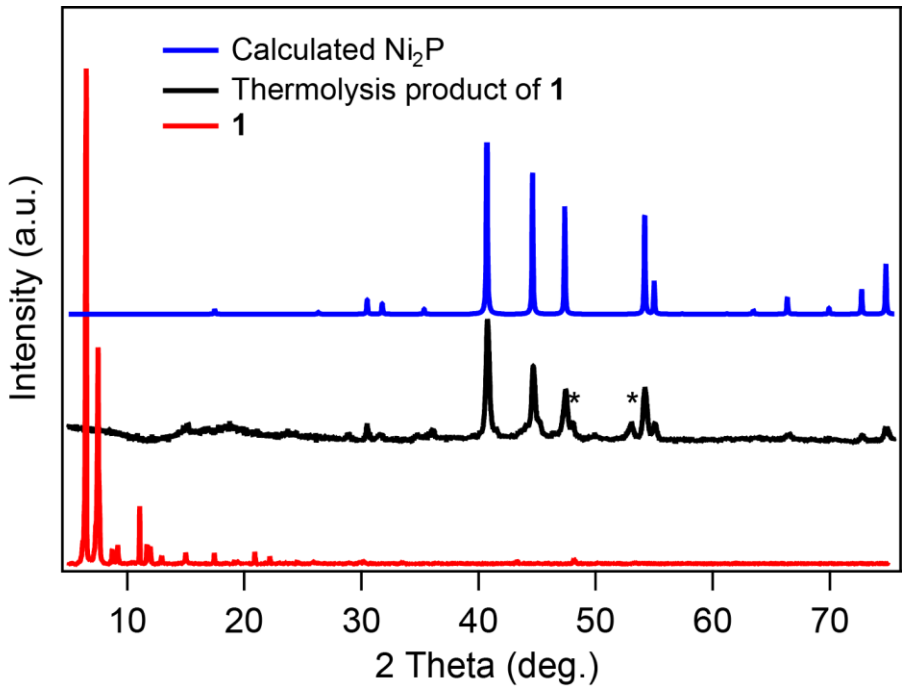

Figure 5.36. PXRD patterns of cluster **1** (red), thermolysis product of **1** (black), and calculated Ni_2P (blue). The NiP impurity peaks are marked by *.

5.7 Conclusion and Outlook

We have established organocyclophosphines as tunable precursors for making nickel phosphinidene molecular clusters. The reaction of $Ni(COD)_2$ with the cyclic phosphorus molecules cleaves the P–P bonds to generate phosphinidene groups that form charge-neutral clusters. We have shown that the cluster core structure and composition is controlled by the bulkiness of the precursor and the capping ligands. These nickel phosphinidene clusters can be used as low temperature single-source molecular precursors to the catalytically active Ni_2P phase. More broadly, this reaction could be applied to different transition metals and cyclic pnictogen molecular

precursors, charting a clear path to create new families of transition metal pnictinidene molecular clusters.

5.8 Additional Synthetic Details

Benzene-d_6 (C_6D_6), tetrahydrofuran-d_8 (THF-d_8), and magnesium turnings were purchased from ACROS Scientific. Lithium hydride (LiH) and crystalline iodine were purchased from Alfa Aesar. Acetonitrile, hexanes, tetrahydrofuran (THF) and toluene were purchased from Fisher Scientific. Dichloromethylphosphine, dichloroethylphosphine, dichloroisopropylphosphine, ferrocene, ferrocenium hexafluorophosphate ($FcPF_6$), tetra-n-butylammonium hexafluorophosphate ($TBAPF_6$), and trimethylphosphine (PMe_3) were purchased from Sigma. Bis(1,5-cyclooctadiene)nickel(0) ($Ni(COD)_2$) and triethylphosphine (PEt_3) were purchased from Strem. Dry and deoxygenated solvents were prepared by elution through a dual-column solvent system (MBraun SPS) or dried over activated 3Å molecular sieves followed by distillation under an inert atmosphere. All reactions and sample preparations were carried out under inert atmosphere using standard Schlenk techniques or in a N_2-filled glovebox. $(PMe)_5$, and $(P^iPr)_4$ were prepared according to published protocol[31, 38]. Note, all compounds prepared here-in are extremely air and moisture sensitive and strict care must be taken when handling these compounds.

$Ni_{12}(PMe)_{10}(PEt_3)_8$ (1). Inside of the glovebox, in a 20-mL scintillation vial equipped with a stir bar, PEt_3 (256 mg, 2.17 mmol) was added to a solution of $Ni(COD)_2$ (298 mg, 1.09 mmol) in 4 mL of toluene. The solution was allowed to stir until all of the $Ni(COD)_2$ was dissolved. A solution of $(PMe)_5$ (50 mg, 0.217 mmol) in 1 mL toluene was added to the $Ni(COD)_2$-PEt_3 solution dropwise, causing an immediate darkening of the solution to a dark brown/black color. The

reaction mixture was allowed to stir for thirty minutes and then filtered through a 0.2 μm syringe filter and layered with 15 mL of hexanes. The reaction mixture was then allowed to sit for one week undisturbed, over this time black crystals of **1** formed. The supernantant solution was decanted, the crystals were carefully washed with 3 x 5 mL of hexanes, and dried *in vacuo*. Yield: 18 mg (9.4 %). $^{31}P\{^{1}H\}$ NMR (tetrahydrofuran-d_8, 202 MHz): δ (ppm) -3.9, -19.3.

[$Ni_{12}(PMe)_{10}(PEt_3)_8$][$PF_6$] ($1^+$). Inside of the glovebox, in a 20-mL scintillation vial equipped with a stir bar, 3.12 mL of a 0.5 mg/mL solution of $FcPF_6$ in THF was added to a black solution of **1** (10 mg, 4.7 μmol) in 5 mL THF. This solution was stirred for 24 hours followed by removal of the solvent *in vacuo*. The residual solids were washed with 3 x 5 mL of toluene and then dried *in vacuo*. Single crystals of **1+** were grown by layering a 5 mL THF solution of **1+** with 15 mL of hexanes. Yield: 9.5 mg (88.9 %). $^{31}P\{^{1}H\}$ NMR (tetrahydrofuran-d_8, 202 MHz): δ (ppm) -146, 6.6, 11.1.

$Ni_8(PMe)_6(PMe_3)_8$ (2). 2 was synthesized similarly to **1** however PMe_3 (123 mg, 1.6 mmol) was used as the capping ligand instead of PEt_3. The diffused reaction solution was placed into a -35°C freezer to facilitate crystallization. Yield: 12 mg (6.5 %).

$Ni_8(P^iPr)_6(PMe_3)_6$ (3). 3 was synthesized similarly to **1** however $(P^iPr)_4$ (50 mg, 0.168 mmol), $Ni(COD)_2$ (185 mg, 0.65 mmol) and PMe_3 (102 mg, 1.3 mmol) were used. The diffused reaction solution was placed into a -35°C freezer to facilitate crystallization. Yield: 5.3 mg (4.6 %).

$Ni_2((PMe)_5)_2(PMe_3)_4$ (4). 4 was synthesized similarly to **1** however $(PMe)_5$ (100 mg, 0.43 mmol), $Ni(COD)_2$ (120 mg, 0.43 mmol) and PMe_3 (66 mg, 0.86 mmol) were used. The diffused reaction solution was placed into a -35°C freezer to facilitate crystallization. Yield: 67.2 mg (34.9 %). ^{1}H NMR (tetrahydrofuran-d_8, 400 MHz): δ (ppm) 1.79 (m, 6H), 1.52 (m, 9H), 1.31 (dd, J = 16.2, 3.6

Hz, 18 H). $^{31}P\{^{1}H\}$ NMR (tetrahydrofuran-d_8, 162 MHz): δ (ppm) 39.6 (m), 32.7 (m), 3.1 (m), -2.0 (m), -9.3 (m), -24.7 (m), -28.4 (m).

5.9 Powder X-ray Diffraction

Powder X-ray diffraction data of all samples was collected using a PANalytical X'Pert^3 Powder diffractometer. Samples were evenly dispersed on a zero-background Si plate and sealed within an air-free domed sample holder.

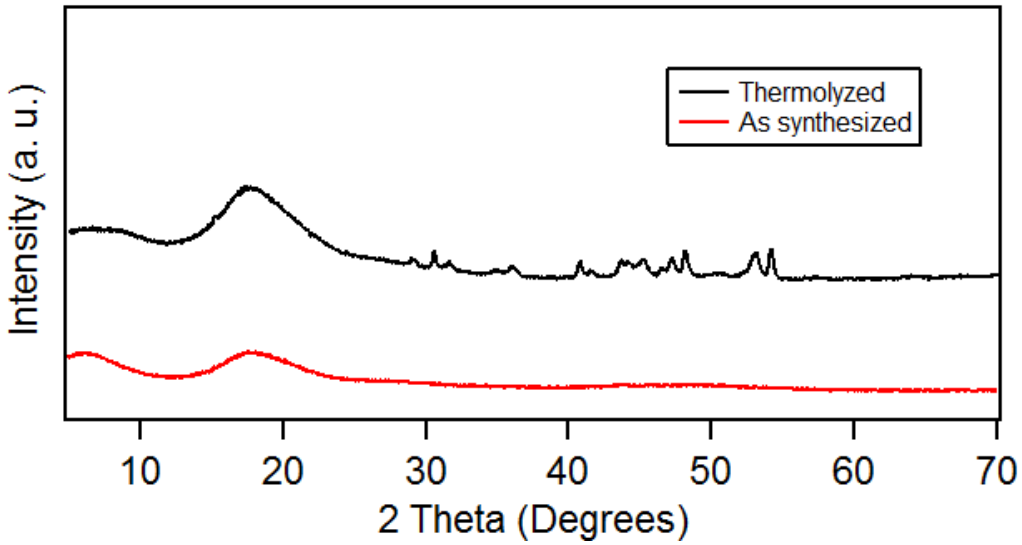

Figure 5.37: PXRD spectra of the material obtained from the combination of $Ni(COD)_2$ and $(PMe)_5$ (red) and its thermolytic conversion to various NiP phases (black). The large, broad signals at ~18 2 theta are due to the air-free domed sample holder.

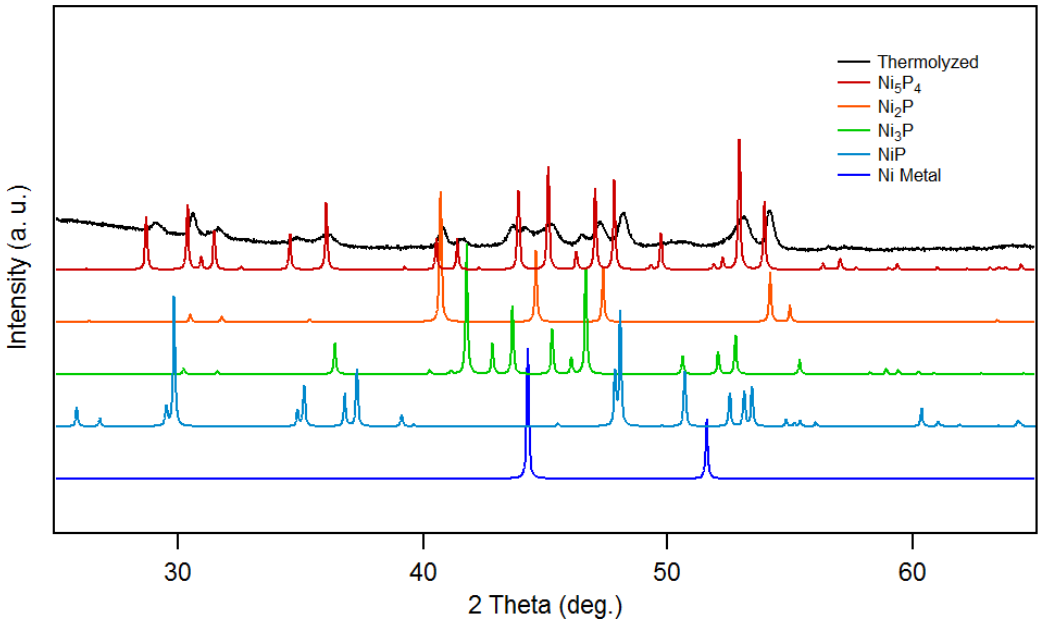

Figure 5.38: Most likely NiP phases produced from the thermolysis of the material obtained from the combination of $Ni(COD)_2$ and $(PMe)_5$.

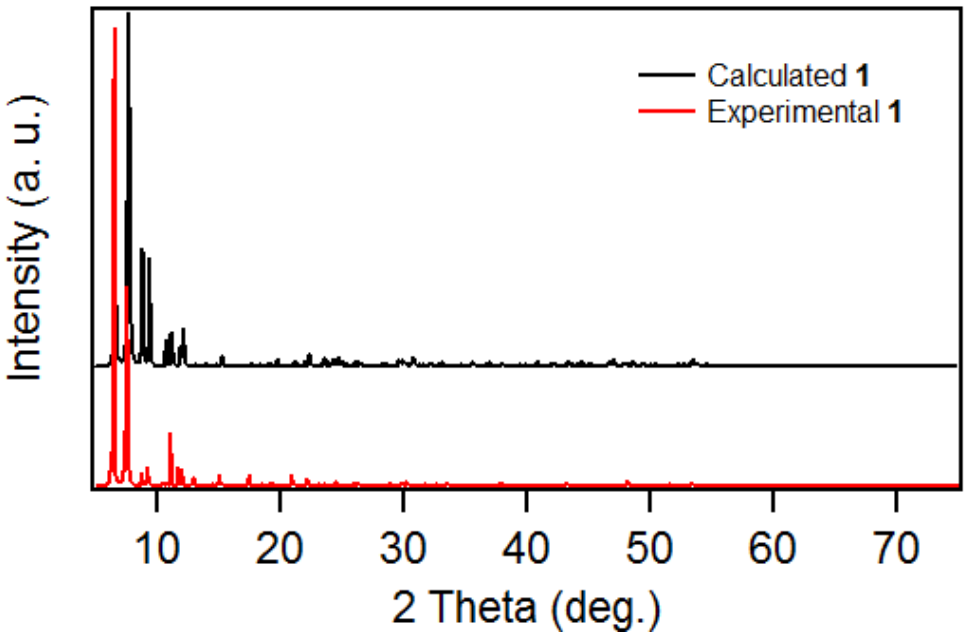

Figure 5.39: PXRD spectrum of **1** (red) and the calculated spectrum of **1** (black) from SCXRD data.

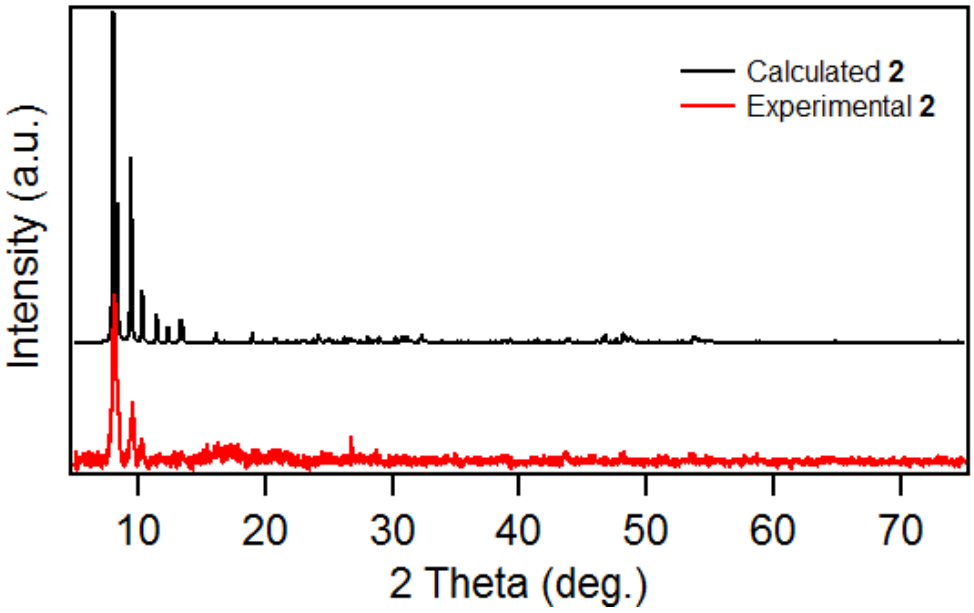

Figure 5.40: PXRD spectrum of **2** (red) and the calculated spectrum of **2** (black) from SCXRD data. The material obtained had poor crystallinity and quickly decomposed even when precautions were taken to exclude air.

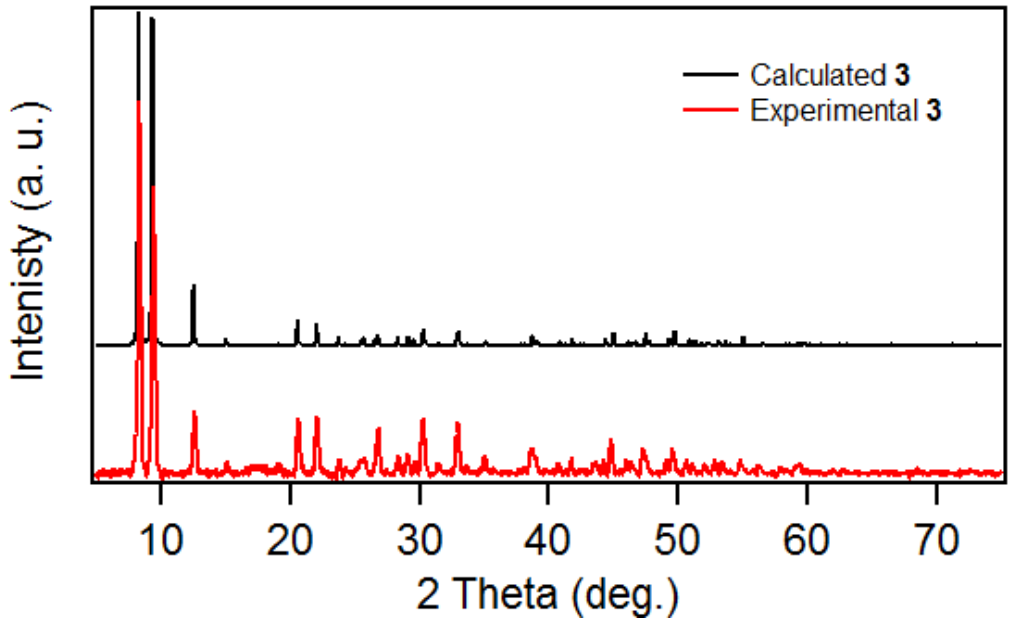

Figure 5.41: PXRD spectrum of **3** (red) and the calculated spectrum of **3** (black) from SCXRD data.

5.10 Additional NMR Spectra and Mother Liquor Analysis by NMR

^{1}H, and ^{31}P NMR spectra were recorded on a Bruker DRX400 or DRX 500 spectrometer. ^{1}H spectra were referenced using C_6D_6, tetrahydrofuran-d_8, or DMSO-d_6 with the residual solvent peaks as the internal standard, and ^{31}P spectra were referenced using H_3PO_4. Chemical shifts were reported in ppm.

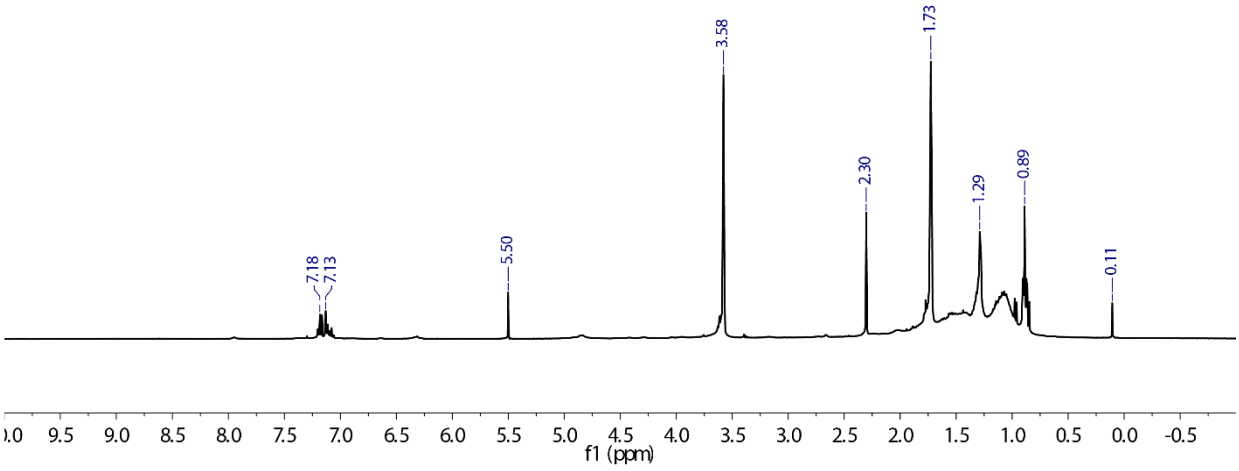

Figure 5.42: ^{1}H NMR (tetrahydrofuran-d_8, 400 MHz) spectrum **1**. No assignable peaks other than residual solvent signals could be identified. Those signals are: toluene at 7.18, 7.13, and 2.30 ppm; DCM at 5.50 ppm; THF at 3.58 and 1.73 ppm; hexanes at 1.29 and 0.89 ppm; and silicon grease at 0.11 ppm.

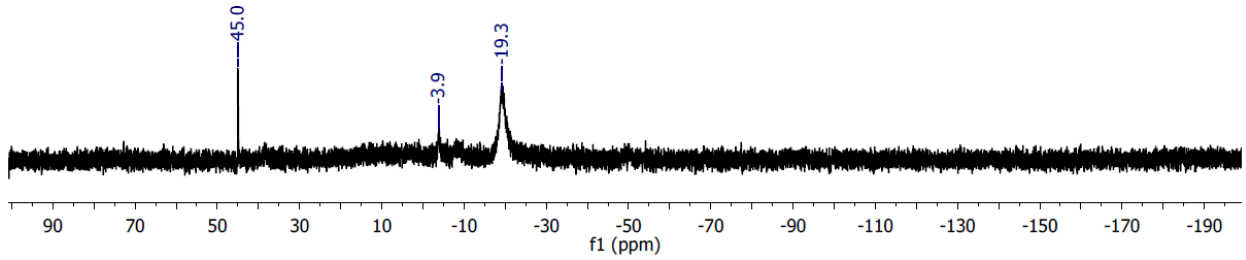

Figure 5.43: 31P{1H} NMR (tetrahydrofuran-d8, 162 MHz) spectrum of **1**.

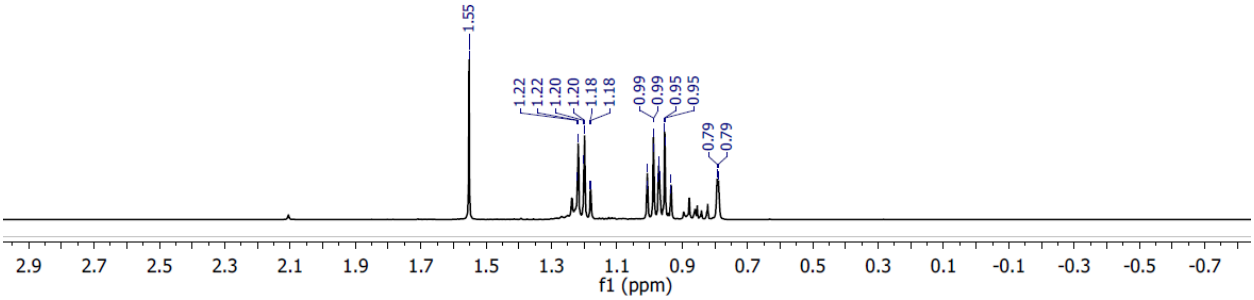

Figure 5.44: ^{1}H NMR (benzene-d_6, 400 MHz) spectrum of the products obtained in the cold end of the tube used in the thermolysis of **1**. The spectrum shows what appears to be splitting associated with PEt_3.

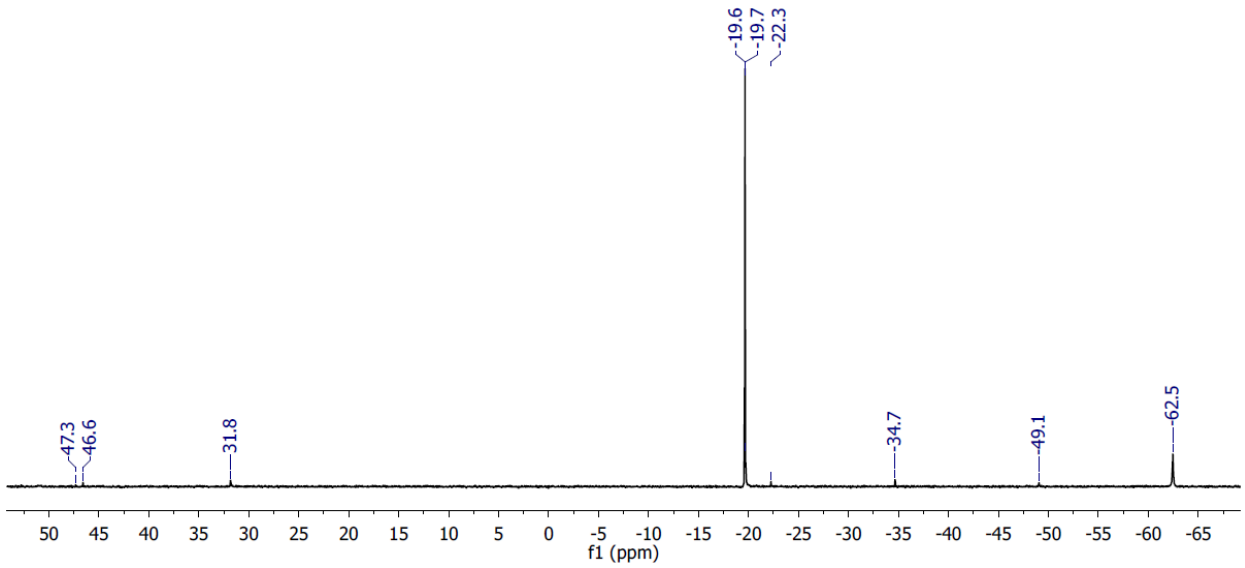

Figure 5.45: $^{31}P\{^{1}H\}$ NMR (benzene-d_6, 162 MHz) spectrum of the products obtained in the cold end of the tube used in the thermolysis of **1**. The strong signal at -19 suggests that the products are mainly PEt_3

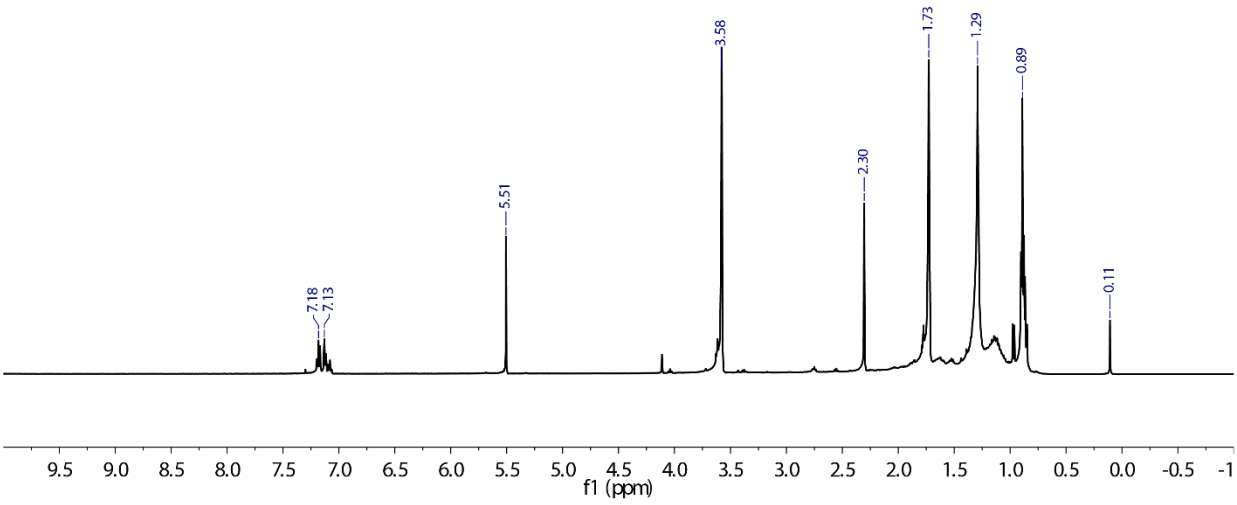

Figure 5.46: ^{1}H NMR (tetrahydrofuran-d_8, 500 MHz) spectrum of **1+**. No assignable peaks other than residual solvent signals could be identified. Those signals are: toluene at 7.18, 7.13, and 2.30 ppm; DCM at 5.50 ppm; THF at 3.58 and 1.73 ppm; hexanes at 1.29 and 0.89 ppm; and silicon grease at 0.11 ppm.

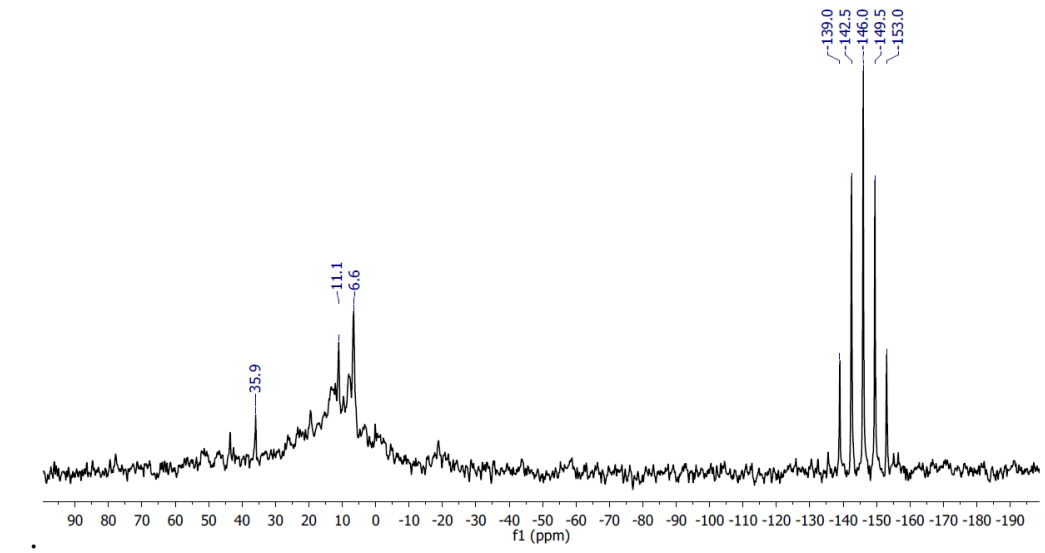

Figure 5.47: $^{31}P\{^{1}H\}$ NMR (tetrahydrofuran-d_8, 202 MHz) spectrum of **1**+.

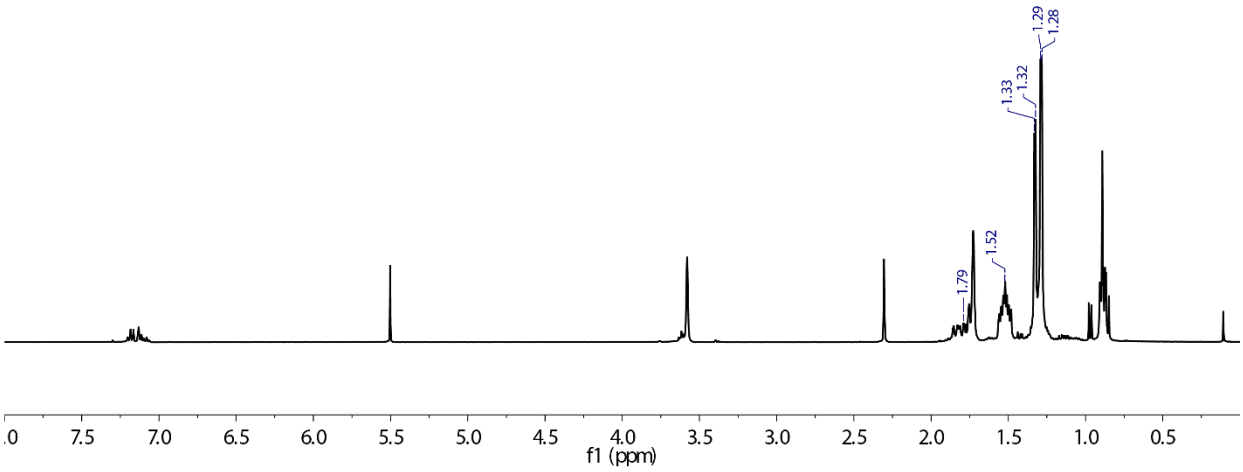

Figure 5.48: ^{1}H NMR (tetrahydrofuran-d_8, 400 MHz) spectrum of **4**.

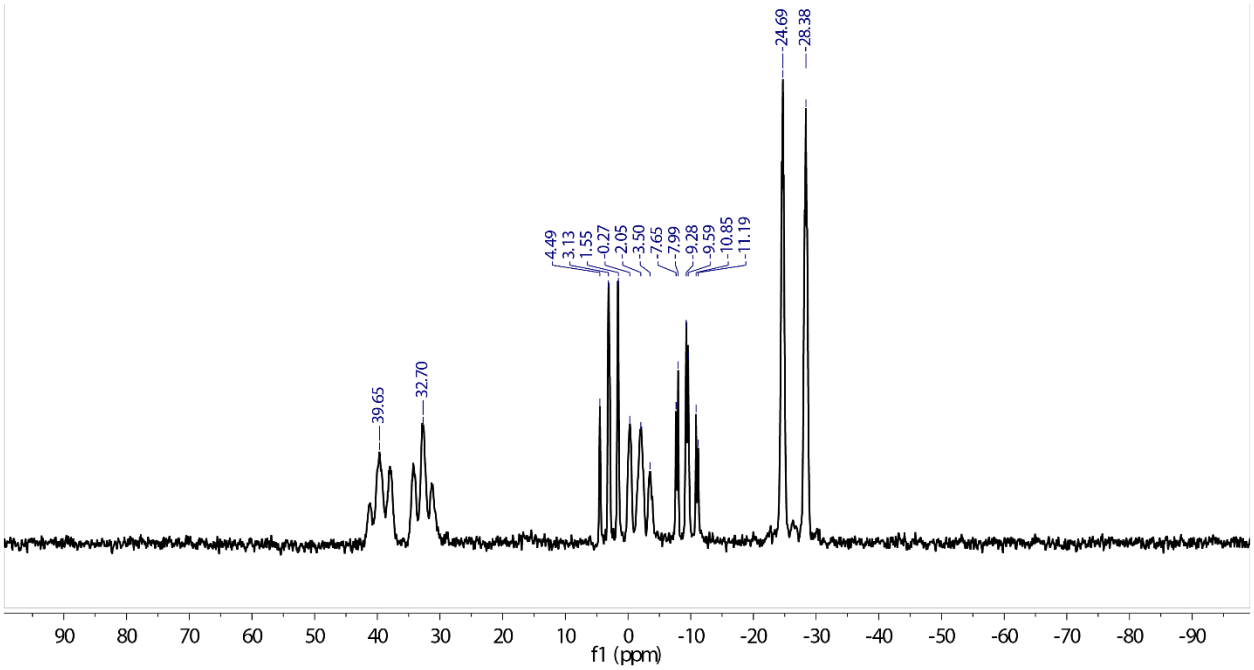

Figure 5.49: $^{31}P\{^{1}H\}$ NMR (tetrahydrofuran-d_8, 162 MHz) spectrum of **4**.

Due to the poor yields of the cluster reactions, analysis was performed on the mother liquors to determine the major products of each reaction. The mother liquors of **1** and **2** were analyzed by both ^{1}H and ^{31}P NMR. From the ^{1}H NMR spectra obtained for the mother liquors, only solvent signals are observed as well as broad signals that may be characteristic of the respective phosphine ligands but are otherwise unassignable. Analysis of the mother liquors using ^{31}P NMR does not provide useful information other than the organocyclophosphine is completely consumed/complexed, various $Ni((PR)_3)_x$ complexes are present,[39-40] free PR_3 is present, or **4** is present. From this information, no definitive conclusions can be made regarding the major products in these reactions.

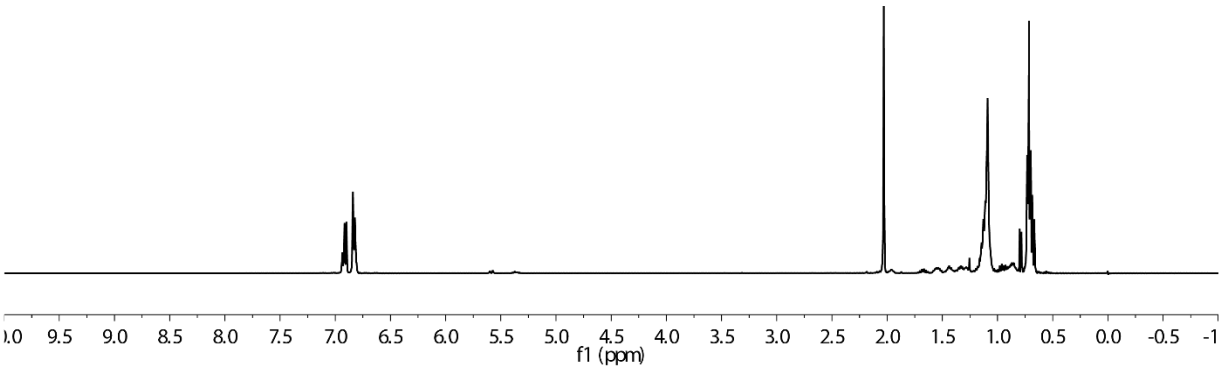

Figure 5.50: ^{1}H NMR (DMSO-d_6, 400 MHz) spectrum of the mother liquor of **1**. Only solvent signals from toluene and hexanes are identifiable.

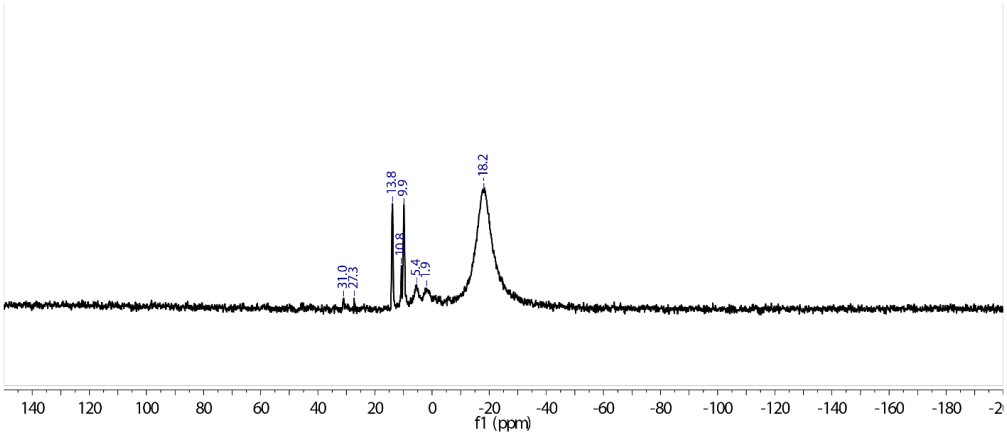

Figure 5.51: ^{31}P NMR (DMSO-d_6, 162 MHz) spectrum of the mother liquor of **1**

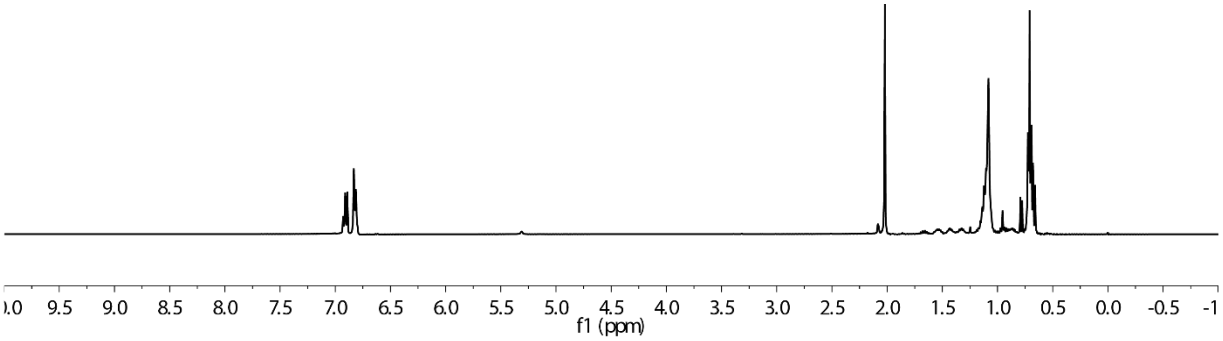

Figure 5.52: ^{1}H NMR (DMSO-d_6, 400 MHz) spectrum of the mother liquor of **2**. Only solvent signals from toluene and hexanes are identifiable.

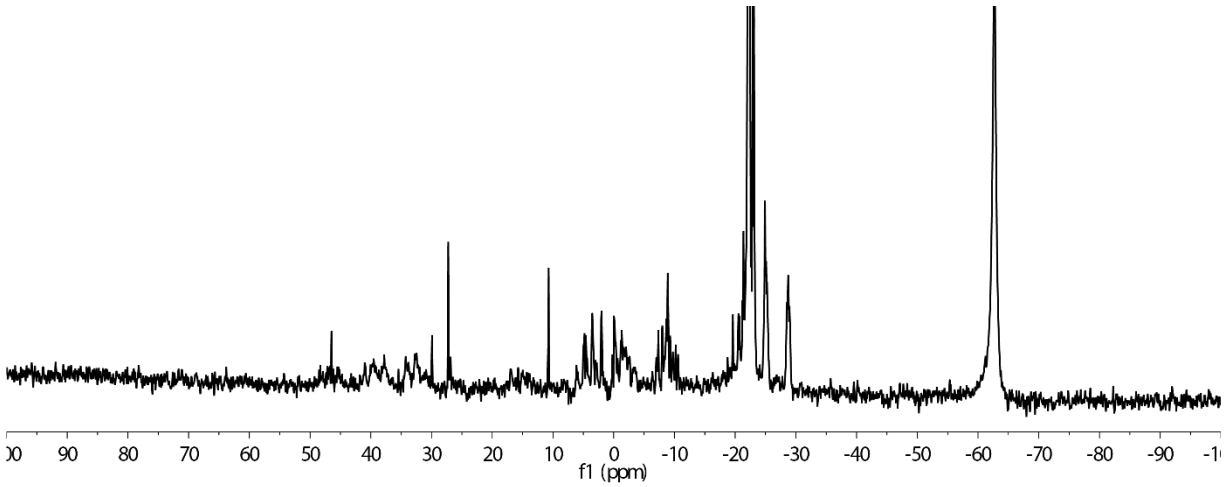

Figure 5.53: ^{31}P NMR (DMSO-d_6, 162 MHz) spectrum of the mother liquor of **2**.

5.11 Single Crystal X-ray Diffraction

Single crystal x-ray diffraction data was collected on an Agilent SuperNova diffractometer using mirror-monochromated CuK_α or MoK_α radiation. Data collection, integration, scaling (ABSPACK) and absorption correction (face-indexed Gaussian integration[41] or numeric analytical methods[42]) were performed in CrysAlisPro.[43] Structure solution was performed using ShelXT.[44] Subsequent refinement was performed by full-matrix least-squares on F^2 in ShelXL.[44] Olex2[45] was used for viewing and to prepare CIF files. Many disordered molecules were modeled as rigid fragments from the Idealized Molecular Geometry Library.[46] ORTEP graphics were prepared in CrystalMaker.[47] Thermal ellipsoids are rendered at the 50% probability level. Details of crystallographic data and parameters for data collection and refinement are provided in **Table S1**. Crystals were mounted on MiTeGen mounts with the aid of STP oil and cooled to 100 K on the diffractometer for screening and data collection. A minimum of 1 hemisphere of data to 0.8 Å

resolution was collected for all compounds. Structure solution and space group assignment were typically performed in ShelXT with no difficulty. In the final refinements, non-H atoms were refined anisotropically with no restraints unless noted; C-H hydrogens were placed in calculated positions and refined with riding isotropic ADPs and coordinates. In several structures, PEt_3 groups were disordered over two positions and these were typically modeled by standard techniques with geometry stabilized by SAME instructions and ADPs stabilized by RIGU and SIMU instructions for all disordered atoms. Other non-routine details of the refinements are given below:

Compound 2: Crystals of 2 diffracted poorly, with most reflections diffuse and anisotropically streaked. After screening many crystals, the best crystal we identified was twinned by a 180 deg. rotation around the direct axis uvw = 311, and further by a 16 deg. rotation around uvw = 0.8730 0.3984 0.2815 (an apparent hitchhiker). The refined volume fractions for these two components were 32.3(6) and 6.2(4) %. The isolated reflections of the minor twin components were omitted from the final data set. In view of the difficult integration, the final refinement gave relatively poor agreement factors (R1 ~12%) and a strongly featured difference map (max. peak 2.7 e- Å-3).

Compound 4: The crystal was apparently cracked with many high-resolutions reflections significantly split. The overlap was modeled by treating the crystal as a two-component twin by a 3.9 deg. rotation around *uvw* = 0.1477 0.9388 -0.3113. The entire structure was disordered in an 86:14 ratio by a flip of two PMe groups in the P_5R_5 ring. The major and minor components were made equivalent by a SAME instruction. The major component was refined with anisotropic ADPs and no other restraints besides a short-range SIMU instruction for overlapping ADPs. The minor component was refined with free isotropic

ADPs on Ni and P atoms and two group isotropic ADPs for carbon atoms; one for PMe methyl groups and another for PMe_3 methyl groups.

Table 5.5: Selected Crystallographic Data

Compound	1	1+	2
Formula	$C_{58}H_{150}Ni_{12}P_{18}$	$C_{58}H_{150}F_6Ni_{12}P_{19}$	$C_{30}H_{90}Ni_8P_{14}$
MW	2109.75	2254.72	1354.27
Space group	P-1	P-1	I2/m
***a* (Å)**	12.1036(3)	12.1480(3)	11.7378(14)
***b* (Å)**	12.9126(3)	12.8618(3)	17.0869(14)
***c* (Å)**	15.0385(4)	15.5073(5)	15.0675(17)
***α* (°)**	111.638(2)	73.488(3)	90
***β* (°)**	99.255(2)	72.044(3)	108.229(13)
***γ* (°)**	99.7316(18)	73.633(2)	90
V (Å^3)	2088.45(9)	2159.20(11)	2870.3(6)
Z	1	1	2
ρ_{calc} (g cm^{-3})	1.677	1.734	1.567
T (K)	100	100.0(2)	150
λ (Å)	1.54184	1.54184	1.54184
$2\theta_{min}$, $2\theta_{max}$	7.6, 146	7.3, 146	10.3, 142
Nref	23456	24089	25759
R(int), R(σ)	.038, .040	.0239,	.063, .094
μ(mm^{-1})	6.334	6.444	6.630
Size (mm)	0.051 × 0.085 × 0.134	0.027 × 0.079 × 0.301	0.046 × 0.088 × 0.14
T_{max} / T_{min}	1.39	3.34	2.95
Data	8292	8558	6982
Restraints	764	109	46
Parameters	615	592	159
R_1(obs)	0.0527	0.0297	0.1161
wR_2(all)	0.1509	0.0781	0.3344
S	1.065	1.022	1.068
Peak, hole (e$^-$ Å^{-3})	1.2, -0.7	0.7, -0.8	2.8, -1.1
CCDC deposition #	1910295	1910297	1910294

Compound	3	4
Formula	$C_{36}H_{96}Ni_8P_{12}$	$C_{22}H_{66}Ni_2P_{14}$
MW	1370.44	881.74
Space group	R-3	$P2_1/n$
***a* (Å)**	21.3071(8)	9.16443(14)
***b* (Å)**	21.3071(8)	10.72956(14)
***c* (Å)**	10.9926(4)	21.7012(3)
***α* (°)**	90	90
***β* (°)**	90	90.2720(14)
***γ* (°)**	120	90
V (Å^3)	4321.9(4	2133.86(5
Z	3	2
ρ_{calc} (g cm^{-3})	1.580	1.372
T (K)	100.0(2)	100.0(2)
λ (Å)	1.54184	1.54184
$2\theta_{min}$, $2\theta_{max}$	9.4, 144	8.1, 146
Nref	15938	45007
R(int), R(σ)	0.0894,	.032, .066
μ(mm^{-1})	6.104	6.173
Size (mm)	0.018 × 0.022 × 0.181	0.05 × 0.051 × 0.078
T_{max}, T_{min}	1.54	1.03
Data	1880	9891
Restraints	0	160
Parameters	90	263
R_1(obs)	0.0546	0.0246
wR_2(all)	0.1492	0.0510
S	1.088	0.937
Peak, hole (e$^-$ Å^{-3})	1.1, -1.1	0.3, -0.2
CCDC deposition #	1910296	1910298

Table 5.6: Comparison of average Ni – Ni bond distances (Å) and their standard deviations within the cores of **1** and **1+** showing a slight contraction and distortion of the core upon oxidation of **1**. Ni_b corresponds to the side-bridging nickel atoms of the **1** and **1+** clusters whereas Ni_e corresponds to the end-capping nickel atoms.

Bond	**1**	**1+**	**Difference**
$Ni_b - Ni_e$	2.5639(89)	2.5498(14)	0.0141
$Ni_e - Ni_e$	2.6787(79)	2.661(22)	0.0176

5.12 References

1. Fehlner, T.; Halet, J.-F.; Saillard, J.-Y., *Molecular Clusters: A Bridge to Solid-State Chemistry*. Cambridge University Press: Cambridge, 2007.

2. Tsui, E. Y.; Tran, R.; Yano, J.; Agapie, T., Redox-inactive metals modulate the reduction potential in heterometallic manganese-oxido clusters. *Nature Chemistry* **2013,** *5*, 293-299.

3. Sanchez, R. H.; Betley, T. A., Thermally Persistent High-Spin Ground States in Octahedral Iron Clusters. *Journal of the American Chemical Society* **2018,** *140*, 16792-16806.

4. Rosemann, N. W.; Eussner, J. P.; Beyer, A.; Koch, S. W.; Volz, K.; Dehnen, S.; Chatterjee, S., A highly efficient directional molecular white-light emitter driven by a continuous-wave laser diode. *Science* **2016,** *352*, 1301-1304.

5. Degroot, M. W.; Corrigan, J. F., 7.2 - High Nuclearity Clusters: Metal–Chalcogenide Polynuclear Complexes. In *Comprehensive Coordination Chemistry II*, McCleverty, J. A.; Meyer, T. J., Eds. Pergamon: Oxford, 2003; pp 57-123.

6. Champsaur, A. M.; Velian, A.; Paley, D. W.; Choi, B.; Roy, X.; Steigerwald, M. L.; Nuckolls, C., Building Diatomic and Triatomic Superatom Molecules. *Nano Letters* **2016,** *16*, 5273-5277.

7. Turkiewicz, A.; Paley, D. W.; Besara, T.; Elbaz, G.; Pinkard, A.; Siegrist, T.; Roy, X., Assembling Hierarchical Cluster Solids with Atomic Precision. *Journal of the American Chemical Society* **2014,** *136*, 15873-15876.

8. Pinkard, A.; Champsaur, A. M.; Roy, X., Molecular Clusters: Nanoscale Building Blocks for Solid-State Materials. *Accounts of Chemical Research* **2018,** *51*, 919-929.

9. Roy, X.; Lee, C. H.; Crowther, A. C.; Schenck, C. L.; Besara, T.; Lalancette, R. A.; Siegrist, T.; Stephens, P. W.; Brus, L. E.; Kim, P.; Steigerwald, M. L.; Nuckolls, C., Nanoscale Atoms in Solid-State Chemistry. *Science* **2013,** *341*, 157-160.

10. Ong, W. L.; O'Brien, E. S.; Dougherty, P. S. M.; Paley, D. W.; Higgs, C. F.; McGaughey, A. J. H.; Malen, J. A.; Roy, X., Orientational order controls crystalline and amorphous thermal transport in superatomic crystals. *Nature Materials* **2017,** *16*, 83-88.

11. Baudron, S. A.; Batail, P.; Coulon, C.; Clerac, R.; Canadell, E.; Laukhin, V.; Melzi, R.; Wzietek, P.; Jerome, D.; Auban-Senzier, P.; Ravy, S., (EDT-TTF-CONH2)(6)[Re6Se8(CN)(6)], a metallic Kagome-type organic-inorganic hybrid compound: Electronic instability, molecular motion, and charge localization. *Journal of the American Chemical Society* **2005,** *127*, 11785-11797.

12. Reber, A. C.; Khanna, S. N., Superatoms: Electronic and Geometric Effects on Reactivity. *Accounts of Chemical Research* **2017,** *50*, 255-263.

13. Bennett, M. V.; Beauvais, L. G.; Shores, M. P.; Long, J. R., Expanded Prussian blue analogues incorporating [Re(6)Se(8)(CN)(6)](3-/4-) clusters: Adjusting porosity via charge balance. *Journal of the American Chemical Society* **2001,** *123*, 8022-8032.

14. Hessen, B.; Siegrist, T.; Palstra, T.; Tanzler, S. M.; Steigerwald, M. L., Cr6te8(Pet3)6 and a Molecule-Based Synthesis of Cr3te4. *Inorganic Chemistry* **1993,** *32*, 5165-5169.

15. Oyama, S. T.; Gott, T.; Zhao, H. Y.; Lee, Y. K., Transition metal phosphide hydroprocessing catalysts: A review. *Catalysis Today* **2009,** *143*, 94-107.

16. Anantharaj, S.; Ede, S. R.; Sakthikumar, K.; Karthick, K.; Mishra, S.; Kundu, S., Recent Trends and Perspectives in Electrochemical Water Splitting with an Emphasis on Sulfide, Selenide, and Phosphide Catalysts of Fe, Co, and Ni: A Review. *Acs Catalysis* **2016,** *6*, 8069-8097.

17. Muthuswamy, E.; Kharel, P. R.; Lawes, G.; Brock, S. L., Control of Phase in Phosphide Nanoparticles Produced by Metal Nanoparticle Transformation: Fe2P and FeP. *ACS Nano* **2009,** *3*, 2383-2393.

18. Carenco, S.; Portehault, D.; Boissière, C.; Mézailles, N.; Sanchez, C., Nanoscaled Metal Borides and Phosphides: Recent Developments and Perspectives. *Chemical Reviews* **2013,** *113*, 7981-8065.

19. Mundy, M. E.; Ung, D.; Lai, N. L.; Jahrman, E. P.; Seidler, G. T.; Cossairt, B. M., Aminophosphines as Versatile Precursors for the Synthesis of Metal Phosphide Nanocrystals. *Chemistry of Materials* **2018,** *30*, 5373-5379.

20. Henkes, A. E.; Vasquez, Y.; Schaak, R. E., Converting Metals into Phosphides: A General Strategy for the Synthesis of Metal Phosphide Nanocrystals. *Journal of the American Chemical Society* **2007,** *129*, 1896-1897.

21. Fenske, D.; Holstein, W., [Cu96P30{P(SiMe3)2}6(PEt3)18], a New Phosphorus-Bridged Copper Cluster. *Angewandte Chemie International Edition in English* **1994,** *33*, 1290-1292.

22. Gary, D. C.; Flowers, S. E.; Kaminsky, W.; Petrone, A.; Li, X.; Cossairt, B. M., Single-Crystal and Electronic Structure of a 1.3 nm Indium Phosphide Nanocluster. *Journal of the American Chemical Society* **2016,** *138*, 1510-1513.

23. Huttner, G.; Knoll, K., RP-Bridged Metal Carbonyl Clusters: Synthesis, Properties, and Reactions. *Angewandte Chemie International Edition in English* **1987,** *26*, 743-760.

24. Whitmire, K. H., Main Group–Transition Metal Cluster Compounds of the Group 15 Elements. In *Advances in Organometallic Chemistry*, Stone, F. G. A.; West, R., Eds. Academic Press: 1998; Vol. 42, pp 1-145.

25. Akita, M., Iron Cluster Compounds: Compounds without Hydrocarbon Ligands. In *Comprehensive Organometallic Chemistry III*, Mingos, D. M. P.; Crabtree, R. H., Eds. Elsevier: Oxford, 2007; pp 259-292.

26. Köhler, H.; Michaelis, A., Ueber Phenylphosphin und Phosphobenzol (Diphosphenyl). *Berichte der deutschen chemischen Gesellschaft* **1877,** *10*, 807-814.

27. Kosolapoff, G. M.; Maier, L., *Organic phosphorus compounds*. Wiley-Interscience: New York,, 1972.

28. Ahlrichs, R.; Fenske, D.; Oesen, H.; Schneider, U., Synthesis and Structure of [Ni(PtBu6)] and [Ni5(PtBu)6(CO)5] and Calculations on the Electronic Structure of [Ni(PtBu)6] and (PR)6, R = tBu,Me. *Angewandte Chemie International Edition in English* **1992,** *31*, 323-326.

29. Bai, J.; Virovets, A. V.; Scheer, M., Synthesis of Inorganic Fullerene-Like Molecules. *Science* **2003,** *300*, 781.

30. Scherer, M.; Stein, D.; Breher, F.; Geier, J.; Schönberg, H.; Grützmacher, H., Copper(I) Chloride Cluster Complexes with Pentaphenyl-Cyclopentaphosphane as Ligand. *Zeitschrift für anorganische und allgemeine Chemie* **2005,** *631*, 2770-2774.

31. Baudler, M.; Glinka, K.; Cowley, A. H.; Pakulski, M., Organocyclophosphanes. *Inorganic Syntheses*.

32. Fenske, D.; Magull, J., Zur Reaktion von NiCl2 mit PhP(SiMe3)2 Die Kristallstruktur von [Ni12Cl2(PPh)2(P2Ph2)4(PHPh)8]. *Zeitschrift für anorganische und allgemeine Chemie* **1991,** *594*, 29-35.

33. Matus, M. H.; Nguyen, M. T.; Dixon, D. A., Heats of Formation of Diphosphene, Phosphinophosphinidene, Diphosphine, and Their Methyl Derivatives, and Mechanism of the Borane-Assisted Hydrogen Release. *The Journal of Physical Chemistry A* **2007,** *111*, 1726-1736.

34. Lower, L. D.; Dahl, L. F., Synthesis and Structural Characterization of a New Type of Metal Cluster System, Ni8(Co)8(Mu4-Pc6h5)6, Containing a Completely Bonding Metal Cube - Transition-Metal Analog of Cubane, C8h8. *Journal of the American Chemical Society* **1976,** *98*, 5046-5047.

35. Fenske, D.; Basoglu, R.; Hachgenei, J.; Rogel, F., Novel Clusters of Cobalt and Nickel with Organo-Phosphorus Ligands. *Angewandte Chemie-International Edition in English* **1984,** *23*, 160-162.

36. Brennan, J. G.; Siegrist, T.; Stuczynski, S. M.; Steigerwald, M. L., The Transition from Molecules to Solids - Molecular Syntheses of Ni9te6(Pet3)8, Ni20te18(Pet3)12, and Nite. *Journal of the American Chemical Society* **1989,** *111*, 9240-9241.

37. Popczun, E. J.; McKone, J. R.; Read, C. G.; Biacchi, A. J.; Wiltrout, A. M.; Lewis, N. S.; Schaak, R. E., Nanostructured Nickel Phosphide as an Electrocatalyst for the Hydrogen Evolution Reaction. *Journal of the American Chemical Society* **2013,** *135*, 9267-9270.

38. Henderson, W. A.; Epstein, M.; Seichter, F. S., Some Aspects of the Chemistry of Cyclopolyphosphines. *Journal of the American Chemical Society* **1963,** *85*, 2462-2466.

39. Porschke, K. R., Mono(Ethyne)Nickel(O) and Bis(Ethyne)Nickel(0) Complexes. *Journal of the American Chemical Society* **1989,** *111*, 5691-5699.

40. Johnson, S. A.; Mroz, N. M.; Valdizon, R.; Murray, S., Characterization of Intermediates in the C-F Activation of Tetrafluorobenzenes using a Reactive Ni(PEt3)(2) Synthon: Combined Computational and Experimental Investigation. *Organometallics* **2011,** *30*, 441-457.

41. Blanc, E.; Schwarzenbach, D.; Flack, H. D., The evaluation of transmission factors and their first derivatives with respect to crystal shape parameters. *Journal of Applied Crystallography* **1991,** *24*, 1035-1041.

42. Clark, R. C.; Reid, J. S., The analytical calculation of absorption in multifaceted crystals. *Acta Crystallographica Section A* **1995,** *51*, 887-897.

43. *CrysAlisPro*, Version 1.171.37.35; Oxford Diffraction /Agilent Technologies UK Ltd: Yarnton, England, 2014.

44. Sheldrick, G., SHELXT - Integrated space-group and crystal-structure determination. *Acta Crystallographica Section A* **2015,** *71*, 3-8.

45. Dolomanov, O. V.; Bourhis, L. J.; Gildea, R. J.; Howard, J. A. K.; Puschmann, H., OLEX2: a complete structure solution, refinement and analysis program. *Journal of Applied Crystallography* **2009,** *42*, 339-341.

46. Guzei, I., An idealized molecular geometry library for refinement of poorly behaved molecular fragments with constraints. *Journal of Applied Crystallography* **2014,** *47*, 806-809.

47. *CrystalMaker*, CrystalMaker Software Ltd: Oxford, England.